

**MICROPHOTONIC DEVICES FOR COMPACT PLANAR  
LIGHTWAVE CIRCUITS AND SENSOR SYSTEMS**

**by**

**JAIME CARDENAS GONZALEZ**

**A DISSERTATION**

**Submitted in partial fulfillment of the requirements  
for the degree of Doctor of Philosophy  
in  
The Optical Science and Engineering Program  
to  
The School of Graduate Studies  
of  
The University of Alabama in Huntsville**

**HUNTSVILLE, ALABAMA**

**2005**

In presenting this dissertation in partial fulfillment of the requirements for a doctoral degree from The University of Alabama in Huntsville, I agree that the Library of this University shall make it freely available for inspection. I further agree that permission for extensive copying for scholarly purposes may be granted by my advisor or, in his/her absence, by the Director of the Program or the Dean of the School of Graduate Studies. It is also understood that due recognition shall be given to me and to The University of Alabama in Huntsville in any scholarly use which may be made of any material in this dissertation.

\_\_\_\_\_  
(student signature)

\_\_\_\_\_  
(date)

**DISSERTATION APPROVAL FORM**

Submitted by Jaime Cardenas Gonzalez in partial fulfillment of the requirements for the degree of Doctor of Philosophy in Optical Science and Engineering and accepted on behalf of the Faculty of the School of Graduate Studies by the dissertation committee.

We, the undersigned members of the Graduate Faculty of The University of Alabama in Huntsville, certify that we have advised and/or supervised the candidate on the work described in this dissertation. We further certify that we have reviewed the dissertation manuscript and approve it in partial fulfillment of the requirements of the degree of Doctor of Philosophy in Optical Science & Engineering.

Committee Chair

---

---

---

---

---

---

---

---

Program Director

---

College Dean

---

Graduate Dean

---

**ABSTRACT**  
School of Graduate Studies  
The University of Alabama in Huntsville

Degree    Doctor of Philosophy      Program      Optical Science and Engineering

Name of Candidate    Jaime Cardenas Gonzalez

Title    Microphotonic Devices for Compact Planar Lightwave Circuits and Sensor Systems

Higher levels of integration in planar lightwave circuits and sensor systems can reduce fabrication costs and broaden viable applications for optical network and sensor systems. For example, increased integration and functionality can lead to sensor systems that are compact enough for easy transport, rugged enough for field applications, and sensitive enough even for laboratory applications. On the other hand, more functional and compact planar lightwave circuits can make optical networks components less expensive for the metro and access markets in urban areas and allow penetration of fiber to the home. Thus, there is an important area of opportunity for increased integration to provide low cost, compact solutions in both network components and sensor systems.

In this dissertation, a novel splitting structure for microcantilever deflection detection is introduced. The splitting structure is designed so that its splitting ratio is dependent on the vertical position of the microcantilever. With this structure, microcantilevers sensitized to detect different analytes or biological agents can be integrated into an array on a single chip. Additionally, the integration of a depolarizer into the optoelectronic integrated circuit in an interferometric fiber optic gyroscope is presented as a means for cost reduction. The savings come in avoiding labor

intensive fiber pigtailed steps by permitting batch fabrication of these components. In particular, this dissertation focuses on the design of the waveguides and polarization rotator, and the impact of imperfect components on the performance of the depolarizer. In the area of planar lightwave circuits, this dissertation presents the development of a fabrication process for single air interface bends (SAIBs). SAIBs can increase integration by reducing the area necessary to make a waveguide bend. Fabrication and measurement of a 45° SAIB with a bend efficiency of 93.4% for TM polarization and 92.7% for TE polarization are presented.

Abstract Approval: Committee Chair \_\_\_\_\_  
*(Date)*

Program Director \_\_\_\_\_

Graduate Dean \_\_\_\_\_

## **ACKNOWLEDGMENTS**

I want to thank my advisor, Dr. Gregory Nordin, for his guidance, teachings, and support throughout my PhD. His guidance was a cornerstone throughout my research. I would also like to thank the members of my committee for their assistance. Additionally, I am grateful to the students and staff at the Nano and Micro Devices Center.

I would like to thank my parents for giving me the best education possible and the necessary tools to reach this point in my career.

Finally, I would like to give a very special thanks to my wife, Cecilia. Without her love and support, none of this would have been possible.

# TABLE OF CONTENTS

	Page
LIST OF FIGURES .....	xi
LIST OF TABLES.....	xix
LIST OF SYMBOLS .....	xx
LIST OF ACRONYMS .....	xxiv
Chapter 1 INTRODUCTION.....	1
1.1 Motivation.....	1
1.2 Dissertation Overview .....	3
1.3 New Contributions .....	5
Chapter 2 BACKGROUND.....	6
2.1 Microcantilevers for Sensing Applications.....	6
2.1.1 Basics of Microcantilevers as Sensors.....	6
2.1.2 Detection Mechanisms.....	9
2.1.3 Novel Photonic Microcantilevers .....	10
2.2 Interferometric Fiber Optic Gyroscope.....	11
2.2.1 Fundamentals of Optical Rotational Sensing.....	11
2.2.2 Typical IFOG Configuration.....	12
2.3 Polymer Plasma Etching.....	13
2.4 Waveguide Bends .....	17
Chapter 3 WAVEGUIDE MICROCANTILEVER DEFLECTION SENSOR DESIGN..	21
3.1 Introduction.....	21
3.2 Design and Analysis .....	22

3.2.1	Component Design.....	23
3.2.2	Sensitivity Analysis .....	25
3.3	Conclusion .....	30
Chapter 4	INTEGRATED OPTIC DEPOLARIZER: DESIGN AND ANALYSIS .....	32
4.1	Introduction.....	32
4.2	System Concept .....	33
4.2.1	Beam Delay.....	35
4.2.2	Measurement of the Source’s Autocorrelation Function .....	36
4.2.3	DoP Tolerance Analysis .....	42
4.3	Design of Required Components .....	49
4.3.1	Waveguide Design .....	49
4.3.2	Polarization Transformer .....	51
4.4	Conclusion .....	53
Chapter 5	INTEGRATED OPTIC DEPOLARIZER: ETCH DEVELOPMENT.....	54
5.1	Introduction.....	54
5.2	Etch Development.....	55
5.2.1	Oxygen, Helium, and Tetrafluoromethane .....	55
5.2.2	Oxygen and Sulfur Hexafluoride .....	59
5.3	Conclusion .....	67
Chapter 6	MICROMOLDED WAVEGUIDES .....	69
6.1	Introduction.....	69
6.2	Mold Requirements.....	71
6.2.1	Chemical Compatibility .....	72

6.2.2	Thermal Stability .....	75
6.2.3	Mold Removal .....	76
6.3	Fabrication Approaches .....	78
6.3.1	SU8 as the Mold Material .....	78
6.3.2	High Temperature Resist as the Mold Material .....	82
6.3.3	Silicon Dioxide as a Mold Material .....	84
6.4	Conclusion .....	89
Chapter 7 FABRICATION OF DEEP TRENCHES IN PFCB POLYMERS .....		90
7.1	Introduction.....	90
7.2	Etch Development.....	92
7.3	Etch Roughness Reduction .....	101
7.3.1	Improved Silicon Dioxide Etch .....	102
7.3.2	PFCB Etching with Reduced Sidewall Roughness.....	109
7.4	Conclusion .....	115
Chapter 8 FABRICATION AND MEASUREMENT OF 45° SINGLE AIR INTERFACE BENDS IN PFCB POLYMERS .....		116
8.1	Introduction.....	116
8.2	Single Air Interface Bend Analysis .....	118
8.3	Fabrication .....	121
8.4	Experimental Measurement and Discussion.....	127
8.5	Conclusion .....	131
Chapter 9 CONCLUSION AND FUTURE WORK.....		132
9.1	Summary.....	132

9.2	Future Research .....	134
9.2.1	Photonic Microcantilevers .....	134
9.2.2	Integrated Optic Depolarizer.....	135
9.2.3	PFCB Etch Development.....	135
9.2.4	SAIB Fabrication .....	136
APPENDIX MASK DESIGN FOR SECOND GENERATION SINGLE AIR BENDS		
	FABRICATION AND TESTING .....	137
A.1	Motivation.....	137
A.2	Mask Description.....	138
	REFERENCES .....	154

## LIST OF FIGURES

Figure	Page
2.1. (a) Optical beam detection method and (b) Piezoresistive detection method.....	10
2.2. Typical IFOG configuration using a SM fiber coil and depolarizers. ....	13
2.3. Etching profiles for different charging effects (a) bowing, (b) notching, and (c) dovetailing.....	15
2.4. Schematic of arc bends: (a) simple arc bend and (b) arc bend with tapers and trenches around the core. ....	18
2.5. Corner bend structures (a) resonance cavity, (b) double corner mirror, (c) single air interface bend, (d) multiple air trench bend, and (e) photonic crystal mirror.	19
19	
3.1. Schematic of waveguide microcantilever sensor for chemical and biological agents [41], [42].....	22
3.2. (a) Cross-section of waveguide leading to cantilever and (b) cantilever cross- section with gold coating for detection chemical and biological agents. ....	23
3.3. (a) Schematic top view of the y-branch splitter and (b) waveguide cross-section at the strip loading level.....	24
3.4. Normalized output power versus the height of the incident mode on the y- branch splitter common path. The origin of the x axis represents the incident mode profile from the cantilever in perfect alignment with the y-branch common waveguide. ....	25
3.5. Contrast after splitter output versus cantilever height. ....	29

3.6. Fundamental sensitivity limit for cantilever deflection detection as a function of optical power incident on the splitter structure.....	29
4.1. Typical IFOG configuration in which an IOC performs the polarizing, splitting and phase modulating functions. Since the coil is made of single mode fiber depolarizers are used.....	33
4.2. Poincare Sphere representation of the Integrated Optic Depolarizer concept [2]. ....	34
4.3. Integrated Optic Depolarizer Layout. ....	35
4.4. a) SLD's optical spectrum as measured by an ANDO 6315E spectrum analyzer and b) Coherence function calculated from the optical spectrum data. Note that the first minimum occurs at a time of 1.44ps.....	41
4.5. Degree of Polarization versus fraction of incident power with a TM polarization state on the depolarizing ring. As we can see, the addition of the third PBS reduces the DoP, though it will cause additional losses.....	47
4.6. Three PBS depolarizing ring configuration. The middle PBS allows TE polarized light to be transmitted and significantly attenuates the unwanted TM polarization component that leaked through the first PBS by reflecting it away from the depolarizing ring. ....	48
4.7. Waveguide Cross-section.....	50
4.8. Periodic Asymmetric Strip Loading for the Polarization Rotator. The length, thickness, refractive index, and the number of periods have to be carefully designed to obtain the desired polarization transformation. ....	52

5.1. (Top left) NOA 71 etched with 22 sccm of oxygen, 500W of coil power, 150W of platen power, and a chamber pressure of 5mT. Notice the “grass on the bottom of the etched polymer. (Top right) NOA 71 etched with 8 sccm of oxygen, 12 sccm of helium, and 2 sccm of tetrafluoromethane, 500W of coil power, 300W of platen power, and a chamber pressure of 2mT. The grass didn’t appear with this recipe. (Bottom center) NOA 71 etched with 8 sccm of oxygen, 12 sccm of helium, and 2 sccm of tetrafluoromethane, 200W of coil power, 300W of platen power, and a chamber pressure of 2mT. The grass reappeared when reducing the coil power. The coil power affects the appearance of grass significantly. ....	57
5.2. Six minute etch in ICP-RIE of 2 $\mu$ m features on full polymer stack.....	58
5.3. Two minute etch in ICP-RIE on 0.5 $\mu$ m features. Notice the severe undercutting while the etch has barely gone into the polyimide layer.....	59
5.4. Explanation for the image layout used in Figures 5.5 and 5.6. The layout is divided into four quadrants and four images are in each quadrant. The recipe parameters are depicted in this figure. ....	62
5.5. Tilted images for the 16 samples that were etched in this experiment. ....	64
5.6. Cross-section images for the 16 samples that were etched in this experiment. ....	65
5.7. Half micron features etched in a stack of NOA 71, PI-2525, and NOA 71. The etch went through the first NOA 71 layer and half way through the PI-2525 layer. It can be seen that the PI-2525 is severely undercut at the interface with the NOA 71. ....	66

5.8. Half micron features etched in PI-2525 with the same etch recipe used to etch the sample shown in figure 1. Some effects of mask erosion can be observed in the roundedness of the top of the features. However, no undercutting is evident.....	66
5.9. Half micron features etched in NOA 71 and PI-2525 with 30sccm of sulfur hexafluoride. The undercutting has been reduced with respect to the etch in Figure 5.7. ....	67
6.1. Cross-section for a typical channel waveguide with an uppercladding and an undercladding. For the waveguides discussed here, the undercladding and the uppercladding are made of the same material.....	70
6.2. Photodefined Mold: (a)-(e) illustrate the basic steps for making micromolded waveguides: (a) cladding is spun and cured on silicon substrate. (b) Mold is made on cladding. (c) Core fills mold and excess is removed with CMP so that the core material is left only inside the grooves defining the waveguides. (d) Mold is removed. (e) Cladding is spun and cured over core.....	74
6.3. (a)-(f). SU8 micromold process. ....	80
6.3. (g)-(j). SU8 micromold process. ....	81
6.4. SEM image of the core polymer and the SU8 mold on the cladding after CMP. It was impossible to remove the mold with this approach.....	81
6.5. (a)-(e). High temperature photoresist micromold process. ....	83
6.5. (f), (g). High temperature photoresist micromold process.....	84

6.6. SEM image of core polymer in the high temperature resist mold on the cladding. In the following step, when removing the mold, the core became delaminated from the cladding.....	84
6.7. (a)-(f). Silicon dioxide micromold process.....	87
6.7. (g)-(i). Silicon dioxide micromold process.....	88
6.8. SEM image of the silicon dioxide mold successfully made on a silicon substrate.	

88

7.1. A SAIB consists of an etched region placed at the intersection of a sharp waveguide bend. ....	93
7.2. SEM image of 2 $\mu$ m features etched in PFCB polymers in an RIE at 175W and 12:8 sccm of oxygen to helium. The etch took 36 minutes. Note the plastic deformation due to the cleaving of the sample during preparation for SEM imaging. ....	93
7.3. Cross-section image of etched silicon dioxide etch mask. Notice the slightly sloped sidewall and the “grassy” bottom on the PFCB surface from overetching.....	94
7.4. Half micron features etched into PFCB with an oxygen/helium chemistry. ....	95
7.5. SEM image of cross-section for typical oxygen/helium etch of 50 $\mu$ m features. At the depth of the waveguide core, the sidewall was measured to be 90.7°, which is only 0.7° from ideal verticality.....	96
7.6. Sidewall angle dependence on platen temperature during the etch process. (a) Platen temperature at 5°C. (b) Platen temperature at 35°C. ....	97
7.7. Typical sidewall roughness observed in oxygen/helium etch of PFCB. ....	98

7.8. Carbon dioxide only etch of 50 $\mu$ m features in PFCB. a) Sidewall roughness appears to be reduced, but the etch depth is shallower. b) The bowing may be due to plastic deformation from cleaving. ....	99
7.9. (a) PFCB trench sidewall when SU8 is used as an etch mask. The horizontal line in the middle of the image is due to charging during the SEM scanning. (b) Angled view of etched trench showing some SU8 remaining from the etch. The thin vertical feature that sticks out along the sidewall of the trench may be due to sidewall passivation from the byproducts of the PFCB when it is etching.....	100
7.10. Optical microscope image through DIC filter of a rectangular SAIB. The sharp corners caused stress cracks. In this case, one of the cracks goes through an adjacent waveguide. ....	100
7.11. Fabricated SAIBs with rounded edges in PFCB polymers. These structures yielded a measured optical bend efficiency of 93.4%. However, some sidewall roughness is visible. Eliminating this roughness should improve the bend efficiency.....	101
7.12. Plot showing the effect of the main parameters affecting the sidewall angle.....	106
7.13. Effect of the significant parameters affecting the silicon dioxide sidewall angle. Note that the front bottom right corner and the back top left corner deviate from the ideal vertical sidewall by less than one degree.....	107
7.14. Comparison of SiO <sub>2</sub> etch mask profile after (a) RIE etch process, and (b) optimized SiO <sub>2</sub> etch in ICP RIE.....	108

7.15. Effect of significant parameters affecting sidewall roughness. For the mask type axis, A- stands for “wet etched”, while A+ stands for “dry etched” .....	113
7.16. Comparison of (a) typical oxygen/helium etch sidewall vs. (b) carbon monoxide/oxygen etch for “Run 7”. Note that (b) looks rougher than (a) in a good portion of the sidewall. However, this etch gets smoother as the sidewall is exposed longer to the process. This data suggests that further investigation is warranted for this etch chemistry.....	114
8.1. Top view of SAIB structure for a 45° waveguide bend showing the air interface placement and choice of reference point for design. ....	119
8.2. Magnitude squared time averaged (a) magnetic field plot (TE polarization) and (b) electric field plot (TM polarization) at $\lambda=1.55\mu\text{m}$ . ....	120
8.3. Bend efficiency as a function of the position of the air interface relative to the O position. The designed position of the SAIB is $z_p = -0.2\mu\text{m}$ . Note that the vertical axis starts at a bend efficiency of 0.5.....	121
8.4. Cross-section SEM image showing the typical etch undercut ( $1.1\mu\text{m}$ as depicted by the cursor width) for an air trench. ....	123
8.5. Microscope image taken with a DIC filter through a 50x objective focused at the waveguide plane of SAIBs in good alignment.....	124
8.6. SEM image of finished air trench bend. The rounded edges are introduced to reduce stress. The dotted line depicts the waveguide core location. ....	125
8.7. SEM image of a typical sidewall for the deep anisotropic air trench etch. ....	126
8.8. SEM image of a typical air trench sidewall. ....	126

8.9. (a) Output power as a function of moving the output fiber away from the waveguide. (b) Standard deviation for measured output power in ten different measurements.....	128
8.10. Measurement data for a waveguide group that shows a bend efficiency of 93.4% with error bars indicating the variability introduced by measurement uncertainty. This waveguide group has an undercut compensation of 1.1 $\mu$ m.....	129
8.11. Simulation and measurement data as a function of SAIB interface misplacement. The horizontal axis is the actual offset introduced into the SAIB mask to compensate for misalignment.....	130
A.1. The mask is divided into die which are 1.5cm by 1.5cm. The alignment marks are placed in die 3 and 6 5.6cm apart from each other. ....	139
A.2. A single die has the waveguide patterns inside with Verniers and the die number on the upper left and lower right corners, and a 50 $\mu$ m wide dicing grid, surrounding it. ....	139
A.3. Structure's layout for die 1 through 12. The figure is to scale.....	150
A.4. Fabrication process for SAIB. Note that step g was omitted in the figure. ....	153

## LIST OF TABLES

Table	Page
3.1. Loss Budget for waveguide microcantilever sensor. ....	27
4.1. Refractive indices for IOD materials system. ....	51
5.1. Process parameters for samples etched in first run with sulfur hexafluoride. ....	61
7.1. Details of exploratory experiment for silicon dioxide etch process. ....	103
7.2. Details of silicon dioxide etch process development experiment. ....	107
7.3. Details of the polymer etching experiment. ....	112
A.1. Parameter variation for structures in die 1. ....	140
A.2. Parameter variation for structures in die 2. ....	141
A.3. Parameter variation for structures in die 3. ....	142
A.4. Parameter variation for structures in die 4. ....	143
A.5. Parameter variation for structures in die 5. ....	143
A.6. Parameter variation for structures in die 6. ....	144
A.7. Parameter variation for structures in die 7. ....	145
A.8. Parameter variation for structures in die 8. ....	146
A.9. Parameter variation for structures in die 9. ....	146
A.10. Parameter variation for structures in die 10. ....	147
A.11. Parameter variation for structures in die 11. ....	148
A.12. Parameter variation for structures in die 12. ....	149

## LIST OF SYMBOLS

<u>Symbol</u>	<u>Definition</u>
$a$	Geometric parameter relating effective microcantilever mass to the beam's mass.
$A$	Ring resonator area.
$B$	Bandwidth.
$c$	Speed of light.
$C$	Coherency matrix.
$C_{xx}$	XX element of the coherency matrix.
$C_{yy}$	YY element of the coherency matrix.
$D_c$	Coil diameter.
$DoP$	Degree of polarization.
$e$	Electron charge.
$e^j$	Complex exponential.
$\hat{e}$	Jones vector.
$E_x$	X component of the electric field.
$E_y$	Y component of the electric field.
$E(t)$	Time varying component of the Electric field.
$\vec{E}(t)$	Electric field vector.
$\vec{E}_r(t)$	Reflected electric field vector.
$\vec{E}_{rr}(t)$	Electric field vector after undergoing two reflections.

$\vec{E}_t(t)$	Transmitted electric field vector.
$\vec{E}_u(t)$	Electric field vector after undergoing two transmissions.
$\vec{E}_r(t)$	Electric field vector after recombining.
$E_Y$	Young's modulus.
$f_d$	Resonance frequency of microcantilever after the spring constant $k$ undergoes a change $\delta k$ .
$f_r$	Resonance frequency of microcantilever.
$F\{ \}$	Fourier transform.
$F^{-1}\{ \}$	Inverse Fourier transform.
$h$	Planck's constant.
$I_1, I_2$	The currents measured at detectors 1 or 2.
$I_f$	Intensity of each of the interfering beams.
$I_M$	2, 2 component of Jones matrix.
$I_t$	Transmitted fraction of TE polarized light.
$I_x$	Intensity at detector x.
$k$	Cantilever's spring constant.
$K$	Contrast.
$L_f$	Fiber length.
$L_l$	Cantilever length.
$m$	Slope of straight line.
$m^*$	Cantilever effective mass.
$m_b$	Beam's mass.
$n_{eff}$	Effective refractive index of the propagating mode.

$P_1, P_2$	The power that reaches detector 1 or 2.
$P_x$	Power at detector x.
$R(\tau)$	Autocorrelation function.
$S$	Stokes vector.
$S(f)$	Fourier transform of the Autocorrelation function.
$t_l$	Cantilever thickness.
$W_l$	Cantilever width.
$\hat{x}$	Unit vector in the $x$ direction.
$y$	Variable referring to position.
$\hat{y}$	Unit vector in the $y$ direction.
$\delta$	Phase delay.
$\delta k$	Change in cantilever's spring constant.
$\delta m^*$	Change in cantilever's effective mass.
$\delta s_1$	Change in surface stress on top cantilever surface.
$\delta s_2$	Change in surface stress on bottom cantilever surface.
$\Delta$	Fraction of TM polarized light.
$\Delta d$	Path length difference.
$\Delta I_1$	Change in current measured at detector 1.
$\Delta I_2$	Change in current measured at detector 2.
$\Delta K$	Change in contrast.
$\Delta\phi$	Phase change.
$\Delta\phi_{IFOG}$	Phase change in an IFOG.

$\Delta y$	Change in variable $y$ .
$\varepsilon_A$	Reflection fraction of TE polarized light.
$\varepsilon_B$	Transmitted fraction of TM polarized light.
$\varepsilon_M$	1,1 component of Jones matrix.
$\kappa$	Fraction of TE polarized light.
$\eta_x$	Quantum efficiency of detector x.
$\lambda_o$	Wavelength of light in a vacuum.
$\pi$	Physical constant pi.
$\sigma$	Standard deviation due to shot noise.
$\tau$	Time delay.
$\nu$	Poisson's ratio.
$\Omega$	Rotation rate.
$\langle \rangle$	Indicates time averaged.

## LIST OF ACRONYMS

<u>Acronym</u>	<u>Definition</u>
<i>2-D-FDTD</i>	Two dimensional finite difference time domain
<i>BHF</i>	Buffered Hydrofluoric acid
<i>CMP</i>	Chemical mechanical planarization
<i>CTE</i>	Coefficient of thermal expansion
<i>DOE</i>	Design of experiments
<i>ICP-RIE</i>	Inductively coupled plasma reactive ion etcher
<i>IFOG</i>	Interferometric fiber optic gyroscope
<i>MOI</i>	Mode overlap integral
<i>NMP</i>	n-Methyl Pyrrolidone
<i>OEIC</i>	Optoelectronic integrated circuit
<i>PFCB</i>	Perfluorocyclobutyl
<i>PLC</i>	Planar lightwave circuit
<i>PM</i>	Polarization maintaining
<i>PSD</i>	Position sensitive detector
<i>RIE</i>	Reactive ion etcher
<i>SAIB</i>	Single air interface bend
<i>SEM</i>	Scanning electron microscope
<i>SLD</i>	Superluminescent diode
<i>SM</i>	Single mode

<i>SOI</i>	Silicon on insulator
<i>TE</i>	Transverse electric
<i>TIR</i>	Total internal reflection
<i>TM</i>	Transverse magnetic

# CHAPTER 1

## INTRODUCTION

### 1.1 Motivation

Increasing the packing density and functionality of integrated optic circuits will generate important advantages for both sensors and optical networks. Two of the main advantages are cost reduction and compactness. Lower cost and greater portability facilitate the deployment of sensors and optical network components in broader practical applications.

Cost reduction in sensors and optical network components will increase their market penetration. For instance, there is an area of opportunity in chemical and biological sensors using waveguide microcantilevers. Arraying numerous microcantilever sensors sensitized for different chemical or biological agents and making them on a low cost platform could produce portable and disposable sensors for field application. Another important application of reduced costs through higher integration is for low cost interferometric fiber optic gyroscopes (IFOG) for small to medium aircraft. Adding functions to the current integrated optical components in an IFOG could lower the IFOGs cost enough to make it viable for this application. Moreover, there is a need for low cost

components for the metro and access networks as optical fiber technology reaches more homes in urban areas; a need which could be filled with components made in polymer materials. And, integrating more functions into a single component reduces the number of fiber connections, which add considerably to cost because they are labor intensive. Thus, cost reduction is a strong motivator for research and development to increase integration in sensors and optical network components.

Another important reason for increasing integration is compactness. In the sensing field, many times it is impossible to detect certain phenomena in a lab environment, because conditions found in a natural environment may be impossible to reproduce. Additionally, in many situations the need for measurement or detection capability lies in the field, such as in the detection of biological agents harmful to humans. Portability of sensing equipment increases its application in the real world [1]. Using the same examples as in the previous paragraph, a more compact IFOG would take less space in an aircraft. This is significant for smaller planes especially if we consider that gyroscopes are typically needed for three rotational axes. On the other hand, more portable chemical and biological sensors can be very useful in military applications where soldiers may need to recognize if an area's environment poses a threat using a small device that can sense life threatening biological agents. In optical networks, shrinking the size of components could reduce their cost by increasing the number of devices fabricated in a die. Higher integration in integrated optic devices can permit deployment of less bulky, easier to use sensors and optical network systems.

## 1.2 Dissertation Overview

Over the nine chapters in my dissertation, I will present the research I worked on as partial fulfillment of the PhD degree in Optical Science and Engineering.

In the second chapter, I will layout the background that specifically motivates the research I conducted in waveguide microcantilever deflection detection, integrated optic depolarizer design and fabrication, and fabrication and measurement of single air interface bends.

Chapter Three discusses the design and theoretical sensitivity of a novel detection method to measure the deflection of a microcantilever. This method can be implemented to detect chemical or biological agents using single cantilever detectors or with arrays of levers individually sensitized for different chemicals. The work in this chapter resulted in patent application number 10/793,783 submitted by Dr. Greg Nordin and myself.

In Chapter Four I present the integration of a depolarizer component into a planar lightwave circuit for an interferometric fiber optic gyroscope. In it I introduce the system's concept, derive the equations for imperfect components in the system and their impact in the degree of polarization, and design the waveguide and polarization transformer for the system. The other components and original concept for the integrated depolarized are the work of Dr. Lixia Li [2].

Chapter Five covers the fabrication efforts for the integrated depolarizer. It is focused on the development of a small feature highly anisotropic, vertical etch in a polymer material system. Two main etch chemistries are explored and the results are presented.

In Chapter Six I discuss my efforts to make micromolded waveguides. The requirements that the mold must meet are discussed first. Then I present the fabrication methods attempted to fabricate waveguides in perfluorocyclobutyl (PFCB) polymers using micromolding.

Chapter Seven presents the development of an etch recipe for making trenches in PFCB polymers. The etch must meet certain requirements of depth, sidewall angle, and sidewall roughness. The development of a recipe that met two of the requirements, depth and sidewall angle, is initially presented followed by our efforts to reduce the sidewall roughness. In this chapter I introduce the application of an experimentation technique commonly used in industry that is called design of experiments and apply it to develop an etch with a smoother sidewall. The work in this chapter was presented at the Photonics West 2005 conference and there are plans to publish a modified version of the manuscript in *Optical Engineering*.

In Chapter Eight, I show the design and fabrication of single air interface bends in PFCB polymers. The design was done by Dr. Seunghyun Kim, while I did the fabrication and measurement of the bends. The design is presented followed by fabrication details and, finally, by measurement results for fabricated samples. The work in this chapter was published in *Optics Express* [3].

Finally, Chapter Nine is the conclusion to this dissertation. This chapter includes a summary of the research reported in this dissertation, and I present future research avenues in the work covered in Chapters Three to Nine.

### **1.3 New Contributions**

The key contributions presented in this dissertation include the following:

1. Design and analysis of a novel waveguide microcantilever deflection detection device.
2. Tolerance analysis for imperfect components in integrated depolarizer design.
3. Development of deep, vertical etch for PFCB polymers.
4. Fabrication of low loss single air interface bends in PFCB polymers.

## **CHAPTER 2**

### **BACKGROUND**

This chapter gives the reader basic information about the subject matter included in the next chapters. They are intended to aid in understanding the importance and motivation of the work in this dissertation. For further details the reader may consult the references.

#### **2.1 Microcantilevers for Sensing Applications**

In this section a brief overview of microcantilevers as sensors is included. The basic equations describing microcantilever deflection and resonance frequency are discussed. Finally, the most important detection methods available are described.

##### **2.1.1 Basics of Microcantilevers as Sensors**

Microcantilevers can serve as sensitive sensing devices because changes in the surrounding environment can modify certain characteristics of the cantilever such as deflection and resonant frequency, among others [4], [5], [6], [7]. Deflection occurs due

to surface stress induced by the adsorption of molecules on one side of the cantilever if properly sensitized [4], [5], [6]. This stress also causes a change in the cantilever's resonant frequency through a change in its spring constant and through mass loading from molecular adsorption. These, along with other parameters, such as amplitude and Q-factor, that are affected by molecular adsorption on the cantilever, can be detected simultaneously [4].

The basic equation that relates beam deflection due to surface stress was first derived in 1909 by Stoney [8]. It may be written as

$$\delta s_1 - \delta s_2 \approx \frac{\Delta z_l E_Y t_l^2}{4L_l^2(1-\nu)}, \quad (2.1)$$

where  $\delta s_1 - \delta s_2$  is the difference of the changes in surface stress of the cantilever's top and bottom surfaces,  $E_Y$  is Young's modulus,  $\nu$  is Poisson's ratio,  $t_l$  is the cantilever thickness,  $\Delta z_l$  is the cantilever deflection, and  $L_l$  its length. For instances in which Young's modulus isn't accurately known, Godin, et al. [6] derived the relation of cantilever deflection to surface stress for rectangular cantilevers as

$$\delta s_1 - \delta s_2 = \frac{4}{3(1-\nu)} \frac{L_l}{W_l t_l} k \Delta z_l, \quad (2.2)$$

where  $\delta s_1 - \delta s_2$  is the difference of the changes in surface stress of the cantilever's top and bottom surfaces,  $W_l$  is the width of the cantilever,  $L_l$  is its length,  $t_l$  its thickness,  $\nu$  is Poisson's ratio,  $\Delta z_l$  is the cantilever deflection, and  $k$  is the cantilever's spring constant (which can be calculated from the cantilever's resonant frequency and quality factor). With these relations we have a way to calculate the surface stress on a cantilever due to molecular adsorption by measuring its deflection.

The resonant frequency of a microcantilever is given by

$$f_r = \frac{1}{2\pi} \sqrt{\frac{k}{m^*}}, \quad (2.3)$$

where  $m^*$  is the cantilever's effective mass. The resonant frequency will change due to changes in the spring constant or changes in the effective mass. After molecular adsorption the resonance frequency can be expressed as

$$f_d = \frac{1}{2\pi} \sqrt{\frac{k + \delta k}{m^* + \delta m^*}}, \quad (2.4)$$

where  $f_d$  is the resonance frequency after the spring constant  $k$  undergoes a change,  $\delta k$ , and the effective mass increases or decreases (as would be the case with desorption) by  $\delta m^*$ . Additionally, the change in spring constant,  $\delta k$ , is related to the differential stress induced on the cantilever between its upper and lower surfaces by

$$\delta k = \pi^2 a \frac{(\delta s_1 - \delta s_2)}{4a_1}, \quad (2.5)$$

where  $n$  is a geometrical parameter that relates the effective mass of the lever to the beam's mass by  $m^* = am_b$ , and  $a$  and  $a_l$  are geometrical parameters, and  $\delta s_1$  and  $\delta s_2$  are the changes in the surface stress on the cantilever's top and bottom surfaces, respectively [4]. By measuring the resonance frequency of the cantilever we can get the spring constant if the mass loading is known or we can calculate the mass loading given that we know the cantilever's spring constant.

Microcantilevers have important advantages in sensing applications. These advantages are sensitivity, scalability to multielement arrays, and they can work in air, vacuum, or liquid environments [4]. In the next section we discuss the main detection mechanisms available as well as their advantages and disadvantages.

### 2.1.2 Detection Mechanisms

Among the detection mechanisms for cantilever deflection are optical beam deflection, piezoresistance, and capacitance. Optical beam deflection and piezoresistance are the main detection methods used. The most sensitive method is optical beam deflection followed by the piezoresistance method.

Optical beam deflection consists in reflecting a laser beam off the cantilever's surface onto a position sensitive detector (PSD) (see Figure 2.1 (a)). A deflection of the cantilever steers the beam to a different position on the PSD. Lang, et al. [9],[10] developed an array of eight microcantilevers as a chemical sensor using this method. Some of its drawbacks are scalability and “artificial” cantilever deflections. When scaling the number of levers to many more than eight, it becomes increasingly complicated to align the laser beams onto the levers' surface. On the other hand, the laser beam heats the cantilever slightly causing a measurement bias; and, localized changes to the refractive index of the medium the lever is in will cause the detection of “artificial” deflections because the beam's path will shift slightly. This limits the application of this detection method in liquids where bubbles would be a localized refractive index change.

The piezoresistance detection method consists on making piezoresistors on the cantilever by using doped silicon as the lever material [11] or placing a strain gauge resistor on the surface of the lever [12]. The lever is put into a Wheatstone bridge and when it bends, its resistance changes. These changes can be correlated to beam deflection (see Figure 2.1 (b)). Chow, et al. reported fabricating arrays of piezoresistive silicon microcantilevers with through-wafer electrical connections [13]. Additionally, Calleja, et al. have done so with polymer cantilevers with gold strain gauge resistors [14].

However, the scaling to arrays requires that the wiring goes through the wafer as in [13] so that the sensor can operate in liquids.

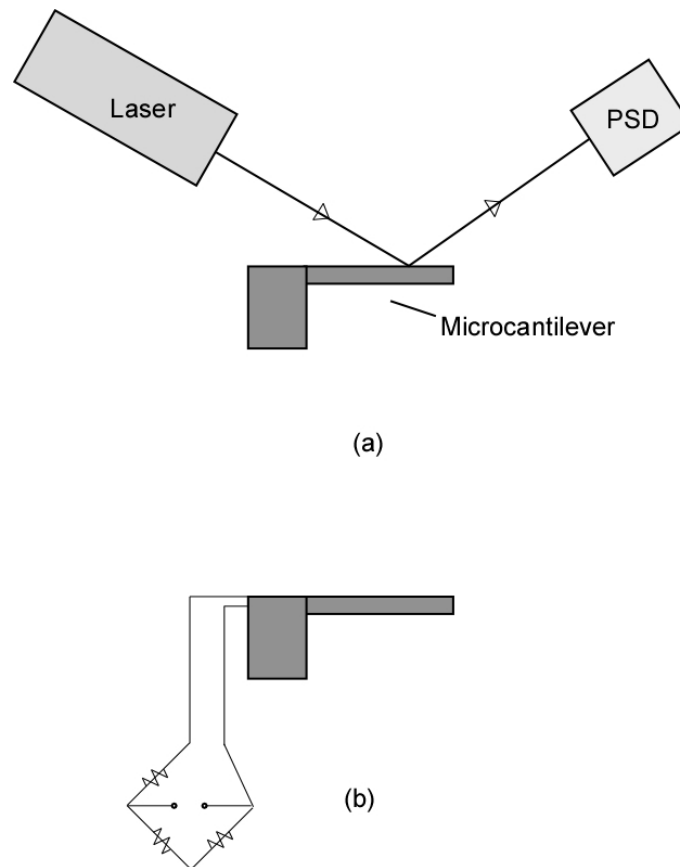


Figure 2.1. (a) Optical beam detection method and (b) Piezoresistive detection method.

### 2.1.3 Novel Photonic Microcantilevers

In Chapter Three of this dissertation, I present the design of a novel microcantilever beam deflection detection method. It consists of making the microcantilever a waveguide and coupling its output to a splitter structure. The splitting ratio of this structure is dependant on the vertical position of the incident optical radiation which comes from the waveguide microcantilever allowing the differential detection of optical power leaving the splitter structure. While waveguide microcantilevers have been used before for deflection detection, they used methods based on a single detector which

measures optical throughput. The details of this novel detection method are explained in Chapter Three.

## 2.2 Interferometric Fiber Optic Gyroscope

This section presents the basics of the Sagnac effect, which is the basis for the interferometric fiber optic gyroscope. Additionally, it discusses the typical inteferometer's configuration.

### 2.2.1 Fundamentals of Optical Rotational Sensing

The Sagnac effect is the basis for the interferometric fiber optic gyroscope (IFOG). It is observed when two coherent counterpropagating optical beams in a ring interferometer undergo an inertial rotation. This rotation produces a phase change that is proportional to the rotational rate [15]. It may be written as

$$\Delta\phi = \frac{8\pi A}{\lambda_o c} \Omega, \quad (2.6)$$

where  $A$  is the area of the ring resonator,  $\lambda_o$  is the wavelength of light in a vacuum,  $c$  is the velocity of light, and  $\Omega$  is the rotation rate. However, in an IFOG there are multiple turns of fiber. This increases the phase change for a given rotation rate by increasing the effective sensing area by the number of turns in the fiber coil. Thus, for an IFOG, considering that the fiber of length  $L_f$  is wound in a circle of diameter  $D_c$ , the phase shift is

$$\Delta\phi_{IFOG} = \frac{2\pi L_f D_c}{\lambda_o c} \Omega. \quad (2.7)$$

The interference pattern is sinusoidal:

$$I = 2I_f + 2I_f \cos(\Delta\phi_{IFOG}). \quad (2.8)$$

Thus, using the Sagnac effect, a ring interferometer can detect small rotational changes. Optical fiber improves its sensitivity by multiplying the sensing area by the number of turns around the coil. However, a longer optical fiber reduces the dynamic range because only a pi phase shift can be measured unambiguously and the phase change for a given rotation rate is proportional to the optical fiber length.

### 2.2.2 Typical IFOG Configuration

A typical IFOG consists of a light source, a 2x2 coupler, an optoelectronic integrated circuit (OEIC), and an optical fiber coil. The light source can be a laser diode or a superluminescent diode (SLD). The SLD, due to its broadband nature, reduces noise due to backreflection, backscattering, polarization cross-coupling, and the nonlinear Kerr effect [16]. On the other hand, the fiber coil may be made of polarization maintaining (PM) or single mode (SM) fiber. PM fiber coils aren't sensitive to small variations in stress. However, in SM fiber, the stress changes cause spurious birefringence. This birefringence changes the polarization state of the beam propagating in the fiber. Since, after the two counterpropagating beams recombine, they go through a polarizer, a randomly changing polarization state will make the throughput after the polarizer vary. The signal could fade entirely if the polarization state is orthogonal to the transmission state of the polarizer. This phenomenon is called polarization fading [17]. To fix this problem in SM fiber coils, depolarizers are added. Actually, two of them must be used (see Figure 2.2), one on each side of the coil, so fabrication tolerances don't degrade the

IFOG's performance excessively [18]. The details of this analysis can be found in Ref. [18].

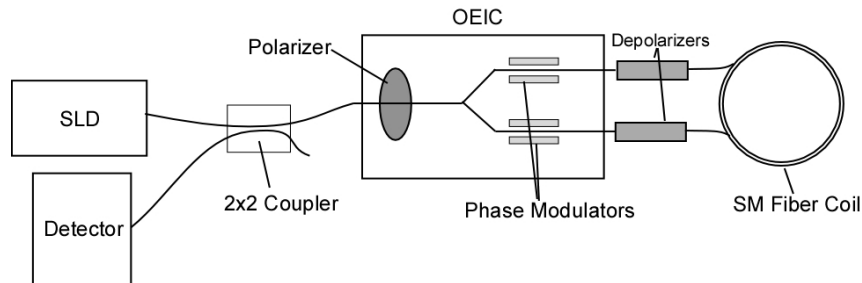


Figure 2.2. Typical IFOG configuration using a SM fiber coil and depolarizers.

In Chapter Four, the integration of the depolarizer into the OEIC is presented. By doing this, the cost of the IFOG may be reduced.

### 2.3 Polymer Plasma Etching

Plasma etching is a common step in microfabrication used to remove material in desired areas. It is usually preceded by a lithography step to define the features to be etched. The lithography step defines the etch mask. During the etch process, the etch mask is usually etched, too. Thus, the etch mask material must have an adequate selectivity (the ratio of the feature's etch rate to the mask's etch rate) for the etch mask to survive the process.

Etching occurs through two mechanisms: chemical reactions through surface adsorption and physical removal through ionic collisions [19]. The gas chemistry used for an etch process depends on the material to be etched. The gases must be chosen such that they react with the surface and create volatile compounds. These compounds are then

pumped out of the chamber. On the other hand, the physical mechanism depends on the ions' energy. They are accelerated by the bias voltage and collide with molecules of the material being etched. Additionally, they provide energy to stimulate chemical reactions.

Etch processes can be described as isotropic or anisotropic. In isotropic processes, the features are etched in all directions. This is undesirable for waveguide fabrication, but has other applications such as stripping. For anisotropic processes, features are etched primarily in the vertical direction. High anisotropy is needed for waveguide fabrication. For low loss waveguides, smooth sidewalls are also very important. And, in the fabrication of single air interface bends, anisotropy, sidewall smoothness, and sidewall verticality are critical for optimum performance.

Polymer materials are being seriously considered for waveguide components and integrated optical systems due to their compatibility with other materials, cost-effective patterning techniques, intrinsically high negative thermo-optic coefficients, low thermal conductivity, and now, their low optical absorption [20], [21]. However, many of these polymers are not photodefinable and plasma etching is required to define features during device fabrication. The need for these etch processes has prompted important development in highly anisotropic, smooth polymer etching [21], [22], [23], [24], [25].

Polymers are usually etched in an oxygen chemistry. Noble gases such as Argon or Helium may be added to increase the physical etching component. However, a purely physical etch is very slow [24] indicating that the etch rate is highly dependent on the reactive component of the etch. Other gases may be added to obtain a certain sidewall profile.

Charging and temperature effects have been reported to adversely affect anisotropy and sidewall verticality [26], [27], [28], [29]. Localized charging in the feature during etching alters the ions' trajectory. It can cause bowing, notching, or dovetailing (see Figure 2.3) of sidewalls especially when etching insulating materials such as polymers. Some research groups have gone to the use of neutral beams of oxygen for polymer etching to avoid the charging problem [29]. On the other hand, higher temperature helps molecules from the sidewall desorb, which degrades anisotropy. To reduce temperature effects, the sample may be cooled to cryogenic temperatures, which minimizes spontaneous etching of the sidewall (i.e., ion energy is needed to desorb the molecules) [21], [22]. However, a large temperature drop may cause stress related problems such as cracking or delamination due to a coefficient of thermal expansion mismatch between the substrate, which is typically silicon, and the polymer. Other ways to achieve highly anisotropic and vertical etching are using a high bias voltage or using an etch chemistry that passivates the sidewall to protect it from lateral etching. These are discussed in the next paragraphs.

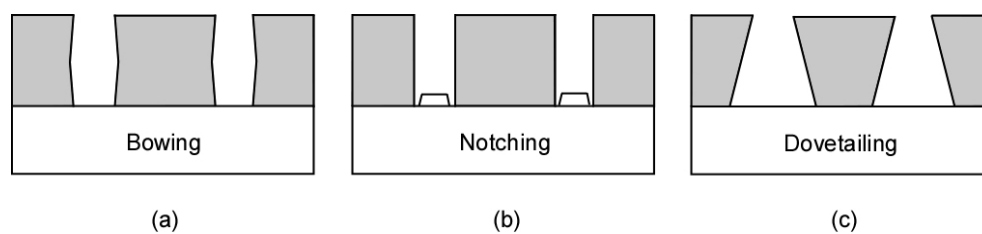


Figure 2.3. Etching profiles for different charging effects (a) bowing, (b) notching, and (c) dovetailing.

Increasing the bias voltage in an etch process makes the etch mechanism more physical than chemical. It is possible to obtain very high anisotropy in a pure oxygen etch

if the ion energy increases to levels greater than 120 eV [22]. However, this anisotropy is enhanced by erosion of the etch mask edge at similar rates as the sidewall edge etching [22]. In some applications, having this erosion well characterized and quantified may allow for successful device fabrication. However, in instances where arrays of features with spacing on the order of the mask erosion are of interest, this is highly undesirable.

If the right etch chemistry is chosen for a particular material, etch byproducts or reactive molecules stripped from the process gases in the plasma will deposit on the surface of the etch sample. Because the ion impact on the horizontal surfaces is much higher than on the sidewalls, this leads to protecting the sidewall, while the feature is being etched. This is called sidewall passivation. While this is desirable for high anisotropy, excess deposition can result in device contamination or cause the etch to stop in sub-micron features [27].

Both high bias etching and sidewall passivation alone have drawbacks. However, a balance in which the sidewall etch rate is identical to the passivation rate will result in a highly anisotropic etch profile [23]. Thus, an etch process must be developed to balance the sidewall etch rate with the passivation layer deposition rate. The development of polymer etch processing is discussed in Chapters Five and Seven for two different material systems.

## 2.4 Waveguide Bends

The need for higher packing densities in integrated optical circuits has spurred the development of many different concepts to achieve low loss compact waveguide bends. These concepts include simply bending a waveguide to form an arc [30], using microprisms [31], and adding a corner structure [32], [33], [34], [35]. Most of these are used for waveguides with both low and high refractive index contrast.

Arc bends consist in routing a waveguide along a circular path with a radius large enough to achieve high optical throughput as in Figure 2.4 (a). Analysis of mode propagation in a curved waveguide reveals that the mode tends to travel closer to the outer edge of the waveguide's core. This causes a mode mismatch at the interface with a straight waveguide. To compensate for this mismatch and increase bend efficiency, offsets may be introduced to improve the coupling [30]. However, the bend efficiency is still limited by the bend radius, which must be large enough so that radiation losses, which occur because the part of the mode traveling on the outside of the bend must travel a longer distance than the inside of the mode, are minimal.

The minimum bend radius for a high optical throughput arc depends on the refractive index contrast of the waveguide. For waveguides made on silicon on insulator (SOI) with a refractive index contrast of 58.6%, Vlasov, et al. reported a loss of only 0.086dB for a bend radius of one micron [36]. However, for material systems with low refractive index contrast on the order of one percent, the minimum bend radius is on the order of several millimeters. Etching trenches around the waveguide's core to increase the refractive index contrast, while adding tapers to reduce the coupling losses to straight

waveguides as shown in Figure 2.4 (b) reduces the minimum bend radius significantly but adds the footprint necessary for the taper sections [37]. Figure 2.4 shows a schematic of these two bends.

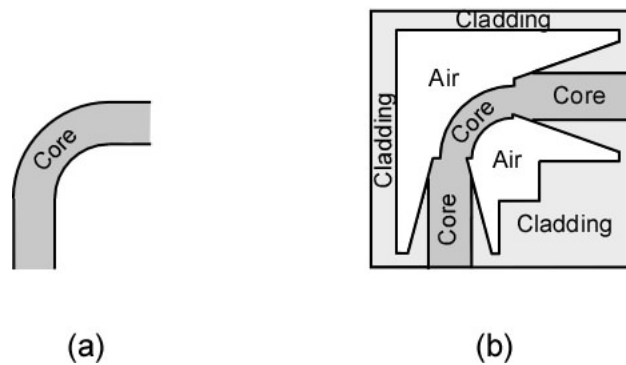


Figure 2.4. Schematic of arc bends: (a) simple arc bend and (b) arc bend with tapers and trenches around the core.

Corner structures that serve as a waveguide bend include resonance cavities [32], double bends at a corner [33], single or multiple air interfaces [34], and photonic crystal mirrors [35]. Of these methods, the first two work well in high refractive index contrast material systems and try to reduce the already small arc bend footprint, while the latter two can be applied for both high and low refractive index contrast waveguides. The corner resonance cavity depicted in Figure 2.5 (a) uses a resonator to achieve maximum transmission by tuning the cavity's properties [32]. The double corner bend takes advantage of index confinement to redirect the mode around the bend [33]. It can be seen in Figure 2.5 (b). Single air interface bends rely on total internal reflection to reflect the incident mode into the bent waveguide (Figure 2.5 (c)). When using these structures for low refractive index contrast waveguides, the maximum bend angle that can be achieved with high efficiency is limited by the refractive index of the waveguide's core. For

channel waveguides with a refractive index contrast around one percent, a core refractive index of 1.6 allows for highly efficient  $90^\circ$  bends. On the other hand,  $90^\circ$  high efficiency bends can also be realized using multiple interfaces as shown in Figure 2.5 (d). This kind of mirror relies partially on total internal reflection from the first interface and Bragg reflection from the rest of the interfaces [34]. Finally, a highly efficient photonic crystal mirror can be added at the corner of a waveguide bend. This approach utilizes the benefits of photonic crystals and combines them with the low loss nature of conventional waveguides while circumventing the problem of lossy photonic crystal waveguides (see Figure 2.5 (e)) [35].

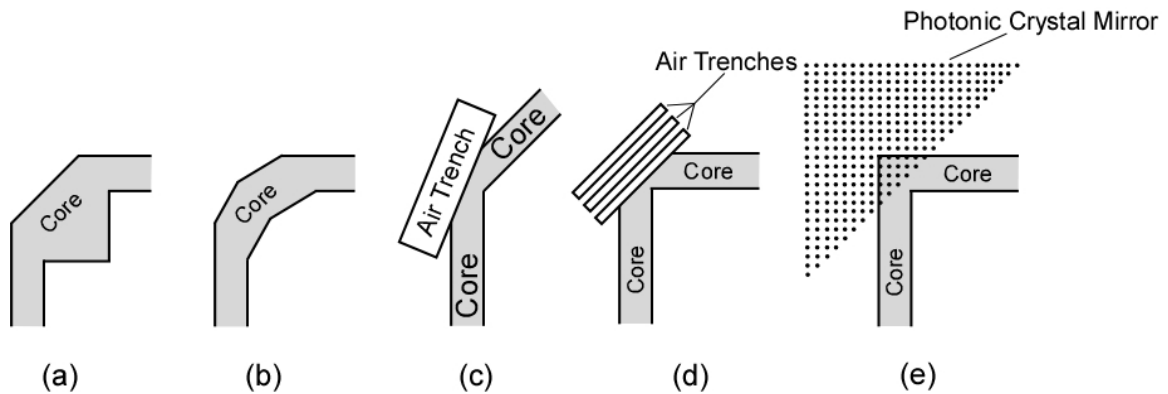


Figure 2.5. Corner bend structures (a) resonance cavity, (b) double corner mirror, (c) single air interface bend, (d) multiple air trench bend, and (e) photonic crystal mirror.

In this section we reviewed the methods used for making highly efficient compact waveguide bends. The bend that is the subject of Chapters Seven and Eight is the single air trench bend. While high efficiency single air trench bends have been demonstrated in high refractive index contrast waveguides [38], [39], [40]; the work in this dissertation demonstrates them in low refractive index contrast waveguides. In Chapters Seven and Eight, we will discuss the etch process for fabricating the trench first (Chapter Seven) and

then Chapter Eight discusses the fabrication and measurement of a  $45^\circ$  single air interface bend.

## **CHAPTER 3**

# **WAVEGUIDE MICROCANTILEVER DEFLECTION SENSOR DESIGN**

This chapter presents the design and analysis of a novel microcantilever detection method with applications in chemical and biological sensing. Initially, current microcantilever detection methods are briefly reviewed. Then, the design of the components for the sensor is presented. Additionally, the fundamental sensitivity limit for the cantilever sensor is explored. Finally, possible next steps in its development are proposed.

### **3.1 Introduction**

Currently, there is a need for chemical and biological sensors that are highly sensitive, scalable, and inexpensive to make. These sensors need to be able to detect very small amounts of a variety of chemical and biological agents in both vapor and liquid environments. In recent proposals to NSF [41], [42], Dr. Gregory Nordin proposed the use of an array of microcantilevers with a new kind of photonic transduction as a sensor platform applicable to a broad range of chemical and biological agents.

The new photonic transduction method consists of a waveguide microcantilever coupled with a deflection sensor. The sensor is composed of the waveguide that is part of the cantilever and a specially designed splitter structure in which the splitting ratio is dependent on the vertical position of the cantilever. While waveguide microcantilevers aren't a new concept, the detection method is novel. A schematic illustration of the sensor concept proposed by Dr. Gregory Nordin [41], [42] is shown in Figure 3.1. The research described in this chapter is focused on the design of the splitting structure and the analysis of the sensitivity of the resulting sensor.

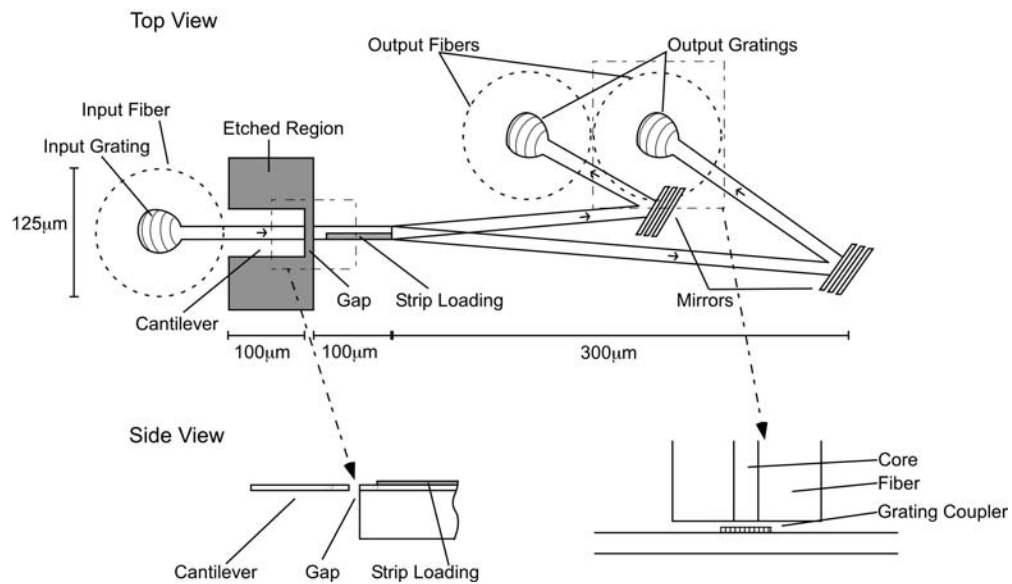


Figure 3.1. Schematic of waveguide microcantilever sensor for chemical and biological agents [41], [42].

### 3.2 Design and Analysis

The novel detection method relies on a splitter structure whose splitting ratio is dependent on the waveguide cantilever's deflection. In this section, we discuss the optical

component's design and the sensitivity analysis to find what is the minimum detectable deflection.

### 3.2.1 Component Design

A waveguide microcantilever sensor can be fabricated with different material systems. Typical materials for cantilevers are silicon and low stress silicon nitride. I designed the components in silicon nitride. The designed parts are the silicon nitride waveguide going to the cantilever and the waveguide splitting structure. They were designed using a commercial beam propagation package, RSoft's Beamprop 5.0.

The device is fabricated on a silicon wafer coated with silicon dioxide and low stress silicon nitride. The rib waveguide is defined by etching 100nm into the nitride layer as seen in Figure 3.2 (a). Finally, silicon dioxide is deposited on the nitride as an overcladding.

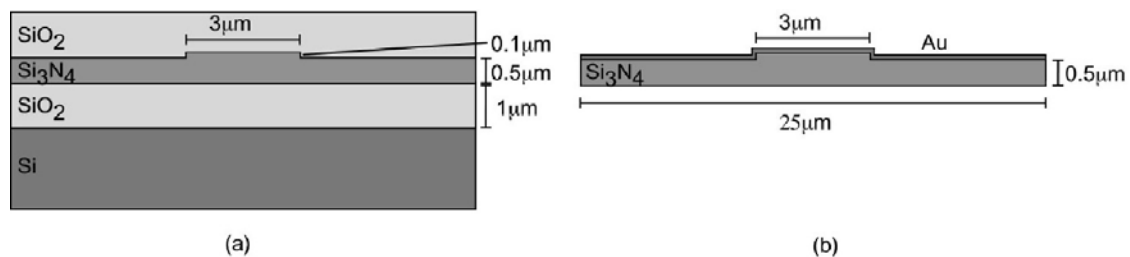


Figure 3.2. (a) Cross-section of waveguide leading to cantilever and (b) cantilever cross-section with gold coating for detection chemical and biological agents.

The splitter consists of a y-branch with an asymmetric high refractive index strip loading on the common path as shown in Figure 3.3. The asymmetric strip loading causes

the splitting ratio to be dependent on the vertical position of the waveguide microcantilever.

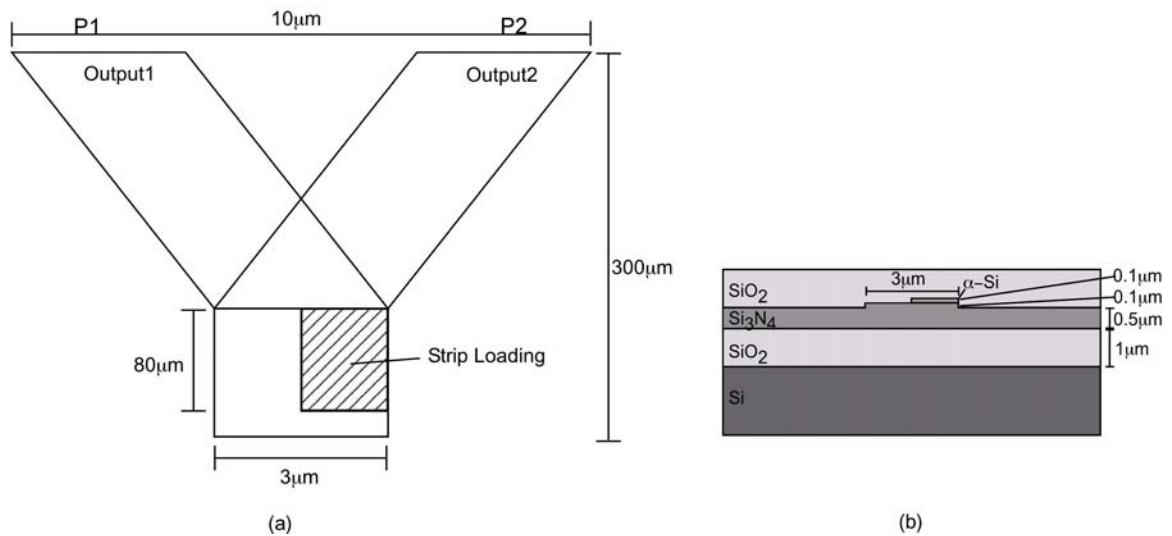


Figure 3.3. (a) Schematic top view of the y-branch splitter and (b) waveguide cross-section at the strip loading level.

The y-branch splitter was simulated by launching the zero order mode of the waveguide leading into the cantilever into the common path of the splitter offset by  $0.5\mu\text{m}$  to the right of the waveguide's center (Figure 3.3 (a)). The result of varying the input height is shown in Figure 3.4. It can be seen that the splitting varies as the microcantilever's height changes. Thus, this design can be used to measure the cantilever's deflection. However, we must still analyze whether it has the potential to have high sensitivity.

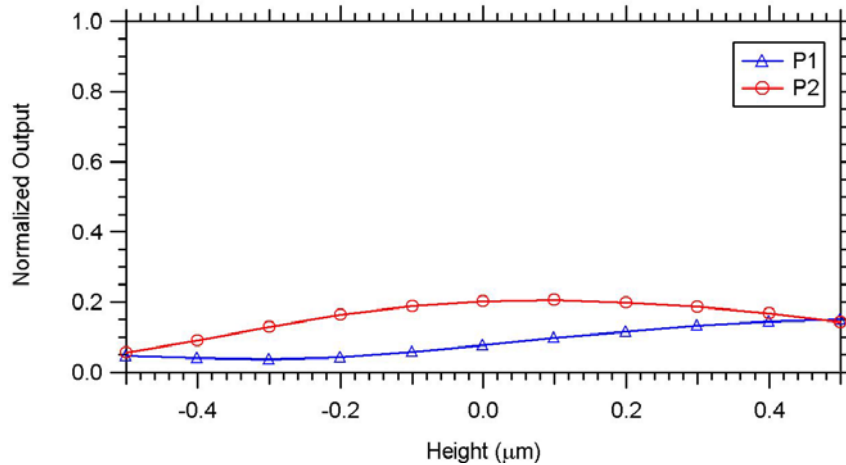


Figure 3.4. Normalized output power versus the height of the incident mode on the y-branch splitter common path. The origin of the x axis represents the incident mode profile from the cantilever in perfect alignment with the y-branch common waveguide.

### 3.2.2 Sensitivity Analysis

The microcantilever sensitivity depends on the accuracy to which we can detect the radiation propagating through the output fibers. In general, most noise sources can be minimized such that shot noise is the dominant noise source. This is inherent to the statistical nature of light when treated as a stream of photons. Thus, there is no way to completely suppress it. Additionally, its variance is proportional to the incident power. Because of these reasons, this analysis will consider a shot noise limited detector and study its impact on the sensitivity that can be achieved with the waveguide microcantilever sensor.

As described in the previous section, the splitter structure was designed by introducing an asymmetry that results in a power variation when the input beam is incident at different heights. To analyze the sensitivity of the sensor, let's start by defining the contrast as

$$K = \frac{I_1 - I_2}{I_1 + I_2}, \quad (3.1)$$

where  $I_1$  and  $I_2$  are the currents measured at detectors 1 and 2, respectively.

To consider the effects on  $K$  by small changes in  $I$ 's, we differentiate on both sides:

$$\Delta K = \frac{\Delta I_1 - \Delta I_2}{I_1 + I_2} + \frac{(\Delta I_1 + \Delta I_2)(I_2 - I_1)}{(I_1 + I_2)^2}. \quad (3.2)$$

After further simplification we have

$$\Delta K = \frac{2(\Delta I_1 I_2 - \Delta I_2 I_1)}{(I_1 + I_2)^2}. \quad (3.3)$$

The equation for the detector current is [43]

$$I_x = \frac{e\eta_x P_x \lambda_o}{hc}, \quad (3.4)$$

and its standard deviation due to shot noise is [43]

$$\sigma_x = \sqrt{\frac{2e^2 \eta_x B P_x \lambda_o}{hc}}, \quad (3.5)$$

where  $x = 1, 2$  corresponding to each detector,  $e$  is the electron charge,  $\eta$  is the detector's quantum efficiency,  $B$  is the bandwidth,  $P_x$  is the power that reaches the detector,  $\lambda_o$  is the laser's wavelength,  $h$  is Planck's constant, and  $c$  is the velocity of light in a vacuum.

Assuming  $\eta_1 = \eta_2 = \eta$ , letting  $\sigma_x = \Delta I_x$  and substituting (3.4) and (3.5) into (3.3), the result reduces to

$$\Delta K = \frac{\sqrt{8hc} \sqrt{\frac{B}{\lambda_o \eta}} \sqrt{P_1 P_2^2 - P_2 P_1^2}}{(P_1 + P_2)^2}. \quad (3.6)$$

In order to pursue this analysis further, we must estimate how much power will reach the detectors. A reasonable loss budget is given in Table 3.1.

Table 3.1. Loss Budget for waveguide microcantilever sensor.

Loss Origin	Magnitude (dB)
Fiber to Waveguide	3-5
Waveguide Propagation	0.5
Waveguide to Cantilever	0.5
Cantilever Propagation	0.2
Cantilever to Splitter	1
Splitter Propagation	13
Air trench Mirrors	0.5
Waveguide to Fiber	3-5
<b>Total</b>	<b>21.7-25.7dB</b>

Following the data from Figure 3.4, we can calculate the contrast as defined by (3.1). Figure 3.5 shows the contrast versus the height of the cantilever. As we can see, the contrast has a linear relationship to the cantilever height in the range of  $-0.2\mu\text{m}$  to  $0.4\mu\text{m}$  with a slope of  $-0.846\mu\text{m}^{-1}$ .

Assuming that  $10\mu\text{W}$  is coupled into the receiver waveguide and the losses are as in Table 3.1 above, the power at the detectors for the deflection that results in the greatest shot noise (height =  $-0.2\mu\text{m}$ ,) which occurs at the lowest output power, is  $P_1 = 0.577\mu\text{W}$  and  $P_2 = 0.151\mu\text{W}$ . Inserting these values into (3.4), choosing a bandwidth of  $B = 1\text{ KHz}$ ,  $\eta = 0.75$ , and evaluating (3.6), we find that  $\Delta K = 7.64 \times 10^{-6}$ . If we operate in the linear range of Figure 3.5, the relationship between the contrast and the vertical position of the cantilever can be simply expressed as  $K = my + b$ . Differentiating this expression with respect to  $y$ , the change in position may be expressed relative to a change in contrast as  $\Delta y = \Delta K/m$ . The contrast change of  $\Delta K = 7.64 \times 10^{-6}$  calculated above can be substituted to find the cantilever deflection noise level for this case, which is  $\Delta y = 9.03\text{pm}$ . Thus, the fundamental limit for cantilever deflection sensitivity is very small. It can be driven still lower by increasing the optical power incident on the splitter structure.

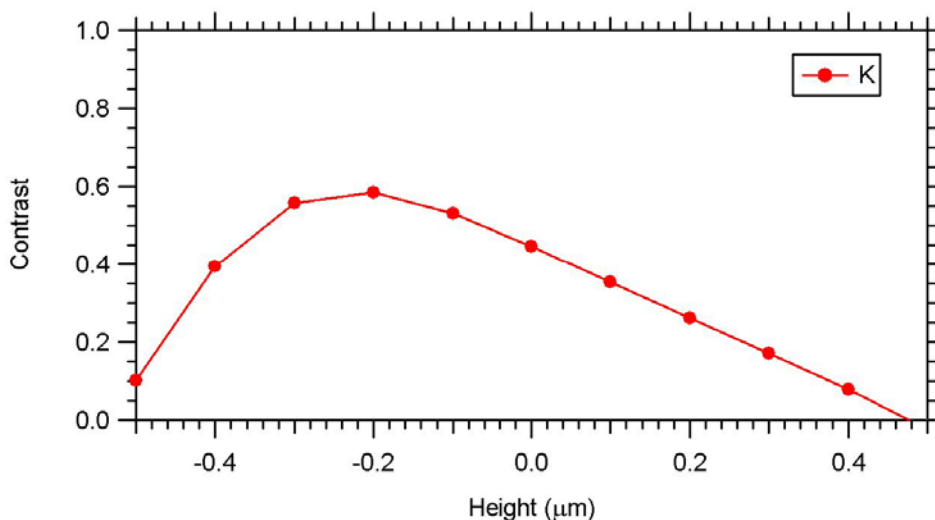


Figure 3.5. Contrast after splitter output versus cantilever height.

The above calculation considers  $10\mu\text{W}$  coupled into the receiver waveguide.

Figure 3.6 shows the tip deflection sensitivity,  $\Delta y$ , as a function of optical power incident on the splitter structure. The required source power needs to be only 6 dB higher than the amount of light coupled into the receiver waveguide considering the loss budget table. A single mW-scale optical source should be able to supply a large number of microcantilevers permitting the microcantilever sensing system to be scaled to large arrays.

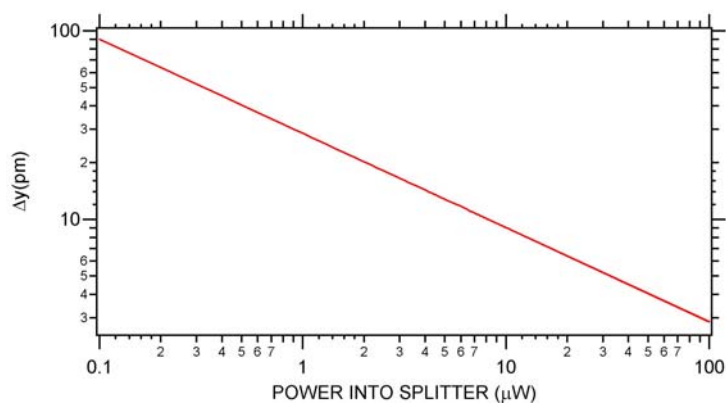


Figure 3.6. Fundamental sensitivity limit for cantilever deflection detection as a function of optical power incident on the splitter structure.

Thus, this sensor meets the high sensitivity requirement and can be fabricated in arrays that could be sensitized for different chemical or biological reagents. Additionally, the material system considered here is compatible with typical semiconductor microfabrication techniques.

### **3.3 Conclusion**

The analysis in the previous sections shows that the design for this novel waveguide microcantilever sensor for biological and chemical agents has high sensitivity and can be fabricated in arrays. These two properties are very important when trying to develop a sensor that can be used to detect very small amounts of a broad range of chemical or biological agents. An obvious application is in the detection of gases dangerous to humans. However, it may also be used in the medical industry in the detection of chemicals in a subject's bloodstream which could provide data for diagnosis of diseases or to the development of new drugs and their interactions with tissue.

Even though these results show great promise, there is much work that must be done to develop the sensor. Potential areas for future research can be divided into design and analysis, experimental proof of the splitter's functionality, and fabrication and testing of waveguide microcantilever sensors. In the area of design and analysis, the splitter structure can be designed for other attractive material systems such as silicon or polymers. While the y-branch splitter offers simplicity and performance, other structures should be explored for, potentially, greater benefits in measurement capabilities. On the other hand, an obvious step in the development of this concept is the experimental proof that the y-

branch splitter can achieve the high sensitivity that our analysis has shown. To do this, the structure must be fabricated and tested to verify the dependence of the splitting ratio on the height of the input beam and to encounter possible unforeseen difficulties in its practical application. Finally, the waveguide microcantilever sensor must be fabricated and tested. During testing, the deflection of the cantilever should be measured by an alternate method to compare with the data produced by the sensor itself.

## **CHAPTER 4**

### **INTEGRATED OPTIC DEPOLARIZER**

#### **DESIGN AND ANALYSIS**

This chapter presents the design and analysis of the integrated optic depolarizer. After a short overview of an interferometric fiber optic gyroscope, the system's concept is presented. This work follows from the original proposal for the integrated depolarizer, its concept, and the design of the polarizing beamsplitter and mirror by Dr. Lixia Li [2]. Here the importance of the beam delay and its dependence on the source's correlation function is addressed. Additionally, a tolerance analysis for imperfect components and its impact on the degree of polarization are presented. Finally, the components that I designed for this system are discussed.

#### **4.1 Introduction**

As discussed in Chapter Two, interferometric fiber optic gyroscopes (IFOGs) are composed of a source, splitter, polarizer, phase modulator, fiber coil, coupler, and detector as shown in Figure 4.1. The two types of fiber coils used are polarization-maintaining (PM) fiber and single mode (SM) fiber coils. IFOG's with PM fiber coils

have a high cost because PM fiber is expensive. The use of SM fiber reduces the cost, but depolarizers must be added into the system (refer to Chapter Two for the details).

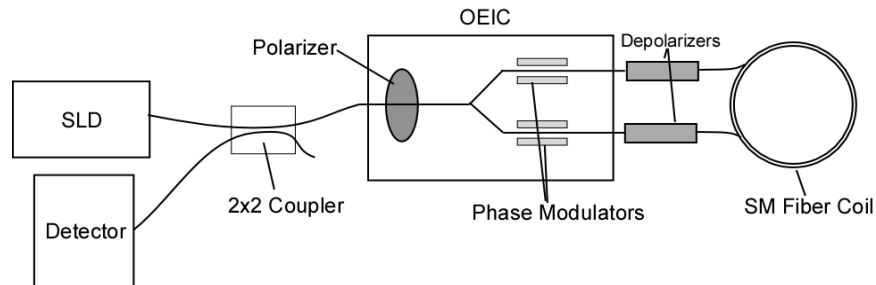


Figure 4.1. Typical IFOG configuration in which an IOC performs the polarizing, splitting and phase modulating functions. Since the coil is made of single mode fiber depolarizers are used.

Current research on interferometric fiber optic gyroscopes (IFOGs) is trying to integrate its components into a planar lightwave circuit (PLC) to reduce its size and cost. However, depolarizers for low cost IFOGs must reduce the degree of polarization (DoP) to five percent or lower. These depolarizers are usually made by splicing two pieces of PM fiber whose slow axes are at  $45^\circ$  [44], [45]. For this research, we are trying to integrate this function into the IOC that contains other parts of the IFOG, such as the polarizer, splitter, and phase modulator.

## 4.2 System Concept

In order to make an integrated optic depolarizer, the incident beam of light must be split in two, then a temporal delay must be introduced into one of the beams such that they become mutually incoherent, and when they are recombined, the beam will be depolarized. To achieve a low DoP, the two beams must have an opposite polarization

state in the Poincare Sphere and their intensities must be evenly matched. Because the system's analysis requires the addition of incoherent light, Jones vector analysis can't be used. Instead, Stokes vectors are required. They can be graphically represented by the Poincare Sphere (Figure 4.2). In this representation, each axis on the sphere represents a different component of the vector. The sphere's radius, ranging between 0 and 1, represents the DoP. At the very center of the sphere light is depolarized, while at the surface it is completely polarized. If two collinear beams of light with opposite polarization states  $S_a$  and  $S_b$  are combined, their addition will result in a single point at the center of the sphere, which represents fully depolarized light.

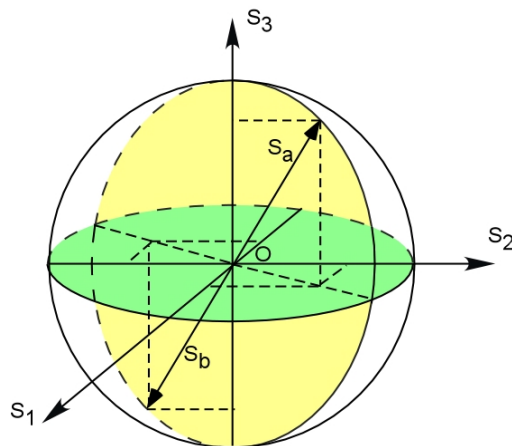


Figure 4.2. Poincare Sphere representation of the Integrated Optic Depolarizer concept [2].

The system we propose in Figure 4.3 will take an incident beam with an out of plane polarization (TM) and transform its polarization state into one that has equal magnitude in both TE and TM components. Then, a polarizing beam splitter (PBS) will separate each component into different paths. One of the beams will be delayed a precise amount to operate at a minimum on the source's coherence function (discussed in the

next section). Finally, the beams will be recombined using another PBS and the output will be depolarized light.

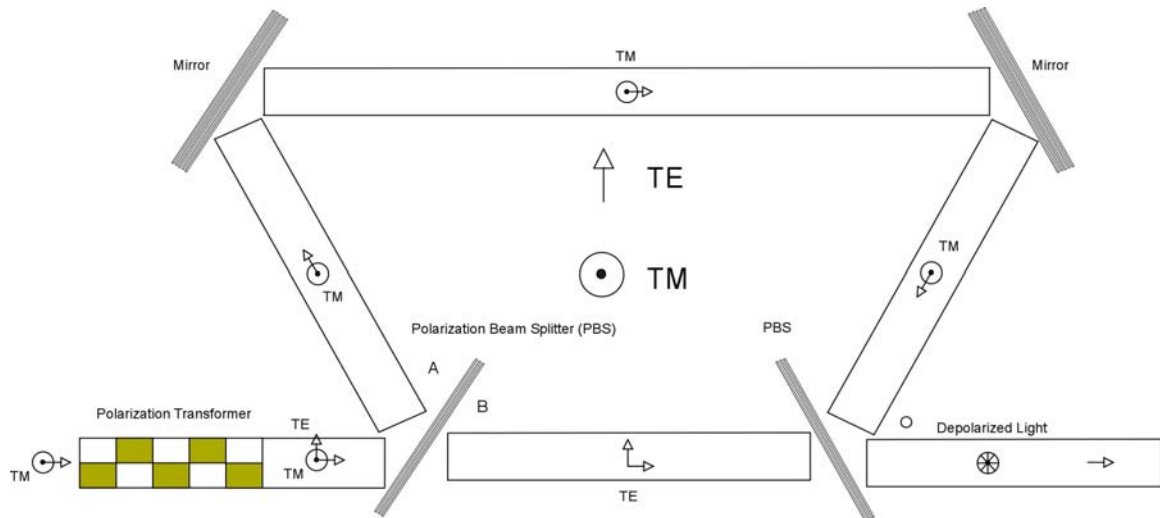


Figure 4.3. Integrated Optic Depolarizer Layout.

#### 4.2.1 Beam Delay

The propagation delay that must be introduced into one of the beams has to be carefully chosen. It depends on the precise spectral content of the source, which must have a broad spectrum. Typically, superluminescent diodes (SLDs) are used as a source for IFOGs. Every SLD has a slightly different spectrum. Additionally, their spectrum is not an ideal Gaussian curve; it usually has a certain amount of spectral ripple. Manufacturers will usually specify this parameter as a worst case for their units. Because of this spectral ripple, the autocorrelation function of the SLD will have secondary peaks. For the IFOG application it is desirable that the depolarizers operate at 40dB below the coherence peak or lower.

#### 4.2.2 Measurement of the Source's Autocorrelation Function

The key concept in the integrated optic depolarizer (IOD) design is the incoherent addition of both beam's intensities after the second PBS. The depolarizer must be designed specifically for the intended source and its coherence function, which is the normalized autocorrelation function. Therefore, it is necessary to know what its autocorrelation function is.

The autocorrelation function can be measured directly, by using a Michelson interferometer, or it can be indirectly deduced by measuring the source's optical spectrum. We chose the latter method because a high precision optical spectrum analyzer was available.

In order to understand how the autocorrelation function can be calculated from the source's optical spectrum and its importance in the design of the depolarizer, let's consider the autocorrelation of the electric field,  $R(\tau)$  [46], as

$$R(\tau) = \langle E^*(t)E(t + \tau) \rangle, \quad (4.1)$$

where  $E$  is the time-varying electric field and the brackets  $\langle \rangle$  indicate "time averaged".

The Einstein-Wiener-Khintchine theorem states that the spectral density and autocorrelation of a time averaged quantity form a Fourier Transform pair [47]. Thus,

$$S(f) = F\{R(\tau)\} = \int_{-\infty}^{\infty} R(\tau)e^{-j2\pi f\tau} d\tau \quad (4.2)$$

and

$$R(\tau) = F^{-1}\{S(f)\} = \int_{-\infty}^{\infty} S(f) e^{j2\pi f\tau} df . \quad (4.3)$$

After the Polarization Transformer (refer to Figure 4.3 throughout this analysis), the electric field is

$$\vec{E}(t) = \frac{E(t)}{\sqrt{2}} \begin{bmatrix} 1 \\ e^{j\delta} \end{bmatrix}, \quad (4.4)$$

where  $\delta$  is a phase delay introduced between the two polarization components, TE and TM, by the polarization transformer.

Then, after the PBS, the reflected field is

$$\vec{E}_r(t) = \frac{E(t)}{\sqrt{2}} \begin{bmatrix} 0 \\ e^{j\delta} \end{bmatrix} \quad (4.5)$$

and the transmitted field is

$$\vec{E}_t(t) = \frac{E(t)}{\sqrt{2}} \begin{bmatrix} 1 \\ 0 \end{bmatrix}. \quad (4.6)$$

The reflected component (TM) will propagate through a longer path, which will introduce a temporal delay  $\tau$  with respect to the TE (transmitted) component. Thus, after the second PBS, the reflected field is

$$\vec{E}_{rr}(t) = \frac{E(t+\tau)}{\sqrt{2}} \begin{bmatrix} 0 \\ e^{j\delta} \end{bmatrix} \quad (4.7)$$

and the transmitted field is

$$\vec{E}_u(t) = \frac{E(t)}{\sqrt{2}} \begin{bmatrix} 1 \\ 0 \end{bmatrix}. \quad (4.8)$$

Therefore, the electric field for the recombined beams is

$$\vec{E}_T(t) = \frac{E(t)}{\sqrt{2}} \hat{x} + \frac{E(t+\tau)}{\sqrt{2}} e^{j\delta} \hat{y}. \quad (4.9)$$

At this point, we will introduce the coherency matrix to study the necessary conditions for  $\vec{E}_T(t)$  to be depolarized. The coherency matrix [46] is defined as

$$C = \begin{bmatrix} \langle E_x E_x^* \rangle & \langle E_x E_y^* \rangle \\ \langle E_y E_x^* \rangle & \langle E_y E_y^* \rangle \end{bmatrix}, \quad (4.10)$$

for  $\vec{E} = E_x \hat{x} + E_y \hat{y}$ .

From the coherency matrix, the DoP [46] is defined as

$$DoP = \sqrt{1 - \frac{4|C|}{(C_{xx} + C_{yy})^2}}, \quad (4.11)$$

where  $|C|$  is the determinant of the coherency matrix.

For the DoP to be zero, the following conditions must be met [46]

$$C_{xx} = C_{yy} \text{ and } C_{xy} = C_{yx} = 0. \quad (4.12)$$

The first condition means that the intensity of both beams needs to be equal. On the other hand, for the second condition to be fulfilled we have that

$$\langle e^{j\delta} E(t+\tau)E^*(t) \rangle = \langle E(t)E^*(t+\tau)e^{-j\delta} \rangle = 0. \quad (4.13)$$

Since the phase terms are independent of time, we may take them out of the time averaging brackets.

$$e^{j\delta} \langle E(t+\tau)E^*(t) \rangle = e^{-j\delta} \langle E(t)E^*(t+\tau) \rangle = 0. \quad (4.14)$$

Moreover, for the above equation to be satisfied, the terms inside the brackets have to be zero. Thus,

$$\langle E(t+\tau)E^*(t) \rangle = \langle E(t)E^*(t+\tau) \rangle = 0. \quad (4.15)$$

Therefore, for the addition of the two beams to result in depolarized light, their autocorrelation must be zero, which means they must be mutually incoherent. Hence, the depolarizer must be designed such that the TM polarized beam is temporally delayed so that we are at a minimum in the autocorrelation function.

We used an optical spectrum analyzer to measure the spectral density of the SLD. Using the Einstein-Wiener-Khintchine theorem, we calculated the autocorrelation by taking the inverse FFT of the generated data. Figure 4.4 (a) shows the measured optical spectrum of the SLD that will be used to test the depolarizer, while part (b) shows its autocorrelation function. It can be seen that for certain delays, the autocorrelation function is at a minimum. For the IOD, we must introduce the delay required to be at the first minimum, which would result in the smallest device possible. The simplest way to do this is to introduce an effective path length difference such that, taking the effective index of the propagating mode into account, it takes that beam  $\tau = \frac{\Delta d \cdot n_{eff}}{c}$  longer to reach the second PBS. In this case, for this particular SLD, a time delay of 1.44ps is needed, which means  $\Delta d$  should be 265 $\mu\text{m}$ .

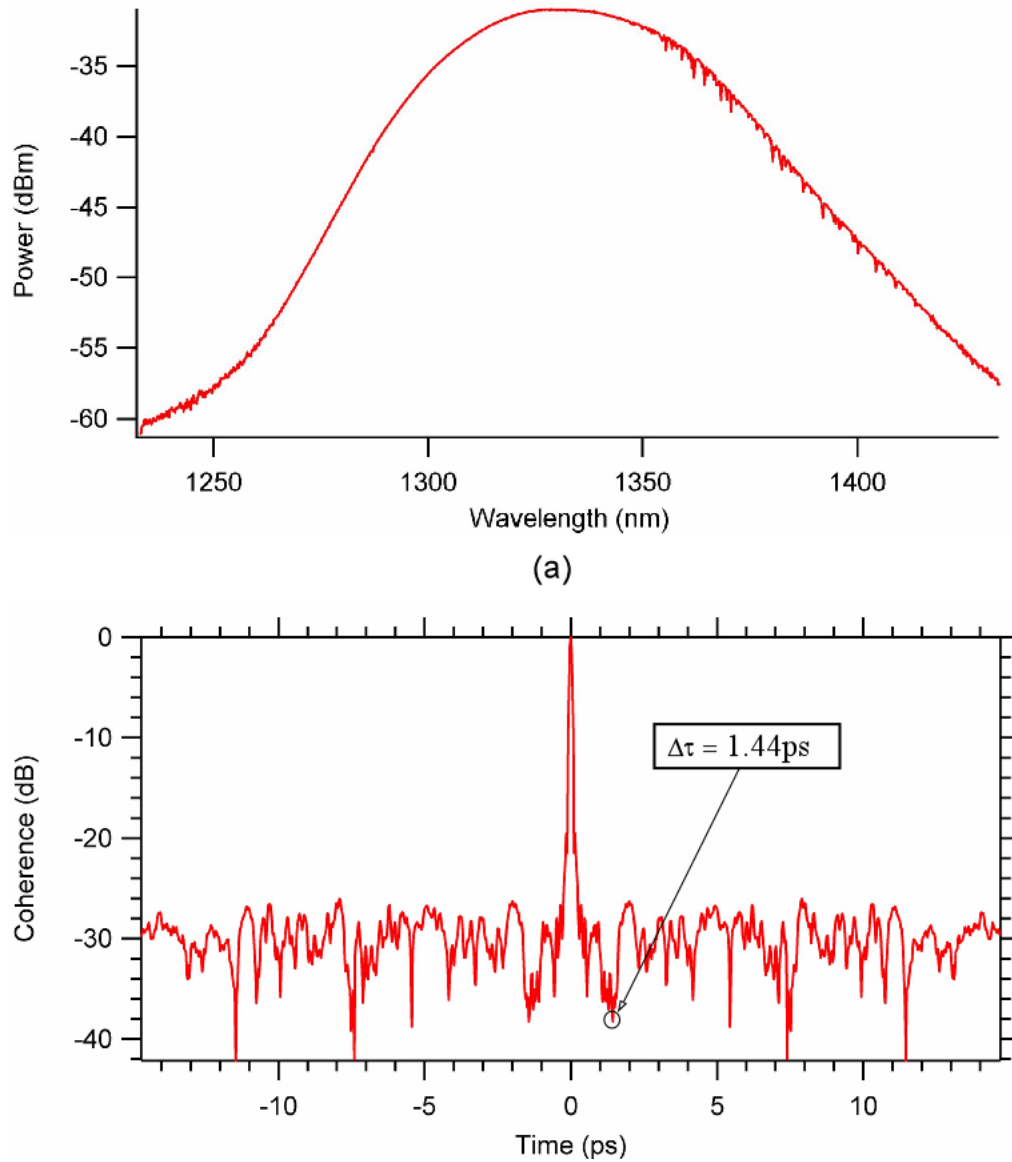


Figure 4.4. a) SLD's optical spectrum as measured by an ANDO 6315E spectrum analyzer and b) Coherence function calculated from the optical spectrum data. Note that the first minimum occurs at a time of 1.44ps.

### 4.2.3 DoP Tolerance Analysis

If ideal components, such as the polarization transformer, the mirrors and the PBSs, are considered, then the resulting DoP will be its minimum, limited only because the two beams aren't completely incoherent. However, the mirrors won't reflect 100% of the incident radiation and the PBS won't reflect one polarization state perfectly while completely transmitting the other one (there will be some leakage of unwanted polarization components in both legs of the ring). Similarly, the output of the polarization transformer won't have equal TE and TM components. All of these imperfections will affect the DoP. In particular, for the IFOG, the DoP must be under 0.05 to attain high performance.

To account for these component imperfections, we used Jones and Stokes vectors to analyze the integrated depolarizer. Consider the Jones vector for the output of the polarization transformer (Refer to Figure 4.3) as

$$\hat{e} = \begin{pmatrix} \kappa \\ \Delta e^{j\delta} \end{pmatrix}, \quad (4.16)$$

where  $\Delta$  and  $\kappa$  are the fraction of TM and TE polarized light, respectively, and  $\Delta^2 + \kappa^2 = 1$ .

After the first PBS, the *reflected* polarization state will be given by

$$\hat{e}_A = \begin{pmatrix} \varepsilon_A \kappa \\ I_R \Delta e^{j\delta} \end{pmatrix}, \quad (4.17)$$

where  $I_R$  and  $\varepsilon_A$  are the reflected portions of TM and TE polarized light, respectively, and  $I_R^2 + \varepsilon_A^2 = 1$ . Similarly, the *transmitted* component will be given by

$$\hat{e}_B = \begin{pmatrix} \kappa I_t \\ \varepsilon_B \Delta e^{j\delta} \end{pmatrix}, \quad (4.18)$$

where  $\varepsilon_B$  and  $I_t$  are the transmitted fractions of TM and TE polarized light, respectively, and  $I_t^2 + \varepsilon_B^2 = 1$ .

The mirrors are designed to provide maximum reflectivity for the expected polarization component in the longer arm. The leaked component won't undergo an efficient reflection. The Jones matrix representing the mirrors is given by

$$Mirror = \begin{pmatrix} \varepsilon_M & 0 \\ 0 & I_M \end{pmatrix}. \quad (4.19)$$

After both reflections, but before the second PBS we have that

$$\hat{e}_{M2} = \begin{pmatrix} \kappa \varepsilon_A \varepsilon_M^2 \\ I_R I_M^2 \Delta e^{j\delta} \end{pmatrix}. \quad (4.20)$$

Then, at point O the field that was reflected at the second mirror is reflected by the second PBS,

$$\hat{e}_{or} = \begin{pmatrix} \kappa \varepsilon_A^2 \varepsilon_M^2 \\ I_R^2 I_M^2 \Delta e^{j\delta} \end{pmatrix}. \quad (4.21)$$

At the same point, but for the transmitted component that propagates through the shorter leg, the polarization state is

$$\hat{e}_{ot} = \begin{pmatrix} \kappa I_t^2 \\ \varepsilon_B^2 \Delta e^{j\delta} \end{pmatrix}. \quad (4.22)$$

At this point, the two beams are incoherent and Jones vectors can't be used to describe their interaction. Instead, we converted them into Stokes vectors. Thus,

$$S_{or} = \begin{pmatrix} \kappa^2 \varepsilon_A^4 \varepsilon_M^4 + I_R^4 I_M^4 \Delta^2 \\ \kappa^2 \varepsilon_A^4 \varepsilon_M^4 - I_R^4 I_M^4 \Delta^2 \\ 2I_R^2 I_M^2 \kappa \varepsilon_A^2 \varepsilon_M^2 \Delta \cos \delta \\ -2I_R^2 I_M^2 \kappa \varepsilon_A^2 \varepsilon_M^2 \Delta \sin \delta \end{pmatrix} \quad (4.23)$$

and

$$S_{ot} = \begin{pmatrix} \kappa^2 I_t^4 + \varepsilon_B^4 \Delta^2 \\ \kappa^2 I_t^4 - \varepsilon_B^4 \Delta^2 \\ 2I_t^2 \kappa \varepsilon_B^2 \Delta \cos \delta \\ -2I_t^2 \kappa \varepsilon_B^2 \Delta \sin \delta \end{pmatrix}. \quad (4.24)$$

The Stokes vector for the combined beams is simply their addition:

$$S_o = \begin{pmatrix} \kappa^2 \varepsilon_A^4 \varepsilon_M^4 + I_R^4 I_M^4 \Delta^2 + \kappa^2 I_t^4 + \varepsilon_B^4 \Delta^2 \\ \kappa^2 \varepsilon_A^4 \varepsilon_M^4 - I_R^4 I_M^4 \Delta^2 + \kappa^2 I_t^4 - \varepsilon_B^4 \Delta^2 \\ 2(I_R^2 I_M^2 \kappa \varepsilon_A^2 \varepsilon_M^2 \Delta + I_t^2 \kappa \varepsilon_B^2 \Delta) \text{Cos} \delta \\ -2(I_R^2 I_M^2 \kappa \varepsilon_A^2 \varepsilon_M^2 \Delta + I_t^2 \kappa \varepsilon_B^2 \Delta) \text{Sin} \delta \end{pmatrix}. \quad (4.25)$$

The Stokes vector components are defined as

$$S = \begin{pmatrix} s_0 \\ s_1 \\ s_2 \\ s_3 \end{pmatrix}, \quad (4.26)$$

and the DoP as

$$DoP = \frac{\sqrt{s_1^2 + s_2^2 + s_3^2}}{s_0}. \quad (4.27)$$

Thus, from  $S_o$ , the Stokes vector components are

$$s_0 = \kappa^2 \varepsilon_A^4 \varepsilon_M^4 + I_R^4 I_M^4 \Delta^2 + \kappa^2 I_t^4 + \varepsilon_B^4 \Delta^2 \quad (4.28)$$

$$s_1 = \kappa^2 \varepsilon_A^4 \varepsilon_M^4 - I_R^4 I_M^4 \Delta^2 + \kappa^2 I_t^4 - \varepsilon_B^4 \Delta^2 \quad (4.29)$$

$$s_2 = 2(I_R^2 I_M^2 \kappa \varepsilon_A^2 \varepsilon_M^2 \Delta + I_t^2 \kappa \varepsilon_B^2 \Delta) \text{Cos} \delta \quad (4.30)$$

$$s_3 = -2(I_R^2 I_M^2 \kappa \varepsilon_A^2 \varepsilon_M^2 \Delta + I_t^2 \kappa \varepsilon_B^2 \Delta) \text{Sin} \delta. \quad (4.31)$$

And, the DoP is given by the relation

$$DoP = \frac{\sqrt{(\kappa^2 \varepsilon_A^4 \varepsilon_M^4 - I_R^4 I_M^4 \Delta^2 + \kappa^2 I_t^4 - \varepsilon_B^4 \Delta^2)^2 + 4(I_R^2 I_M^2 \kappa \varepsilon_A^2 \varepsilon_M^2 \Delta + I_t^2 \kappa \varepsilon_B^2 \Delta)^2}}{\kappa^2 \varepsilon_A^4 \varepsilon_M^4 + I_R^4 I_M^4 \Delta^2 + \kappa^2 I_t^4 + \varepsilon_B^4 \Delta^2}. \quad (4.32)$$

Ideally, the PBS would block the entire TM component for transmission and it would not reflect any part of the TE component, which means  $\varepsilon_A$  and  $\varepsilon_B$  would be equal to zero. In this case, the second and third terms would go to zero, while the first term's magnitude would depend on the balance between the two polarization components exiting the polarization transformer, therefore, making the DoP very small. The small TM transmitted component and TE reflected component in the PBSs cause the second and third terms to be nonzero. Careful inspection of these terms points out that there are no subtracted quantities. Thus, their balance does not affect the DoP. The only way to compensate for their adverse effect is to find a way to leak these components out of the system before the beams recombine.

The PBS for the depolarizer, designed by Dr. Lixia Li [2] using the 2D FDTD code developed at the Nano and Micro Devices Center, has an  $I_R^2 = 0.97$ , an  $\varepsilon_A^2 = 0.03$ , an  $I_t^2 = 0.96$ , and an  $\varepsilon_B^2 = 0.04$ . The mirrors have an  $I_M^2 = 0.99$  and an  $\varepsilon_M^2 = 0.09$ . We generated the plots for the DoP based on the previous analysis for the original depolarizing ring configuration. The parameter that we varied was the fraction of TM power incident on the depolarizing ring. The results are shown in the red curve of Figure 4.5. We can see from the plot that the window at which the DoP would be under

five percent is from a fraction of the incident power with TM polarization of 49% to 51%. This places a tight tolerance on the polarization transformer fabrication tolerances.

The addition of a PBS in between the two original ones as shown in Figure 4.6, results in the blue curve in Figure 4.5. As we can see, the minimum DoP is now about one percent and it remains under five percent for a  $\pm 2\%$  of  $\Delta^2$  centered around 49%. The use of this additional PBS will introduce additional losses and its benefits in DoP must be weighed versus its additional loss.

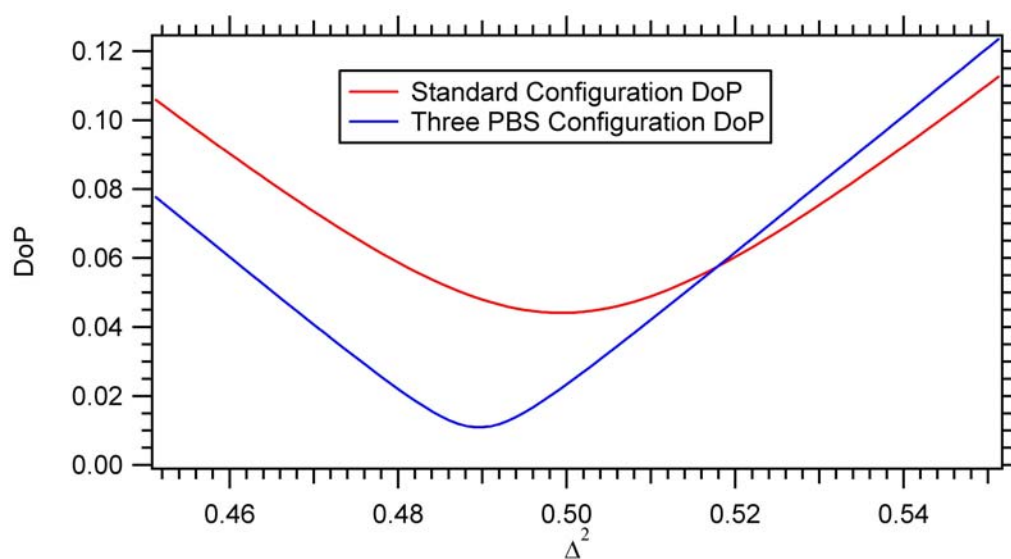


Figure 4.5. Degree of Polarization versus fraction of incident power with a TM polarization state on the depolarizing ring. As we can see, the addition of the third PBS reduces the DoP, though it will cause additional losses.

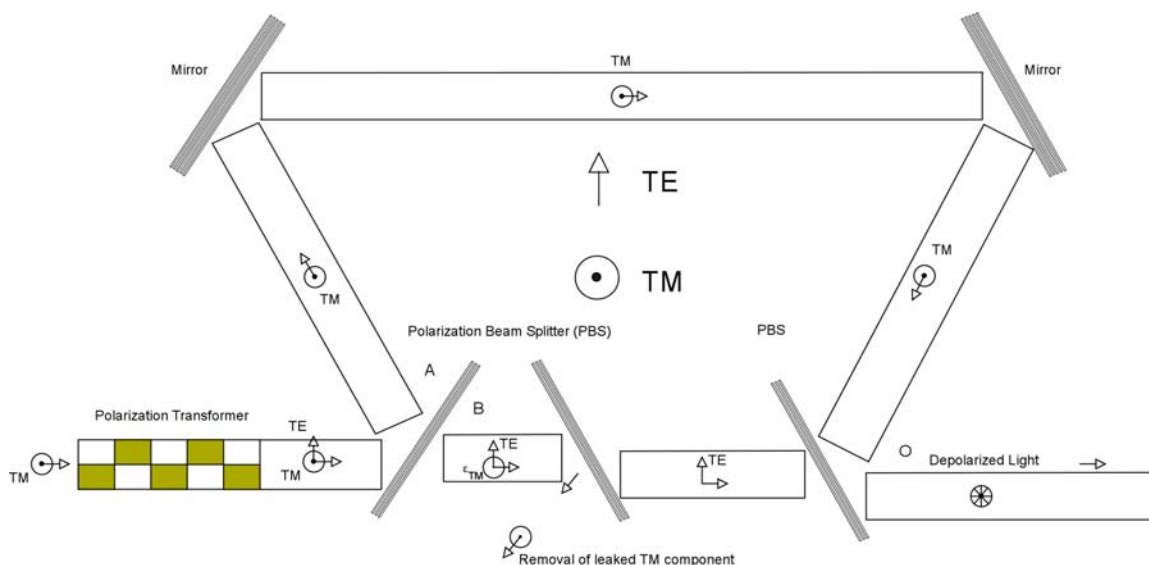


Figure 4.6. Three PBS depolarizing ring configuration. The middle PBS allows TE polarized light to be transmitted and significantly attenuates the unwanted TM polarization component that leaked through the first PBS by reflecting it away from the depolarizing ring.

This analysis provides insight into how component imperfections will affect the DoP. To achieve high depolarization, the beams' intensities from both legs must be nearly equal. This balance depends on the incident polarization state of the beam and on the performance of the components. For instance, a mirror that won't reflect 100% of the power incident on it might not be significantly detrimental if this loss helps deliver balanced intensities at the output waveguide. If some TM light is transmitted by the PBS instead of reflected, this component should be leaked out of the system and not allowed to recombine at the output. This is what the three PBS configuration (see Figure 4.6) attempts to do. By adding the third PBS, the leaked TM component is diminished and the DoP reduced. The reduction in DoP by introducing an additional PBS must be weighed against the additional loss that would be introduced into the device. If the loss is tolerable,

then adding the PBS increases the tolerance on the polarization transformer and reduces the lowest DoP attainable.

### **4.3 Design of Required Components**

The four components for the IOD were designed using numerical simulations. Dr. Lixia Li generated the depolarizer concept and designed the mirror and PBS using a 2D FDTD code [2]. I designed the waveguide and the polarization transformer using Fimmwave/Fimmprop.

#### **4.3.1 Waveguide Design**

The objective of this design was to determine the required dimensions for the circuit's waveguides to be single mode and to reduce the effective  $\Delta n$  between the core and the cladding. The necessity to meet contractual requirements fixed the materials for the core and the cladding. Additionally, a ridge waveguide structure was mandated. The simulations were made using Fimmwave 4.0 (Photon Design, UK).

The waveguide was defined as shown in Figure 4.7 in Fimmwave. The materials system for the IOD is PI-2525 polyimide for the core and NOA 71 Norland optical adhesive for the upper and lower cladding. The refractive indices used in the simulations are shown in Table 4.1. The rib height was varied while keeping the total height (rib height + slab height) at 3  $\mu\text{m}$ . Creating this structure was simple in Fimmwave and the mode solver was set to calculate 20 modes. Because Fimmwave works by calculating the eigenmodes of the waveguide structure, one can't assign a specific number to each of the

guided modes. Instead, they should be inspected and their side power loss calculated in order to decide whether they would propagate or leak out. To do this it is necessary to use the side power loss parameter to identify leaky modes because the reflective boundary conditions that Fimmwave uses won't discriminate between guided and radiation modes. To accelerate the design process we also used the Waveguide Scanner in Fimmwave. This allows the user to vary a parameter and calculate, among others, effective index and side power loss. After doing this for waveguides of several widths and varying the rib height, the optimum waveguide was found to have a rib height of  $0.7\mu\text{m}$ , a slab height of  $2.3\mu\text{m}$ , and a width of  $3.5\mu\text{m}$ . A narrower waveguide didn't provide a smaller  $\Delta n$ , while the rib height of  $0.7\mu\text{m}$  allows for a  $0.1\mu\text{m}$  etch tolerance for fabrication. It is important to point out that for this structure, higher order modes require  $\sim 5\text{mm}$  of propagation to attenuate to five percent of their initial power.

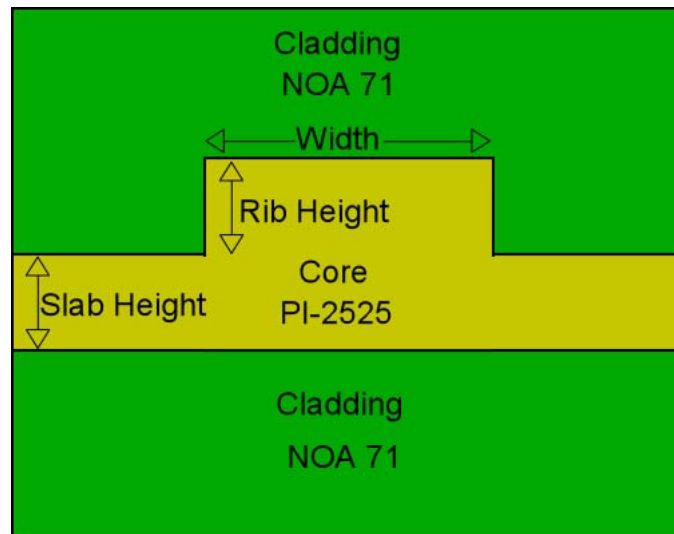


Figure 4.7. Waveguide Cross-section.

Table 4.1. Refractive indices for IOD materials system.

Material	Refractive Index	
	TE (in-plane)	TM (out-of-plane)
PI-2525	1.656	1.640
NOA71	1.548	1.548

#### 4.3.2 Polarization Transformer

The polarization transformer has to be designed to take a linear polarization state (TE or TM) and transform it into any polarization state of equal magnitude for the in-plane (TE) and out-of-plane (TM) components. Their relative phase is not important to the rest of the structure. In the literature, polarization converters, which take horizontally polarized light and convert it into vertically polarized light, have been demonstrated [48], [49]. This has been done using high index contrast materials, which shortens their length and facilitates their fabrication. In this case, the polymer material system used for the gyro depolarizer has a much smaller refractive index contrast.

The basic principle behind the polarization transformer is the coupling of light from the fundamental mode of out-of-plane polarization (TM) to the fundamental mode of in-plane polarization (TE). This can be done by introducing a periodic asymmetric strip loading on the waveguide [50] so that this coupling occurs (See Figure 4.8). The length of the strip loading sections, the strip loading material, its thickness, and the number of necessary periods are critical in defining the output polarization state of the waveguide mode. Many different materials can be chosen. As long as there is a way to fabricate the strip loading on the waveguide and that the material properties are

controllable to within a particular tolerance, the fabrication of the polarization transformer should be feasible.

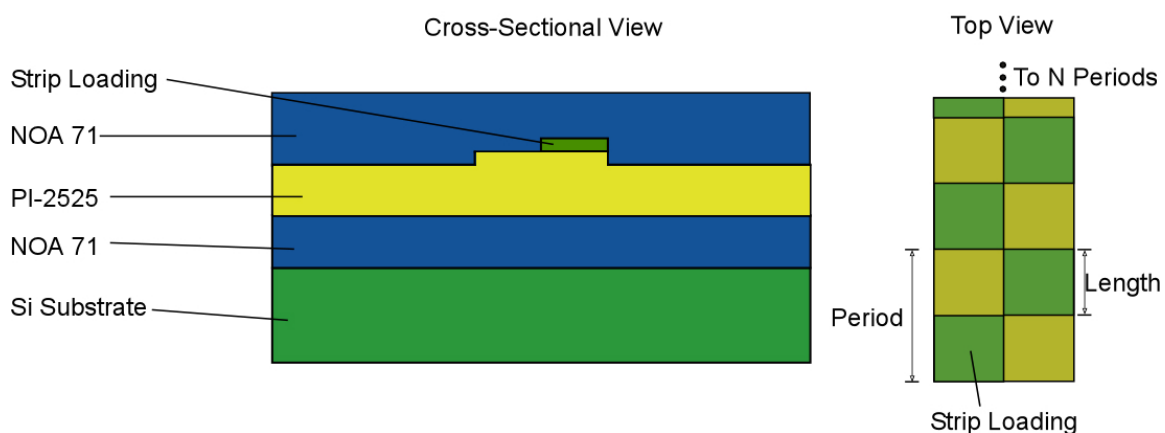


Figure 4.8. Periodic Asymmetric Strip Loading for the Polarization Rotator. The length, thickness, refractive index, and the number of periods have to be carefully designed to obtain the desired polarization transformation.

We compared several materials for the strip loading: silicon, silicon nitride, core material, and silicon dioxide. The first two materials required very thin layers (<60nm) and control over variations in thickness would be difficult because a very small change would represent a large percentage of the nominal thickness. The third one, the core material, looked promising but controlling the etch to achieve the same thickness every time is difficult. The fourth material, silicon dioxide, seems to be the most promising because a 10% change in a nominal thickness of 300nm would still yield results within our tolerances. However, silicon dioxide has the drawbacks of requiring a longer device to achieve the polarization transformation and its index of refraction must be controlled to within 0.01. It is important to note that silicon and silicon nitride had tighter requirements for the index of refraction; the core material shouldn't have this problem, though, because the change would happen to the waveguide and the "strip loading."

We used Fimmprop to simulate this structure. By varying the strip loading section length and the number of periods, we found that the polarization transformer would consist of 24 periods of  $133.5\mu\text{m}$  long sections (two sections per period) with an index of refraction of 1.44 for a total device length of 6.4mm. This makes the device rather long and another possibility for realizing the polarization transformer was proposed by Cai, et al. Their device is very short but has some fabrication challenges that must still be resolved [51]. Nonetheless, at this point our baseline plan is to use this design as the polarization transformer.

#### **4.4 Conclusion**

In this chapter we have presented the design and analysis for the integrated optic depolarizer. The main concept to achieve depolarization consists in separating the equal magnitude polarization components and delaying one of them precisely into a minimum of the beam's coherence function and then recombining them. The design and analysis considers tolerances for the various components to set requirements for fabrication. However, our efforts are still ongoing to fabricate all the components for the IOD. In the next chapter, we detail the progress in the fabrication of the beamsplitter and mirror structures.

## **CHAPTER 5**

### **INTEGRATED OPTIC DEPOLARIZER**

#### **ETCH DEVELOPMENT**

This chapter presents the results for two main etch chemistries for etching small feature, high aspect ratio trenches in a polymer material system. The materials are Norland Optical Adhesive and Polyimide. One of the etch chemistries was based on a high bias oxygen process, while the second one was based on sidewall passivation with sulfur. The results are illustrated with scanning electron microscope images.

#### **5.1 Introduction**

The components of the integrated optic depolarizer (IOD) that are the most difficult to fabricate are the polarizing beam splitter and the five layer mirrors. The main reasons are feature size, alignment, and the etch depth necessary for the air trench to affect the entire waveguide mode. The small features, of around  $0.5\mu\text{m}$ , can be patterned with optical or ebeam lithography. While it would be challenging for optical contact lithography, a stepper can achieve the necessary resolution and has the potential for meeting the alignment requirements. On the other hand, ebeam lithography can meet both

the feature size and alignment requirements. So, even though lithography poses a challenge, there is enough previous work in semiconductor processing that feature size and alignment aren't challenges as big as achieving the necessary etch depth, while maintaining a straight, vertical sidewall with low surface roughness. Thus, we started the focus of the fabrication development for the IOD by working on developing an etch recipe that would yield straight, vertical sidewalls with low surface roughness.

## **5.2 Etch Development**

We started the etch development by spinning films of approximately  $4\mu\text{m}$  of Norland NOA 71 on silicon wafers and later moved on to stacks with the three layers that the waveguides would have, which consisted of approximately  $4\mu\text{m}$  of NOA 71 followed by about  $3\mu\text{m}$  of polyimide PI-2525 and another  $4\mu\text{m}$  of NOA 71. We explored two main etch chemistries: oxygen, helium, and tetrafluoromethane; and oxygen and sulfur hexafluoride. Additionally, we initially used  $2\mu\text{m}$  features patterned on top of the polymer films and later moved on to  $0.5\mu\text{m}$  features, which are around 100nm smaller than the smallest designed air trench.

### **5.2.1 Oxygen, Helium, and Tetrafluoromethane**

Our first goal in the etch development was to determine how etch parameters such as power, chamber pressure, and gas flows affected the etch profile. To achieve this, samples with the polymer films on silicon wafers were prepared. The etch mask used was silicon dioxide and its thickness was increased as the etch times increased. To define the

features first we patterned photoresist with contact lithography and etched the silicon dioxide in a reactive ion etcher (RIE). Each sample was then etched in an inductively coupled plasma reactive ion etcher (ICP-RIE) with different etch parameters followed by imaging with a scanning electron microscope (SEM) to determine the etch quality, anisotropy, and depth of the trenches.

The first etch run on NOA 71 with oxygen left lots of small structures at the bottom of the trench commonly referred to as “grass” as can be seen in the top left image in Figure 5.1. The first hypothesis on what was causing the “grass” was that the Norland adhesive had some sulfur in it which the oxygen wasn’t etching and that adding tetrafluoromethane would fix this. This hypothesis was suggested by another group at the Army’s Aviation and Missile Command led by Dr. Paul Ashley who had worked with this material previously. We introduced tetrafluoromethane and helium to the etch chemistry. What we found was that the tetrafluoromethane did help in removing the “grass,” but that its effectiveness was also dependent on the coil power (see top right and bottom center images in Figure 5.1). A high enough coil power together with a small amount of tetrafluoromethane completely removed the etch “grass.”

After fixing the “grass” problem, we proceeded to etch the whole stack of polymer layers. We used the same recipe that produced no “grass.” With six minutes, the etch went through the whole stack and stopped at the silicon wafer (see Figure 5.2). There was some visible undercut, although it was impossible to measure from these images. Using data from other etches we estimate the undercut to be around  $0.5\mu\text{m}$  on each side. This means that the standing structure’s width is only on the order of  $1\mu\text{m}$ . It is clear that with this recipe you can’t etch a  $0.5\mu\text{m}$  feature to the same depth because the

undercutting will etch it away. However, for the IOD, the etch depth needs to be six microns, versus the eleven micron etch depth where this undercut was observed. Thus, even though it is still too much undercut, assuming the undercut rate is the same when etching smaller features, it seemed like a good starting point for the 0.5 $\mu$ m features.

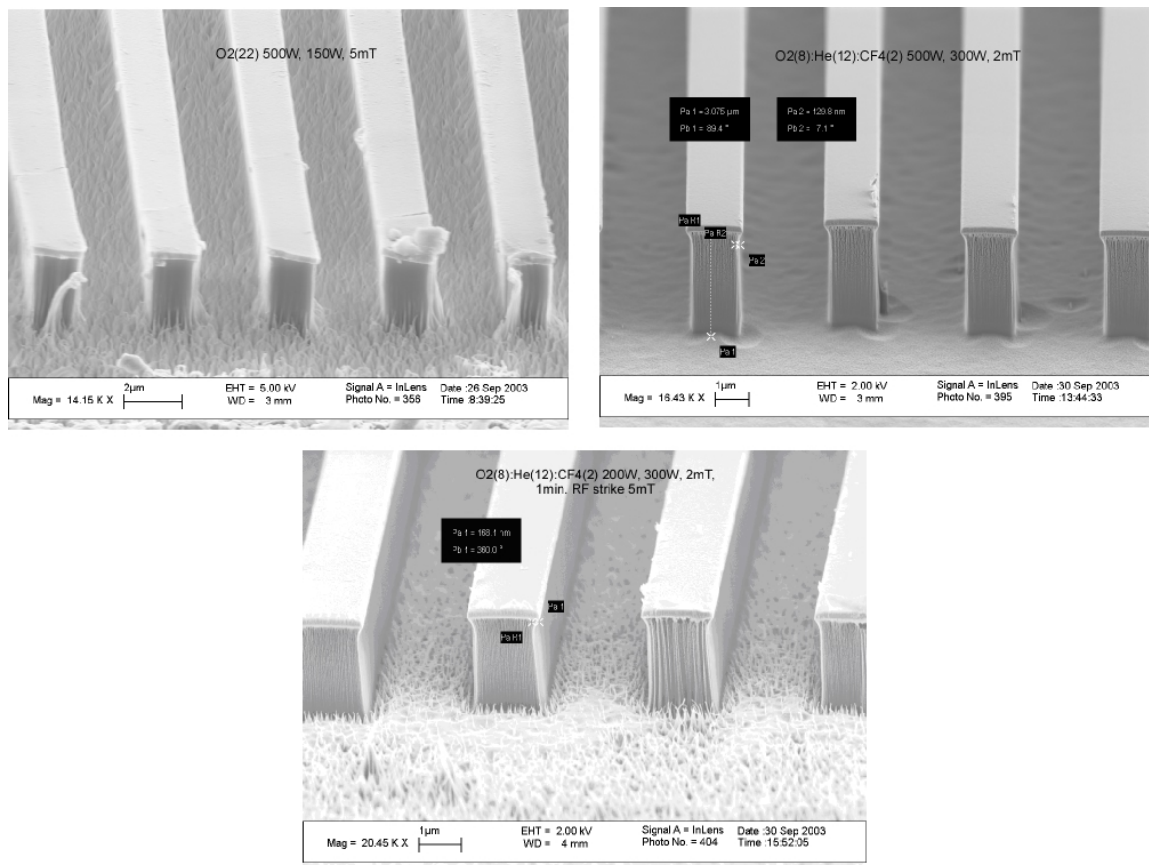


Figure 5.1. (Top left) NOA 71 etched with 22 sccm of oxygen, 500W of coil power, 150W of platen power, and a chamber pressure of 5mT. Notice the “grass on the bottom of the etched polymer. (Top right) NOA 71 etched with 8 sccm of oxygen, 12 sccm of helium, and 2 sccm of tetrafluoromethane, 500W of coil power, 300W of platen power, and a chamber pressure of 2mT. The grass didn’t appear with this recipe. (Bottom center) NOA 71 etched with 8 sccm of oxygen, 12 sccm of helium, and 2 sccm of tetrafluoromethane, 200W of coil power, 300W of platen power, and a chamber pressure of 2mT. The grass reappeared when reducing the coil power. The coil power affects the appearance of grass significantly.

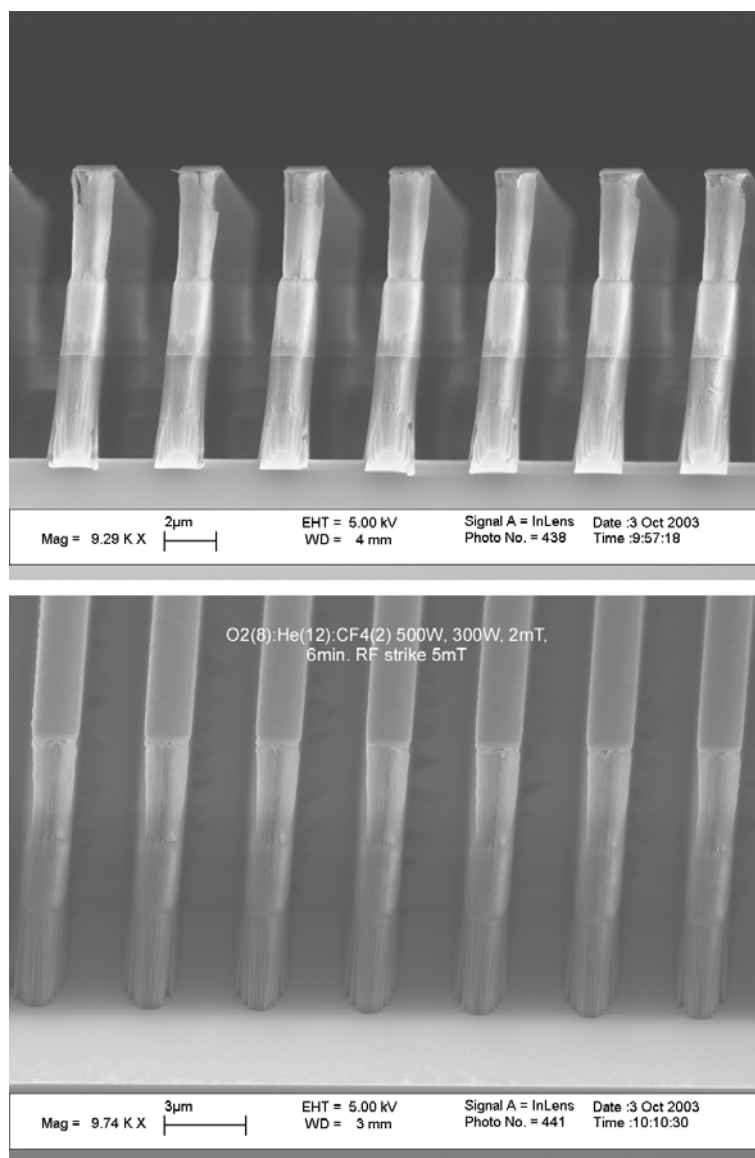


Figure 5.2. Six minute etch in ICP-RIE of  $2\mu\text{m}$  features on full polymer stack.

However, the undercut rate increased when etching the  $0.5\mu\text{m}$  features. As can be seen in Figure 5.3, which was etched for only two minutes with a recipe whose only difference with the one just described above was that the coil power was reduced to 300W from 500W (in an attempt to reduce the undercut rate), the features are barely standing due to undercutting. The etch just started to go into the polyimide layer. Thus, a new approach must be taken to have a successful process. In the next section, we explore

the use of a passivating species to protect the sidewalls and reduce undercutting during etching.

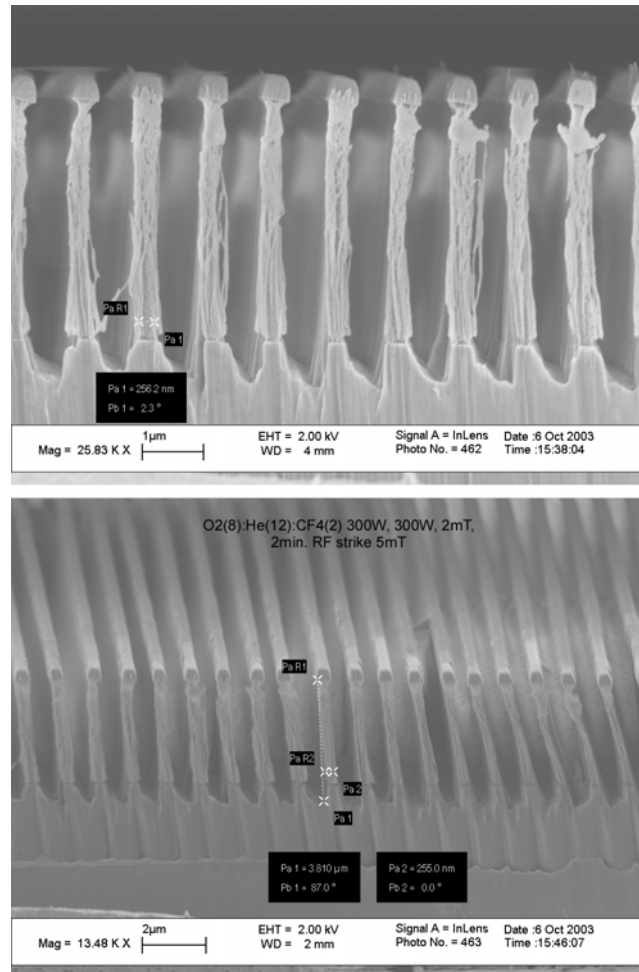


Figure 5.3. Two minute etch in ICP-RIE on  $0.5\mu\text{m}$  features. Notice the severe undercutting while the etch has barely gone into the polyimide layer.

### 5.2.2 Oxygen and Sulfur Hexafluoride

Since we couldn't eliminate the undercutting problem by etching with a high bias power and a low pressure, we moved on to the use of a passivating species, which is deposited on the sidewall during the etch. Thus, the lateral etch will attack the passivating species instead of the polymer's sidewall. In a literature search, we found that Pons, et al.

[22] had proposed the use of sulfur as a passivating species. Sulfur is a good candidate because its vapor pressure is low enough to condense at typical operating chamber pressures and thus deposit on the sidewalls. For the ICP-RIE tool at Nano and Micro Devices Center (a Surface Technology Systems Advanced Silicon Etcher ICP-RIE), the only gas we had that contained sulfur was sulfur hexafluoride. The drawback between this gas and sulfur dioxide, which was used by [22] is that it contains fluorine. Gas chemistries with fluorine will etch many of the etch mask materials that we typically use. In particular, the etch mask we had been using, silicon dioxide, etches in fluorine chemistries. Thus, we changed the etch mask material to aluminum and ran a set of samples while varying several process parameters.

Samples were coated with NOA 71, about  $3.6\mu\text{m}$  thick, on Si wafers. Photoresist was coated and patterned with  $0.5\mu\text{m}$  lines and spaces. Then, a layer of 120nm of Al was evaporated using a thermal evaporator and the photoresist lifted off to leave the etch mask. The samples were etched in an ICP RIE for two minutes while varying the recipe parameters according to Table 5.1. Then the samples were imaged in the SEM.

Table 5.1. Process parameters for samples etched in first run with sulfur hexafluoride.

Sample #	Gases (sccm)	Coil Power	Platen Power	Pressure	Platen Temperature
1	O2 (10):SF6 (10)	200W	150W	2mT	20°C
2	O2 (10):SF6 (2)	200W	150W	2mT	20°C
3	O2 (10):SF6 (10)	300W	150W	2mT	20°C
4	O2 (10):SF6 (2)	300W	150W	2mT	20°C
5	O2 (10):SF6 (10)	200W	50W	2mT	20°C
6	O2 (10):SF6 (2)	200W	50W	2mT	20°C
7	O2 (10):SF6 (10)	300W	50W	2mT	20°C
8	O2 (10):SF6 (2)	300W	50W	2mT	20°C
9	O2 (10):SF6 (10)	200W	150W	10mT	20°C
10	O2 (10):SF6 (2)	200W	150W	10mT	20°C
11	O2 (10):SF6 (10)	300W	150W	10mT	20°C
12	O2 (10):SF6 (2)	300W	150W	10mT	20°C
13	O2 (10):SF6 (10)	200W	50W	10mT	20°C
14	O2 (10):SF6 (2)	200W	50W	10mT	20°C
15	O2 (10):SF6 (10)	300W	50W	10mT	20°C
16	O2 (10):SF6 (2)	300W	50W	10mT	20°C

In order to illustrate the results efficiently, the images were organized into two figures (one for the cross-section view and one for the tilted view). They are divided into four quadrants. In each quadrant, there are four images corresponding to samples that share two parameters (from the quadrant they are in) and have two other parameters that are varied. Figure 5.4 shows how this is arranged.

Figure 5.5 shows the tilted views of the etched samples. The top two samples in the fourth quadrant produced the best results. The image for the first sample of the first quadrant is actually a view of the sidewall because the sample wasn't loaded properly into the SEM. On the other hand, Figure 5.6 shows the cross-section views of the etched samples. The picture for the first sample of the first quadrant is missing because there wasn't a good edge to look at.

<p>Quadrant 1 corresponds to samples etched with 2sccm's of SF6 and a chamber pressure of 2mT.</p> <table border="1" data-bbox="362 310 782 520"> <tr> <td>Coil Power = 200W Platen Power = 150W</td> <td>Coil Power = 300W Platen Power = 150W</td> </tr> <tr> <td>Coil Power = 200W Platen Power = 50W</td> <td>Coil Power = 300W Platen Power = 50W</td> </tr> </table>	Coil Power = 200W Platen Power = 150W	Coil Power = 300W Platen Power = 150W	Coil Power = 200W Platen Power = 50W	Coil Power = 300W Platen Power = 50W	<p>Quadrant 2 corresponds to samples etched with 2sccm's of SF6 and a chamber pressure of 10mT.</p> <table border="1" data-bbox="919 310 1339 520"> <tr> <td>Coil Power = 200W Platen Power = 150W</td> <td>Coil Power = 300W Platen Power = 150W</td> </tr> <tr> <td>Coil Power = 200W Platen Power = 50W</td> <td>Coil Power = 300W Platen Power = 50W</td> </tr> </table>	Coil Power = 200W Platen Power = 150W	Coil Power = 300W Platen Power = 150W	Coil Power = 200W Platen Power = 50W	Coil Power = 300W Platen Power = 50W
Coil Power = 200W Platen Power = 150W	Coil Power = 300W Platen Power = 150W								
Coil Power = 200W Platen Power = 50W	Coil Power = 300W Platen Power = 50W								
Coil Power = 200W Platen Power = 150W	Coil Power = 300W Platen Power = 150W								
Coil Power = 200W Platen Power = 50W	Coil Power = 300W Platen Power = 50W								
<p>Quadrant 3 corresponds to samples etched with 10sccm's of SF6 and a chamber pressure of 2mT.</p> <table border="1" data-bbox="362 716 782 926"> <tr> <td>Coil Power = 200W Platen Power = 150W</td> <td>Coil Power = 300W Platen Power = 150W</td> </tr> <tr> <td>Coil Power = 200W Platen Power = 50W</td> <td>Coil Power = 300W Platen Power = 50W</td> </tr> </table>	Coil Power = 200W Platen Power = 150W	Coil Power = 300W Platen Power = 150W	Coil Power = 200W Platen Power = 50W	Coil Power = 300W Platen Power = 50W	<p>Quadrant 4 corresponds to samples etched with 10sccm's of SF6 and a chamber pressure of 10mT.</p> <table border="1" data-bbox="919 716 1339 926"> <tr> <td>Coil Power = 200W Platen Power = 150W</td> <td>Coil Power = 300W Platen Power = 150W</td> </tr> <tr> <td>Coil Power = 200W Platen Power = 50W</td> <td>Coil Power = 300W Platen Power = 50W</td> </tr> </table>	Coil Power = 200W Platen Power = 150W	Coil Power = 300W Platen Power = 150W	Coil Power = 200W Platen Power = 50W	Coil Power = 300W Platen Power = 50W
Coil Power = 200W Platen Power = 150W	Coil Power = 300W Platen Power = 150W								
Coil Power = 200W Platen Power = 50W	Coil Power = 300W Platen Power = 50W								
Coil Power = 200W Platen Power = 150W	Coil Power = 300W Platen Power = 150W								
Coil Power = 200W Platen Power = 50W	Coil Power = 300W Platen Power = 50W								

Figure 5.4. Explanation for the image layout used in Figures 5.5 and 5.6. The layout is divided into four quadrants and four images are in each quadrant. The recipe parameters are depicted in this figure.

By inspecting the images some conclusions can be drawn. A high enough sulfur hexafluoride flow is necessary to generate enough sidewall passivation (redeposition) to prevent undercutting.

A higher chamber pressure increases the sidewall passivation rate, but it also increases the lateral etch rate. If the sidewall passivation rate is greater or equal to the lateral etch rate, then undercutting is minimized or, in the ideal case, eliminated. From the images it can be seen that the undercutting was lower when the chamber pressure was at its high state as long as the sulfur hexafluoride flow was also at its high state.

At low platen power, there is bowing in the sidewalls, while at high platen power the bowing is reduced and practically disappears. This is probably due to charging in the

polymer film which deflects the ions that start out in a trajectory perpendicular to the substrate [26], [27]. At higher platen powers the deflection is less because the ions are moving at a greater velocity.

These results are promising. However, when this etch was translated to the full NOA 71-PI\_2525-NOA 71 stack, the etch rate slowed down considerably when it hit the PI-2525 layer, while the undercut increased destroying the features (see Figure 5.7). This pointed to the PI-2525 undercutting faster than the NOA 71. If this was the case, then the etch should be developed for the PI-2525 first. When we etched a sample with only PI-2525 on it, we found that with the same recipe as for the full stack, the features didn't undercut appreciably as in Figure 5.8. Thus, we concluded that the passivation rate is lower at deeper levels in the etch. To increase the redeposition the logical step is to add more sulfur hexafluoride. Reducing the oxygen content should also help reduce the lateral etch rate. This is what we did in the extreme case of using only sulfur hexafluoride to increase the passivation and not including oxygen at all (see Figure 5.9).

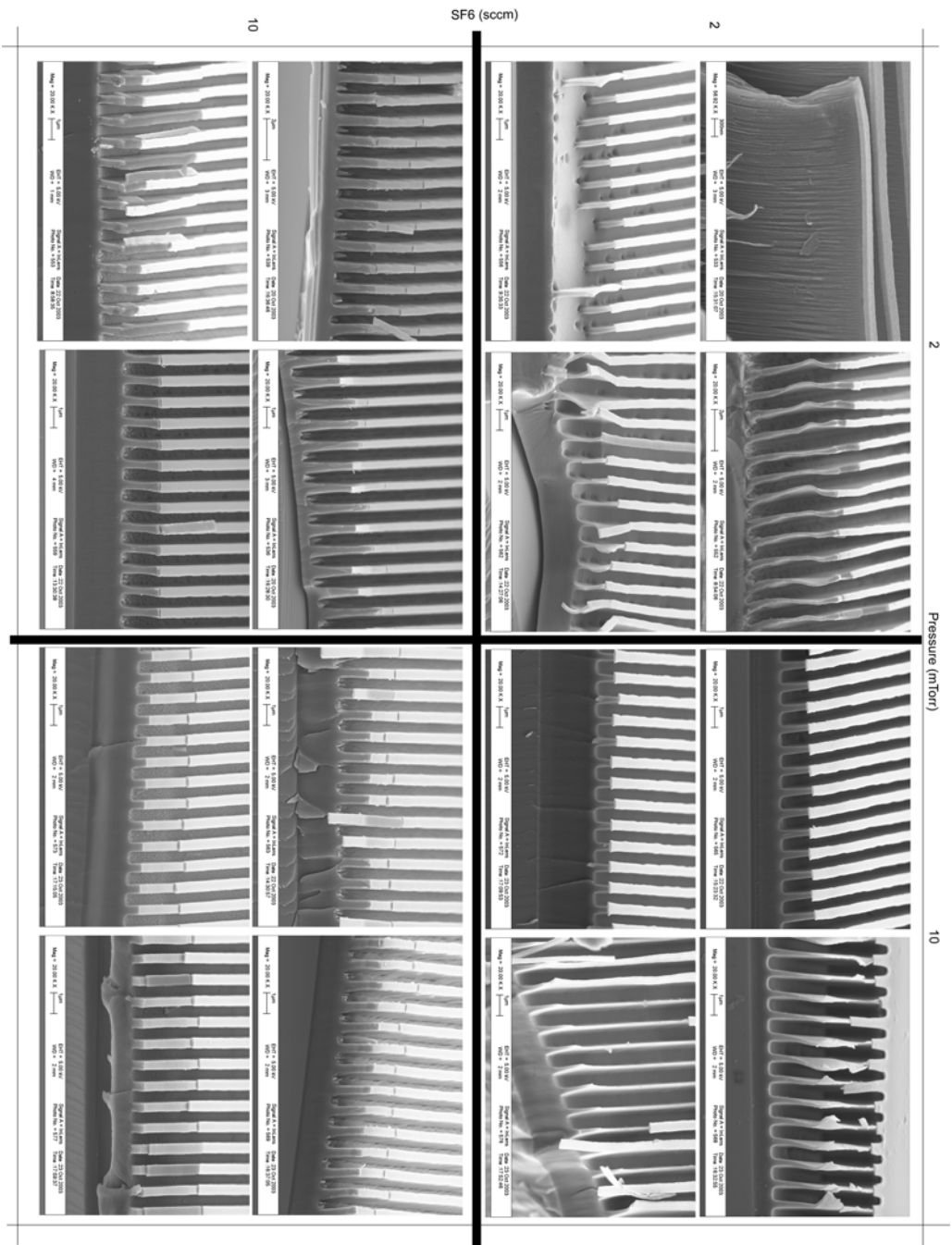


Figure 5.5. Tilted images for the 16 samples that were etched in this experiment.

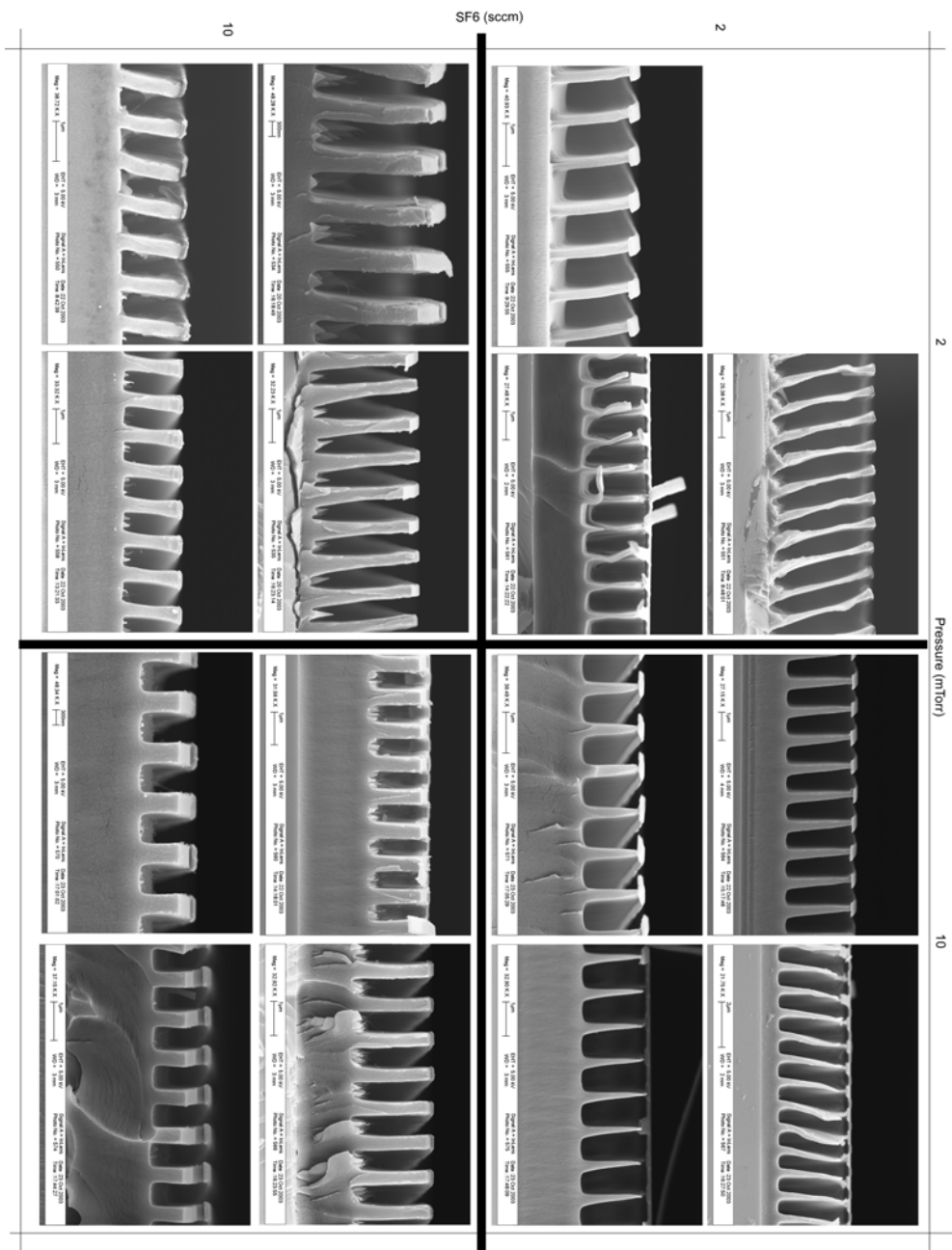


Figure 5.6. Cross-section images for the 16 samples that were etched in this experiment.

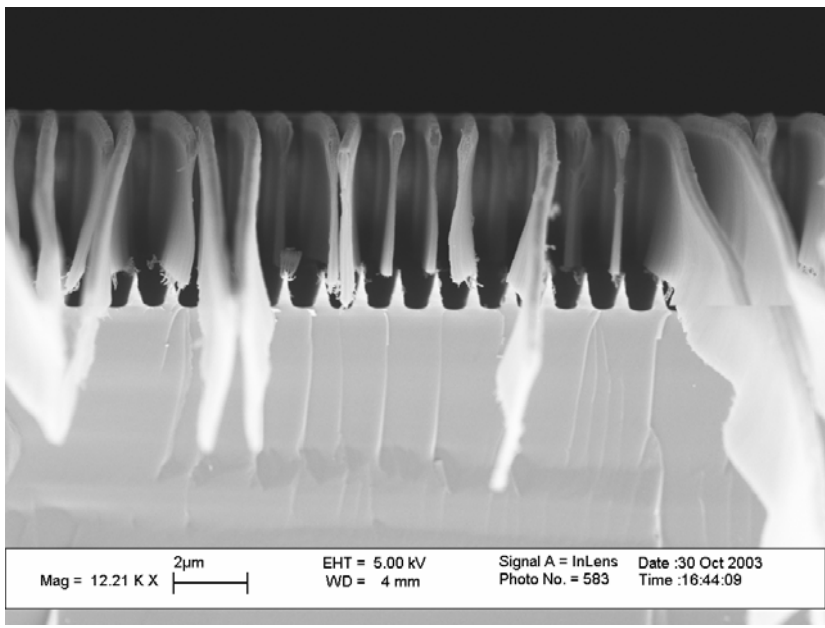


Figure 5.7. Half micron features etched in a stack of NOA 71, PI-2525, and NOA 71. The etch went through the first NOA 71 layer and half way through the PI-2525 layer. It can be seen that the PI-2525 is severely undercut at the interface with the NOA 71.

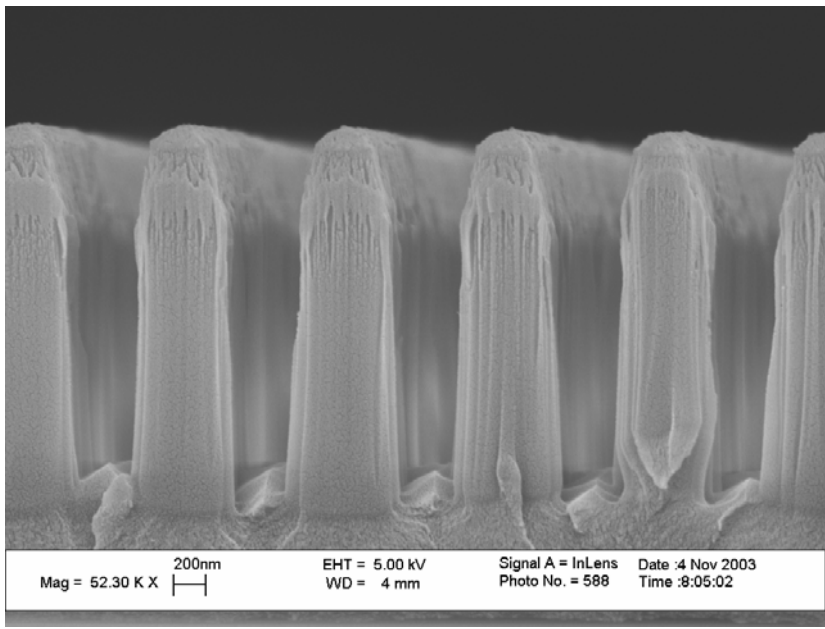


Figure 5.8. Half micron features etched in PI-2525 with the same etch recipe used to etch the sample shown in figure 1. Some effects of mask erosion can be observed in the roundedness of the top of the features. However, no undercutting is evident.

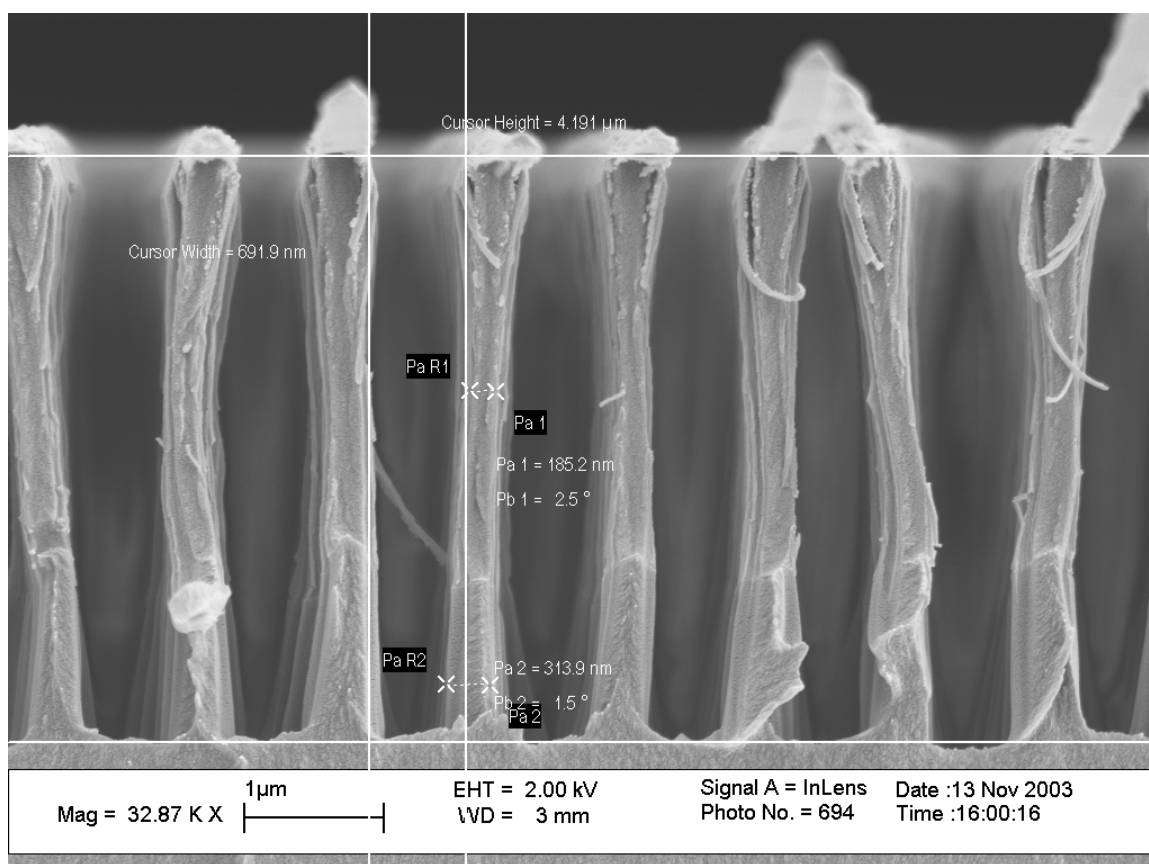


Figure 5.9. Half micron features etched in NOA 71 and PI-2525 with 30sccm of sulfur hexafluoride. The undercutting has been reduced with respect to the etch in Figure 5.7.

This was the best etch that we achieved. It is still two to three microns shy of the required etch depth. More work is needed to try to improve it. Even though it isn't very likely that using sulfur as a passivating species will be the answer, using a lower platen temperature may improve the results.

### 5.3 Conclusion

In the past two chapters we have discussed the integrated optic depolarizer. While in the previous chapter we went into detail about the design and analysis of the device, in this chapter we addressed the main challenge in its fabrication. This main challenge is to

develop an etch process with a very high aspect ratio, and straight, vertical, and smooth sidewalls. We used an etch chemistry based on low chamber pressure and high bias power, and another one based on a passivating species to protect the sidewalls from undercutting. The process using high bias and a low chamber pressure with oxygen, helium, and tetrafluoromethane worked well for two micron features. However, it couldn't be scaled down to features of half micron. The second process based on a passivating species with oxygen and sulfur hexafluoride worked better for half micron features, but we couldn't reach the desired etch depth.

There is a good opportunity for future research in the development of this etch process. Several paths can be explored. For instance, the process based on sulfur passivation described here can be explored at lower platen temperatures. On the other hand, other etch chemistries may be able to provide greater passivation for these materials. Thus, the use of other combinations of gases such as carbon monoxide could be explored.

## **CHAPTER 6**

### **MICROMOLDED WAVEGUIDES**

In this chapter, the fabrication of waveguides using micromolding is explored. The molding approach that we followed was based on a sacrificial mold which is fabricated on top of the waveguide's undercladding and is removed after the waveguide's core has been defined. Several materials were used for the mold, but in the end none of them yielded a successful process. This chapter is included to document what was done.

#### **6.1 Introduction**

Waveguides have three main layers, which are the undercladding, the core, and the overcladding. In many cases both claddings are made of the same material, but not always. Additionally, many different materials and waveguide profiles can be used. We focused on making channel waveguides (see Figure 6.1), which have an undercladding, fully etched core, and overcladding. In our case, the materials are polymers and both claddings are made of the same material. The core's geometry is square to try to minimize polarization dispersion, which occurs when the two polarization components propagate at different velocities inside the waveguide.

Channel waveguides are typically fabricated by first coating the undercladding on a substrate. Then the core layer is coated as a film and a masking material is deposited and patterned using photoresist. This patterning step defines the waveguide. Then, the core material is etched either with chemicals, called a “wet” etch, or with a plasma, which is called “dry” etching. Since “wet” etching is isotropic in most cases, “dry” etching is used when the walls of the etched core must be vertical. However, plasma etching often causes sidewall roughness on the waveguide. This roughness produces undesirable scattering losses [52], [53].

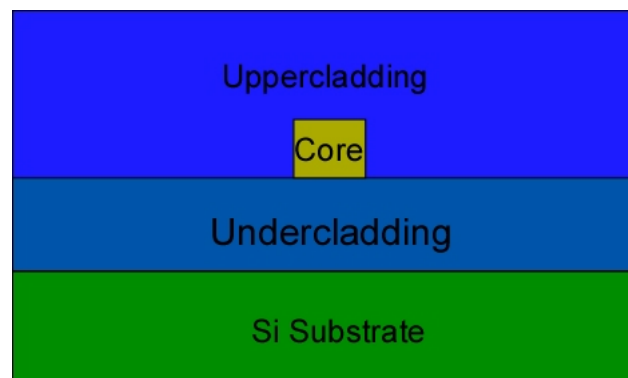


Figure 6.1. Cross-section for a typical channel waveguide with an uppercladding and an undercladding. For the waveguides discussed here, the undercladding and the uppercladding are made of the same material.

Our proposal was that by filling a mold with the waveguide’s core polymer material and removing the excess, the sidewall roughness could be significantly reduced. We originally tried to make the mold in silicon using a two wafer approach. This method consisted in making the mold in silicon and filling it with the core material. Then, the undercladding was coated. This was followed by bonding the mold wafer to a handle wafer and a subsequent release of the mold wafer. However, this didn’t work out very

well because we couldn't release the waveguide from the mold without catastrophic delamination. Thus we shifted our focus to a photodefined mold made on top of the undercladding layer which would then be removed to coat the overcladding on the defined core layer. In this chapter we discuss the mold's requirements and the fabrication approaches that we worked on.

## **6.2 Mold Requirements**

Waveguide fabrication must follow specific designs to maintain the desired properties of the guides. In this case we designed a channel waveguide of specific dimensions whose core is typically square. The mold must take this form as accurately as possible. Of particular interest are the sidewall roughness and vertical walls. Sidewall roughness causes scattering losses. Hence, the mold's sidewalls should be as smooth as possible. On the other hand, polarization dispersion will be augmented if the waveguide's shape isn't symmetric. Thus, vertical sidewalls are of great importance, too.

Since we weren't able to pursue the silicon mold approach any further, we decided to focus our efforts on a simpler method, a photodefined mold approach. It consists on spin coating a cladding layer on the silicon substrate; then forming the mold on top of it and spin coating the core layer followed by a chemical mechanical planarization (CMP) step to remove the excess core polymer and leave it only in the grooves to make a channel waveguide. Then, the mold is removed. Finally, another clad layer is spun (Figure 6.2). This new approach brings up a very important challenge: finding a mold material that is chemically compatible with the core and cladding

polymers, thermally stable at the core polymer's curing temperatures, and easily removable by means of wet chemical etching.

### 6.2.1 Chemical Compatibility

During the fabrication process, the polymers that will make the waveguide and the necessary materials to create the mold will interact. All of these materials must be compatible with each other, as well as the chemicals they may require for processing. These interactions are mainly spin coating, developing, etching, and adhesion.

Most materials that are applied by spin coating come in a solution. Their solvents are generally chosen to achieve the best results in terms of film uniformity and adhesion. These solvents can interact with underlying layers. In some cases, even after a full cure cycle, materials aren't fully impervious to solvents. This is precisely the case with the family of perfluorocyclobutyl (PFCB) polymers developed and supplied by Clemson University. The cladding polymer (6F:TVE (80:20)) was cured at 300°C and some solvents could still damage it. In some cases the damage was small enough during the brief interaction while spinning, that it was acceptable. With other solvents, however, a thin protective layer had to be deposited before the spin coating step.

Photolithography is an unavoidable step in any processing involving integrated devices. It allows you to transfer a pattern from a mask onto a light sensitive material. Developing is a necessary step to remove the unwanted material when making the pattern. The developer will also come into contact with the PFCB polymers. Thus, unwanted interaction between the polymers and the developer is possible. Fortunately, most fluorinated polymers, the family of PFCB polymers from Clemson University included,

are impervious to most commonly used chemicals for developing. Thus, the PFCB polymers are chemically compatible with the developing steps during fabrication. Once the mold has been fabricated and it has fulfilled its purpose of shaping the waveguide's core, it must be removed to apply the cladding overlay. The mold is removed by etching. In this case the preferred method is "wet" etching versus the alternative of "dry" etching, which would require critical alignment which, in turn, is extremely difficult due to the small dimensions of the waveguides. During wet etching the sample is immersed in a solution that will consume the mold material in order to leave only the core and cladding polymers on the substrate. The solution should not react at all with them to preserve their composition and surface quality. The PFCB polymers have very little interaction with bases and none with acids. However, they do interact considerably with some solvents. Hence, not all materials that require solvent etchants will be compatible with the process.

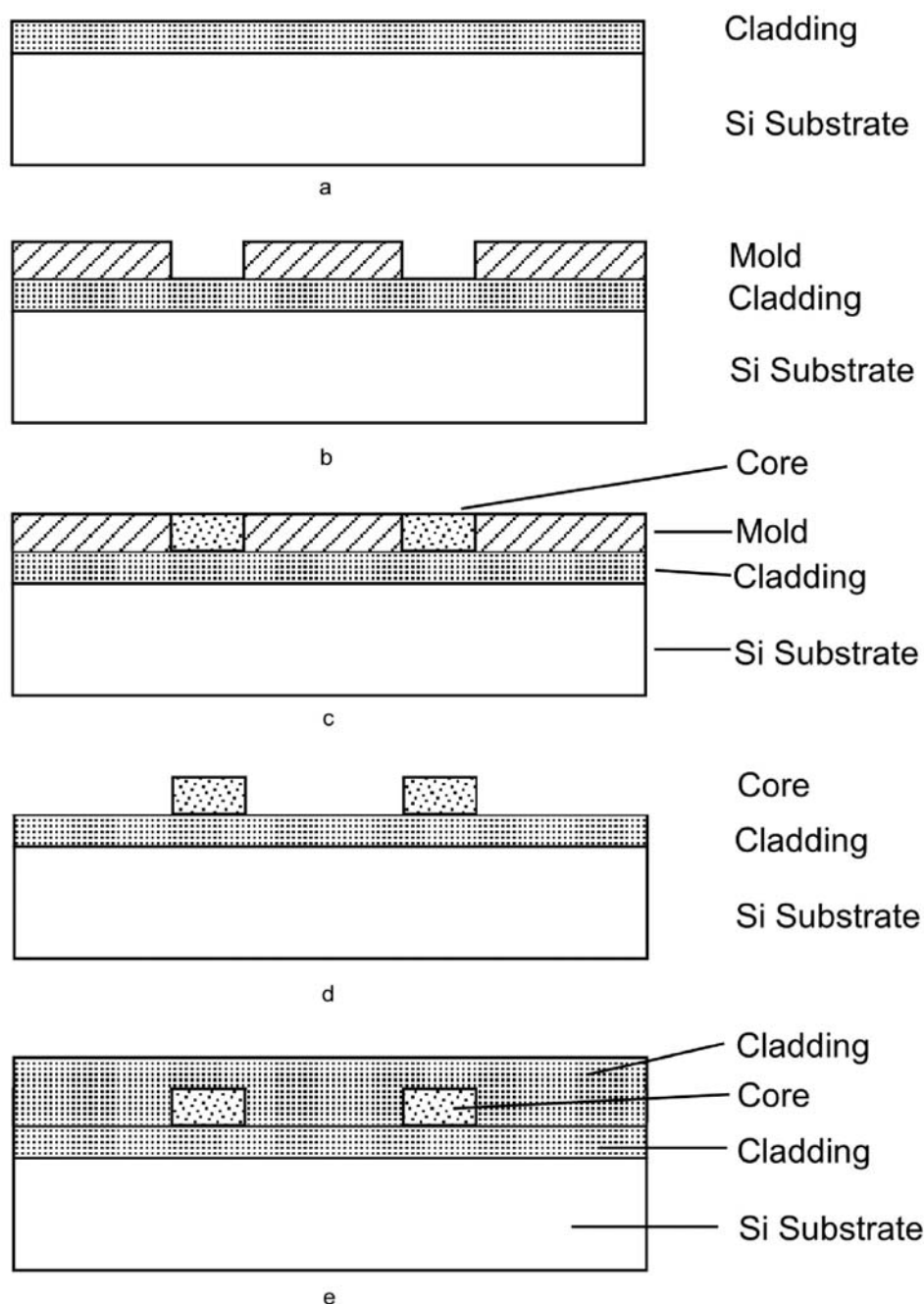


Figure 6.2. Photodefined Mold: (a)-(e) illustrate the basic steps for making micromolded waveguides: (a) cladding is spun and cured on silicon substrate. (b) Mold is made on cladding. (c) Core fills mold and excess is removed with CMP so that the core material is left only inside the grooves defining the waveguides. (d) Mold is removed. (e) Cladding is spun and cured over core.

Finally, adhesion is an important parameter because the mold will undergo several processes while it remains on the polymer. It must at least be good enough so that the

mold doesn't delaminate from the polymer surface before we want to remove it. If the adhesion is not adequate, we can use adhesion promoters to try to improve it. So far it hasn't been a major concern, but it is important to keep it mind when selecting the appropriate mold material.

We have discussed the main chemical compatibility issues that will arise when trying to fabricate a mold on the cladding material. The most critical interactions happen during spin coating and the mold's etching. A suitable mold material will be compatible with the PFCB polymers during all steps of the process.

### 6.2.2 Thermal Stability

The PFCB polymers must be cured at temperatures above 150°C for at least two hours. This means that the mold will be exposed to such temperatures for long periods of time. Its shape must remain constant throughout this entire process for the waveguide to retain its properties. Hence, a successful fabrication process depends on the mold's stability throughout the curing of the core polymer.

During curing, the core polymer can flow until polymerization starts to occur solidifying it. If the mold changes its shape, then the core will take that shape and the fabricated waveguide won't meet the desired geometrical specifications, which will definitely alter its polarization properties because the sidewalls won't remain straight. Their shape will most likely be rather complicated. Therefore, besides disrupting the polarization properties, the irregularity of the sidewalls (due to the mold changing shape during the core's curing process) may also induce some radiation losses and the waveguide won't guide light adequately. A good example of a material that could be used to make the mold if thermal stability wasn't so important is regular photoresist. At first

glance, it seems like a good option to make the mold. However, most photoresists start to flow at temperatures above 130°C. This means that they won't hold their shape during the polymer curing.

In summary, the mold must be made of a material that will remain stable when undergoing the core polymer's curing. Thus the mold's material must have a glass transition temperature similar to PFCB.

### 6.2.3 Mold Removal

Once the waveguide's core has been formed, it is time to remove the mold in order to complete the fabrication. The mold must be removed by using a chemical that will attack it and etch it away. As discussed above, this chemical shouldn't interact with the waveguide materials. Additionally, since the contact area of the mold with the clad layer is much larger than that of the core polymer, the core is susceptible to delamination. Thus, the key concerns when removing the mold are damaging the polymer films and core delamination during mold removal.

The polymer films can be damaged by causing delamination from the substrate or by chemical interaction, which degrades the films' quality. When strong bases, which will remove resists in some cases, are used to remove the mold, they will attack the silicon substrate. If given enough time, the clad polymer will start to delaminate from the substrate because the silicon will be eroded from underneath it causing a loss of mechanical support. On the other hand, film quality can be degraded when solvents that attack the polymers are used to remove the mold. They will degrade the film quality by dissolving the polymer and creating pits or swelling on its surface. Once again, if the

exposure is short enough, the damage might be tolerable. Ideally, though, the chemical used to remove the mold won't attack the films nor the substrate. In some cases, the substrate could be protected if that represented the only hurdle to clear before having a successful fabrication process.

If we have delamination of the core from the clad polymer while removing the mold, the waveguide is effectively ruined. This is a particular problem if ultrasound is required to remove the mold, especially if the core polymer didn't bond well with the cladding during curing. Ultrasound is often used to remove photoresist. Its vibration can easily cause delamination of the core polymer because the mold has a much larger contact area. It is greatly desirable that ultrasound isn't needed to reduce the chances of delamination. Furthermore, even when ultrasound can be avoided, poor bonding between the core and cladding polymers will cause delamination. A possible solution to this is to cure the cladding at a lower temperature than what the core will be cured at. In this way, both may undergo some curing together and promote better adhesion.

We have discussed the importance of removing the mold and the potential problems while doing so. Finding a mold material that allows for easy removal is of great importance when attempting to fabricate a waveguide using micromolding. The requirements that our mold must meet are chemical compatibility, thermal stability, and it must be easily removable. We have described these requirements in detail and mentioned examples of how some materials stack up in relation to these requirements. Our research has focused on finding a material and a set of steps that would yield a successful waveguide fabrication. These processes will be detailed in the following section as well as the problems that we encountered.

## 6.3 Fabrication Approaches

In the previous section we discussed the knowledge we gained through working on different mold materials and processes. We tried to fabricate the micromolded polymer waveguides following three different processes. All three involve different mold materials. In the next sections we will describe three different processes that rewarded us with a better understanding of what our mold should be like in order for the fabrication to yield a successful result.

### 6.3.1 SU8 as the Mold Material

This fabrication approach consists on starting with a silicon substrate and spinning the clad polymer, which is called 6F:TVE (80:20), and curing it at 300°C for 2hours (Figure 6.3 (a)). The material used for the mold is SU8, a negative tone radiation sensitive polymer. The solvent used in it, cyclopentanone, dissolves the clad polymer. Thus, a thin layer of silicon dioxide was sputtered on the cladding (Figure 6.3 (b)). Afterwards, the SU8 was spun and patterned (Figure 6.3 (c)). The SiO<sub>2</sub> layer had to be removed inside the patterned channels to allow the core polymer to be in direct contact with the cladding. This was done with reactive ion etching using sulfur hexafluoride and oxygen (Figure 6.3 (d)). After the etching, the core polymer, BPVE:TVE (80:20), was spun and cured at 195°C for 2hrs. in a tube furnace with a nitrogen atmosphere to prevent oxidation (Figure 6.3 (e)). Since our design calls for a channel waveguide with a square cross-section, the core was polished down to the silicon dioxide level using chemical mechanical planarization (CMP) leaving the core polymer only inside the patterned channels (Figure 6.3 (f) and Figure 6.4). Now the mold material had to be removed. We

tried dipping the sample in buffered hydrofluoric acid (BHF) for hours, but the mold didn't come off. As a matter of fact we later learned that SU8 could only be removed by using very extreme methods (extreme temperatures, salts bath, fuming nitric acid), all of which not only damage the polymers, but actually destroy them. The manufacturer offered us a product they were testing for SU8 removal. It consisted of a material that was spun into a thin layer prior to spinning the SU8 and later its removal would cause the SU8's removal. However, even this technique failed. SU8 proved to be great in some aspects such as chemical compatibility (once the silicon dioxide layer was included) and thermal stability, but came up short because it isn't removable. If the removal had been successful, the process would have continued with the spinning and curing of the cladding to finalize the process and have the micromolded waveguides (Figure 6.3 (g-h)).

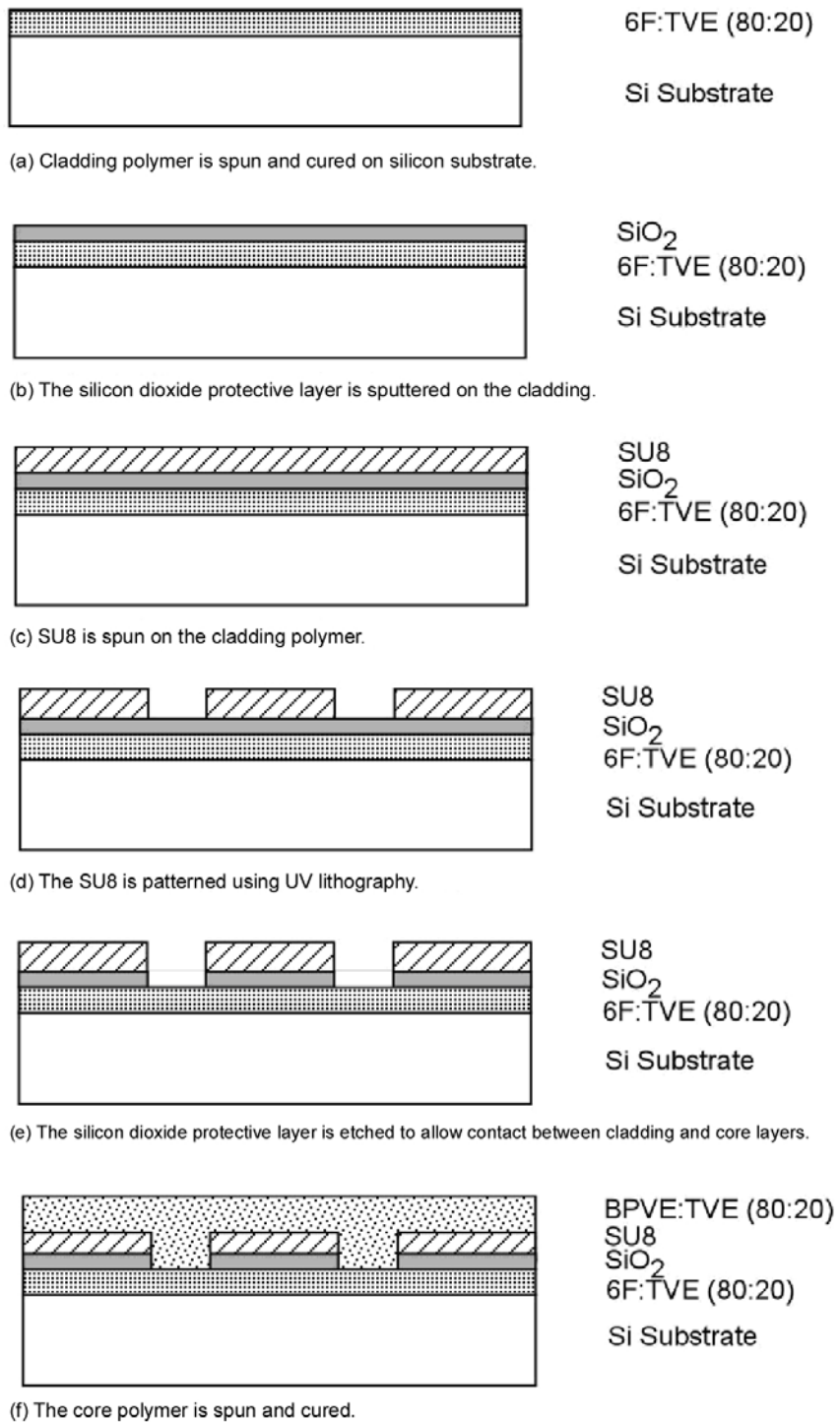


Figure 6.3. (a)-(f). SU8 micromold process.

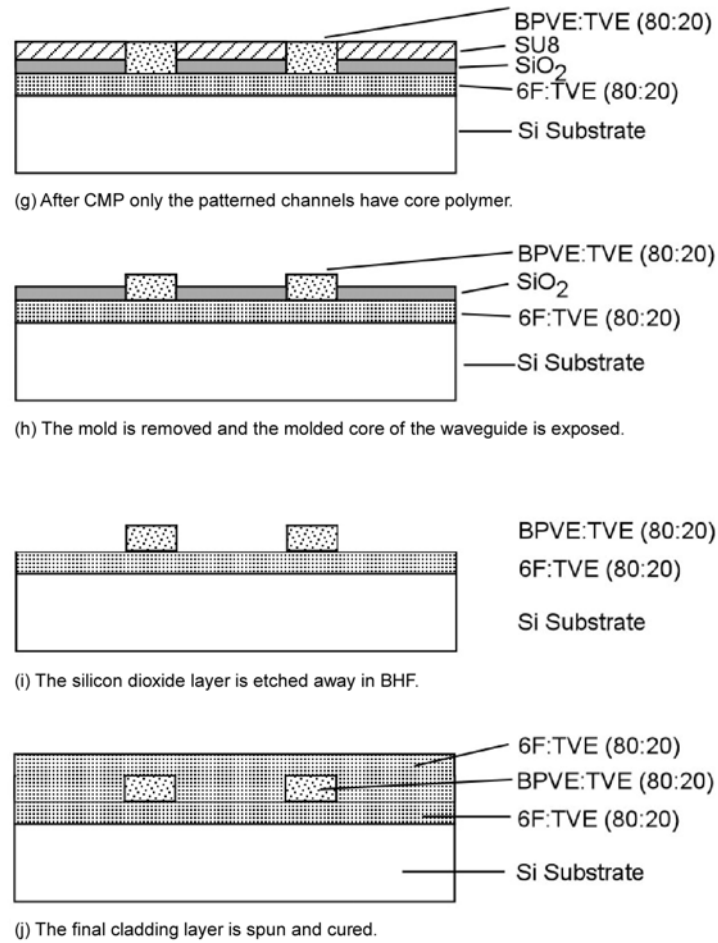


Figure 6.3. (g)-(j). SU8 micromold process.

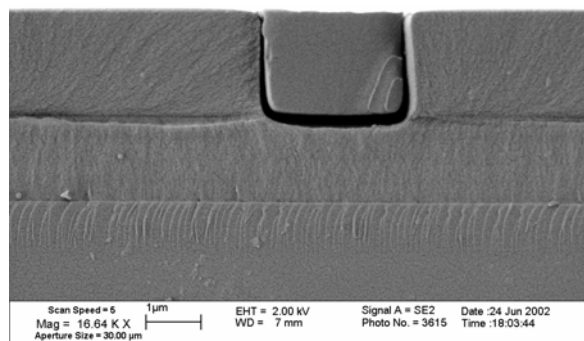


Figure 6.4. SEM image of the core polymer and the SU8 mold on the cladding after CMP. It was impossible to remove the mold with this approach.

### 6.3.2 High Temperature Resist as the Mold Material

Our next attempt was to use a photoresist as the mold material. Photoresists are usually easy to remove. Because regular photoresists are not thermally stable above 130°C and our curing requirements are of at least 150°C, we turned to high temperature resists, which are engineered for ion implantation. They can withstand processing temperatures of around 200°C.

The process is similar to the one used with SU8. The cladding polymer is spun and cured for 2hrs. at 300°C on the silicon substrate (Figure 6.5 (a)). Since this photoresist does minimal damage to the clad polymer during spinning, no protective layer was needed. After spinning and patterning the photoresist, the core polymer was spun and cured at 190°C for 2hrs (Figures 6.5 (b)-(c)). Then the excess core was polished with CMP (Figure 6.5 (d) and Figure 6.6). We tried to remove the photoresist with a 20% potassium hydroxide solution and by using a solvent called NMP (n-Methyl Pyrrolidone) at room temperature, but the former caused the cladding to delaminate from the substrate by attacking the silicon, and the latter seemed to have no effect. When the temperature was brought up to 80°C the NMP did remove the photoresist; however, it didn't etch it. The resist was removed in large chunks, which caused the delamination of the core from the cladding. If the removal had been successful, the process would have been completed by spinning and curing the second cladding layer (Figures 6.5 (e)-(f)). This approach also failed because we couldn't remove the mold without damaging the existing films (in this case the core).

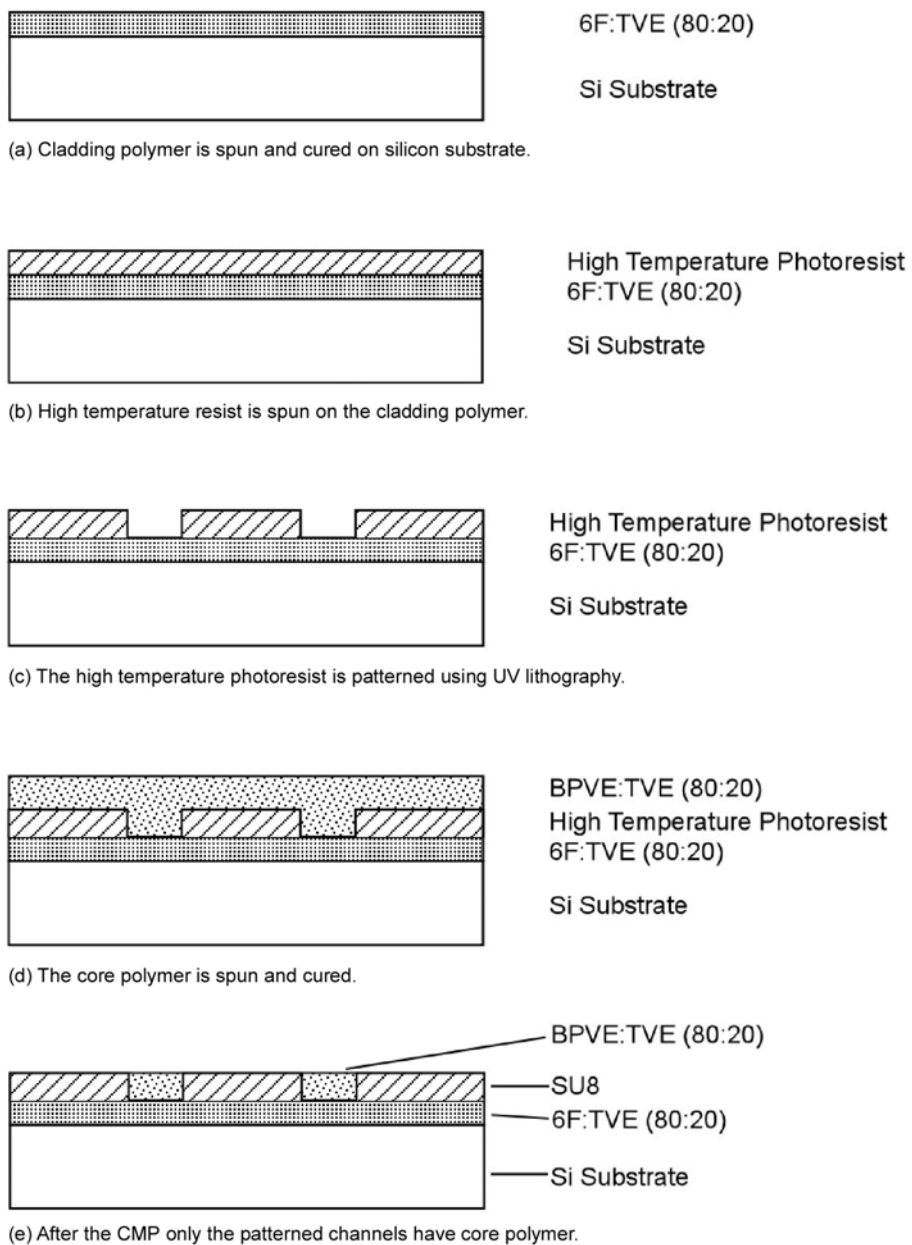
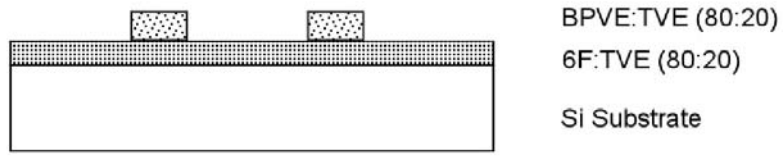
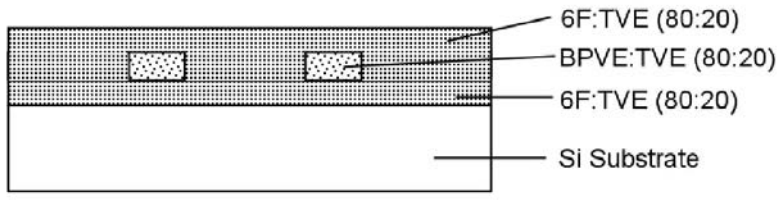


Figure 6.5. (a)-(e). High temperature photoresist micromold process.



(f) The mold is removed.



(g) The final cladding is spun and cured.

Figure 6.5. (f), (g). High temperature photoresist micromold process.

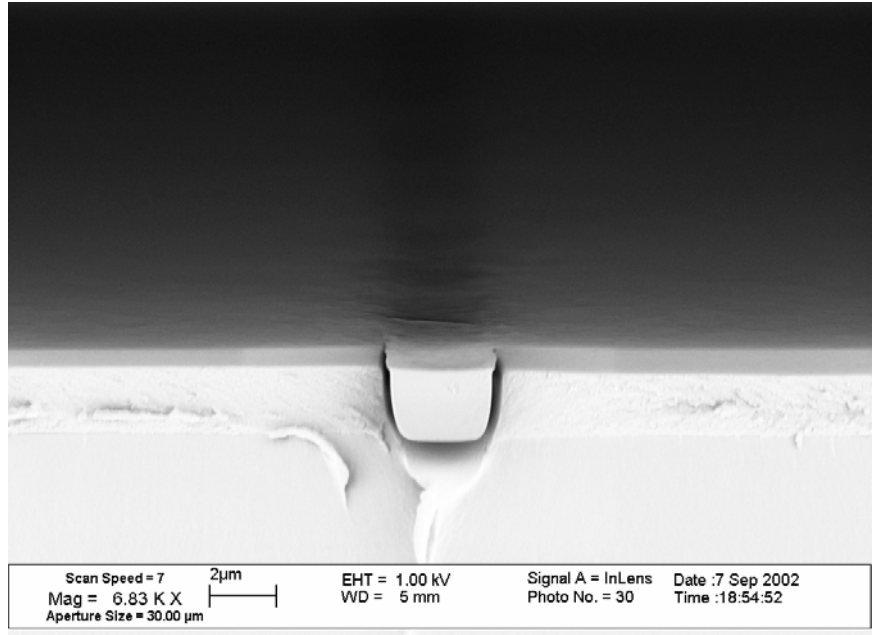


Figure 6.6. SEM image of core polymer in the high temperature resist mold on the cladding. In the following step, when removing the mold, the core became delaminated from the cladding.

### 6.3.3 Silicon Dioxide as a Mold Material

Finally, we will describe an approach that uses photoresist to pattern a negative version of the mold. Using the photoresist, a silicon dioxide mold is made around it.

Silicon dioxide is an attractive material because it is thermally stable and can be etched away with BHF.

Once again we started by spinning the clad polymer on the silicon substrate and curing it at 300°C for 2hrs (Figure 6.7 (a)). Then the high temperature photoresist is spun and patterned, but this time the pattern is inverted (We use a mask of opposite polarity to create a negative version of what was done in the previous approaches) (Figure 6.7 (b)). Afterwards, a thick silicon dioxide layer is sputtered on top of the pattern. Due to the pattern itself, the sputtered layer won't be flat, but will have big lumps in the areas where the resist is present (Figure 6.7 (c)).

This step produced some undesirable results. During sputtering, the sample gets hot due to the collisions of the silicon dioxide molecules with it; and, because the cladding polymer has a coefficient of thermal expansion much higher than silicon dioxide, the cool down stresses the film greatly causing it to break and delaminate in the unpatterned areas. This yielded unpredictable results in the CMP step, usually resulting in the removal of everything on the substrate.

If this could be fixed, we would polish the silicon dioxide back to the resist level, leaving an extremely flat surface (Figure 6.7 (d)). Then with plasma oxygen etching, the resist would be removed (see Figure 6.8 for an example of the mold on a silicon substrate) and the core spun and cured at a temperature close to its minimum curing temperature (to stress the oxide mold as little as possible) (Figures 6.7 (e),(f)). After a second CMP step, and mold removal using BHF, the cladding would be spun and cured to finish the process (Figures 6.7 (g)-(i)).

The problems encountered in this approach are rooted in the huge coefficient of thermal expansion (CTE) mismatch between silicon dioxide and the waveguide polymers. This makes it difficult to think that this method can work with silicon dioxide. However, there may be other materials with a CTE closer to the PFCB polymers that could make it feasible.

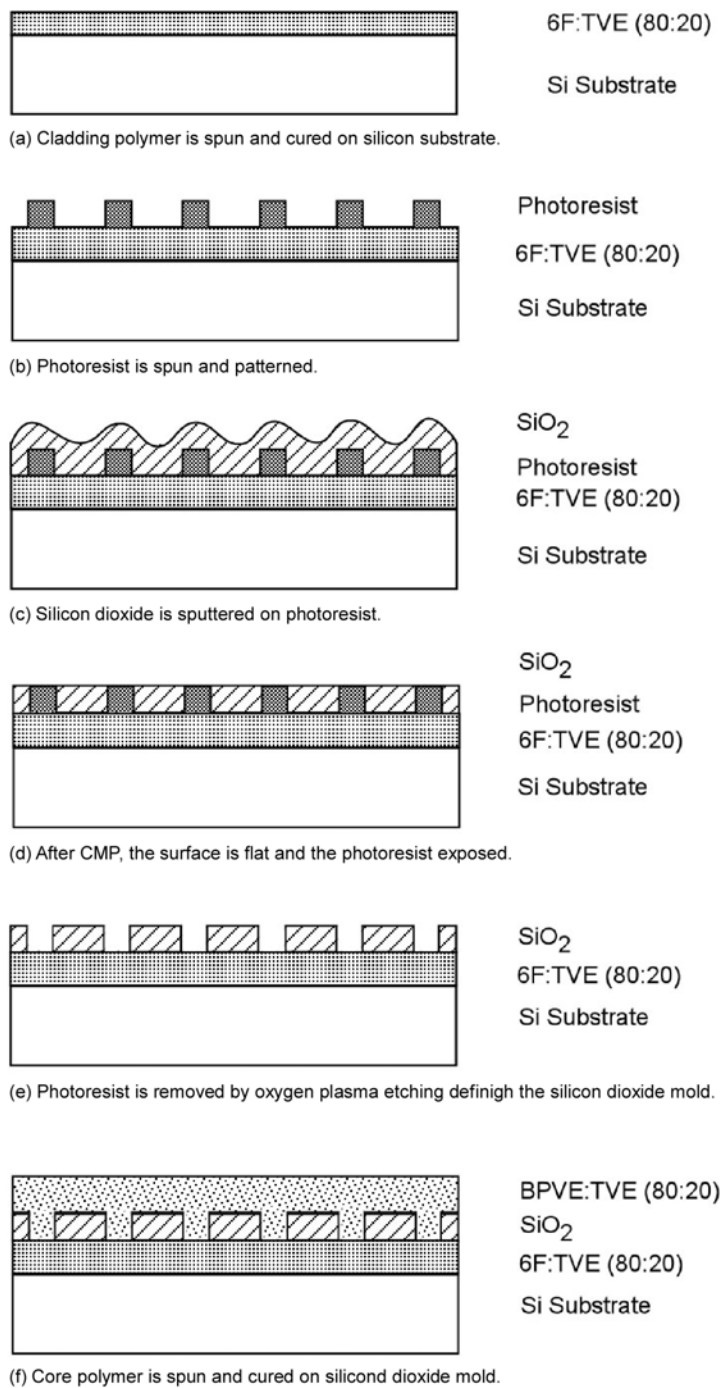
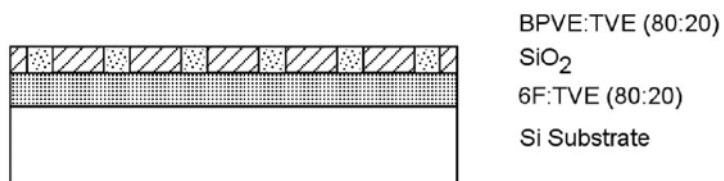
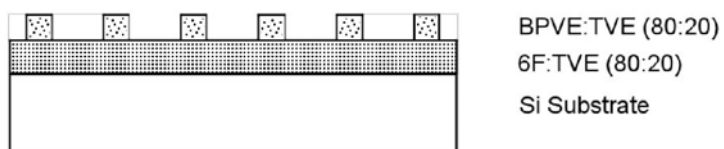


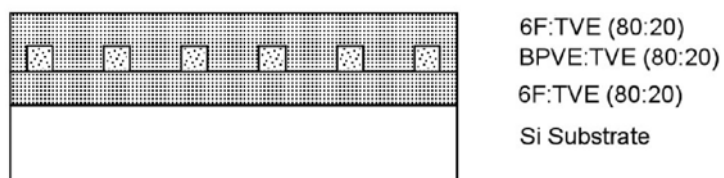
Figure 6.7. (a)-(f). Silicon dioxide micromold process.



(g) After a second CMP, the excess core polymer is removed.



(h) The silicon dioxide is removed with BHF.



(i) The final cladding layer is spun and cured.

Figure 6.7. (g)-(i). Silicon dioxide micromold process.

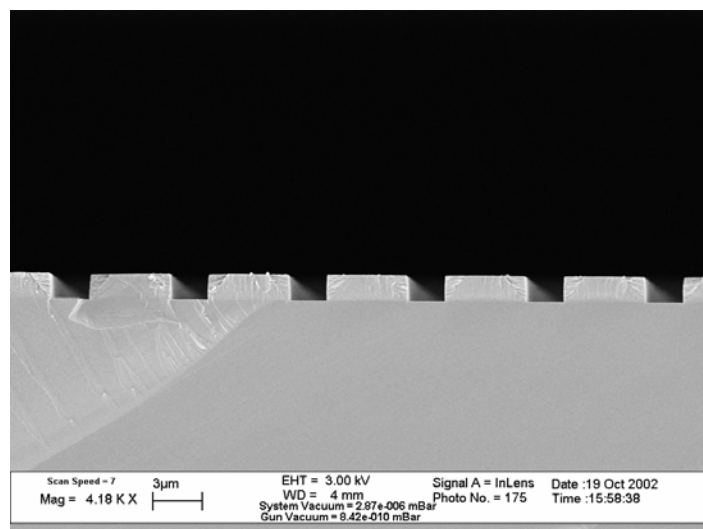


Figure 6.8. SEM image of the silicon dioxide mold successfully made on a silicon substrate.

## 6.4 Conclusion

In this chapter, we described the requirements that a mold must have to make successful micromolded waveguides. Additionally, we discussed three different approaches we worked on to produce micromolded polymer waveguides. The first two produced a wealth of knowledge on the requirements that a suitable mold must have for the fabrication to be successful. While these methods weren't successful, different materials could be all that is needed to make them work. Future research should be aimed at finding better photodefinable materials which are easier to remove while being strong enough to withstand the required processing temperatures.

## **CHAPTER 7**

### **FABRICATION OF DEEP TRENCHES IN PFCB POLYMERS**

In this chapter, Sections 7.1 and 7.2 were published in the SPIE Proceedings for the Photonics West 2005 conference © SPIE. In them the development of a vertical, deep polymer etch is presented. The following sections discuss further efforts to reduce the sidewall roughness and introduce design of experiments as a tool used for this purpose.

#### **7.1 Introduction**

The minimum size of planar lightwave circuits (PLCs) in low refractive index contrast waveguides is ultimately limited by the area needed to make bends. Since their refractive index contrast is typically in the range of 0.3 to 1.5%, simply making an arc on the waveguide requires a minimum radius on the order of at least several millimeters to achieve high transmission through the bend. A structure that can be used to significantly reduce this area is a single air interface bend (SAIB) [34]. A SAIB consists of vertically etching a region at the corner of a waveguide bend. This creates a high refractive index contrast interface and the incident radiation is reflected into the bent waveguide through total internal reflection (see Figure 7.1). [34] The etched area that defines the SAIB must encompass most of the incident mode in order to obtain high bend efficiency. In the case

of low refractive index contrast waveguides, the mode profile has a typical cross-sectional dimension on the order of 10 to 20  $\mu\text{m}$ . Thus, the etched region must be just as deep. The bend efficiency achievable with a SAIB doesn't depend only on etching deep enough to affect the entire mode profile. The characteristics of the interface such as verticality, profile, and roughness will determine what fraction of the incident mode is reflected into the bent waveguide and how much radiation is scattered or misdirected. Thus, we must develop an etch that yields a highly anisotropic, vertical, and smooth etch.

Other groups have worked on various etch processes for polymer materials. For example, Pons, et al. [22] used  $\text{SO}_2$  as a passivating species and concentrated on etching submicron features. Chinoy [54] employed a design of experiments (DOE) to study the etching of benzocyclobutene using photoresist as an etch mask. Schuppert, et al. [21] reported etching PFCB polymers using cryo cooled ( $T=-50^\circ\text{C}$ ) reactive ion etching and a photoresist etch mask for waveguide fabrication. They achieved an approximately  $84^\circ$  sidewall angle for a  $\sim 5.5 \mu\text{m}$  deep etch.

Our work is focused on etch chemistries using oxygen/helium and carbon dioxide/helium in an inductively coupled plasma reactive ion etcher (ICP-RIE) to etch deep trenches in PFCB polymers with silicon dioxide as an etch mask. We report a highly anisotropic and vertical etch with which we made and tested SAIBs and discuss possible improvements.

## 7.2 Etch Development

Our initial work was carried out in a reactive ion etcher (RIE). We started our recipe development using helium and oxygen gas mixtures. The parameters that we varied were helium to oxygen gas ratios and power. We quickly settled on 175W power and a ratio of 12:8 sccm of oxygen to helium. Figure 7.2 shows an SEM image of such an etch for 2 $\mu$ m features with an etch depth slightly over 2 $\mu$ m. The etched sidewalls are very close to 90°. While it is impossible to determine the exact sidewall angle accurately from this image, it is apparent that this recipe yields a highly anisotropic and reasonably vertical sidewall. However, some vertical striations are visible, indicating some roughness of the etched sidewalls. This etch took 36 minutes. The etch rate is only 0.061 $\mu$ m/min. For an etch depth of 16 microns, it would take a lengthy 262 minutes. Thus, we moved to an ICP-RIE in order to achieve faster etch rates while hoping to keep the anisotropy and verticality of this etch.

The etch mask we used consisted of RF sputtered silicon dioxide. With this etch mask material, we measured an etch selectivity of approximately 70:1 between PFCB and silicon dioxide for a typical etch recipe in the ICP-RIE. With such a selectivity we can potentially etch 20 $\mu$ m deep with an etch mask only 290nm thick. In practice we used thicker etch masks to have a broader process latitude. Figure 7.3 is an SEM cross-section image of a typical etch mask before the air trench etch.

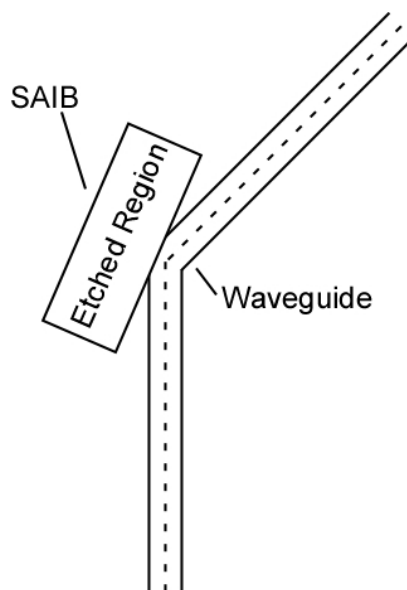


Figure 7.1. A SAIB consists of an etched region placed at the intersection of a sharp waveguide bend.

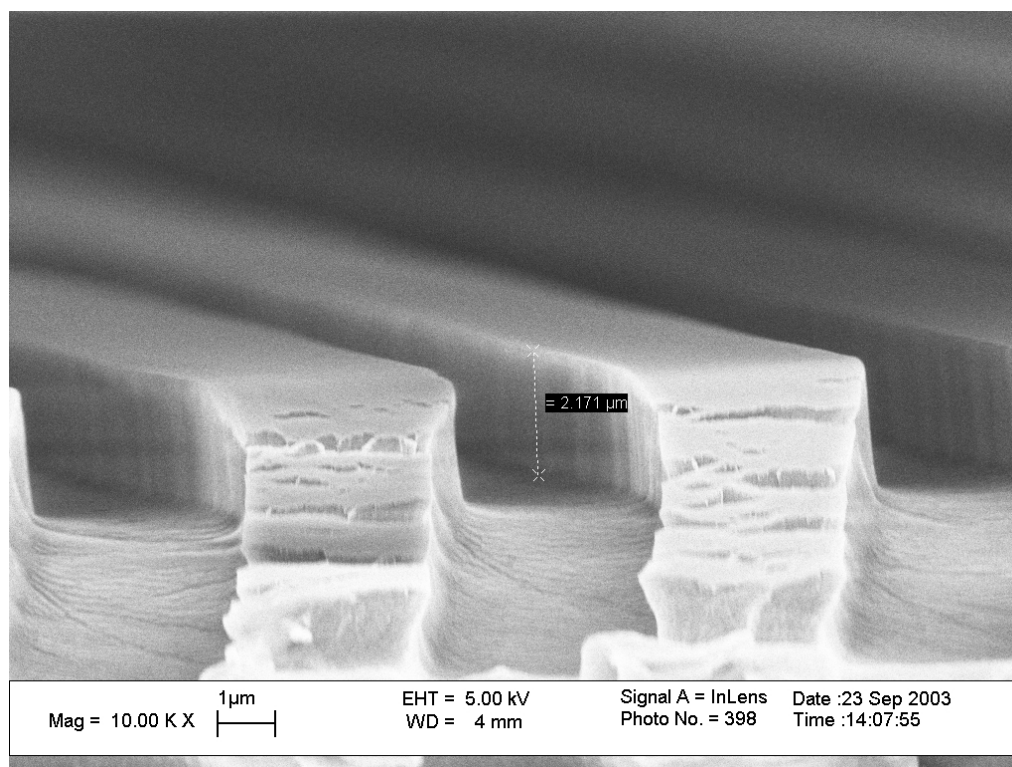


Figure 7.2. SEM image of  $2\mu\text{m}$  features etched in PFCB polymers in an RIE at 175W and 12:8 sccm of oxygen to helium. The etch took 36 minutes. Note the plastic deformation due to the cleaving of the sample during preparation for SEM imaging.

We transferred the oxygen and helium etch recipe from the RIE to the ICP by using the same gas ratios, and set the coil power to 300W and the platen power to 300W as well, while maintaining the platen temperature at 20°C during the etch. With this recipe, we etched 2 $\mu\text{m}$  features and observed a small amount of undercut. Additionally, 0.5 $\mu\text{m}$  features were etched and, as can be seen in Figure 7.4, the undercut is too great to etch this size feature to a significant depth. While this etch recipe isn't suitable for such small features, we tested it on 50 $\mu\text{m}$  features since SAIBs can use relatively large features. The result was a highly anisotropic, vertical trench with an etch rate of 0.93  $\mu\text{m}/\text{minute}$ . The measured sidewall angle departs from ideal verticality by only 0.7° (see Figure 7.5).

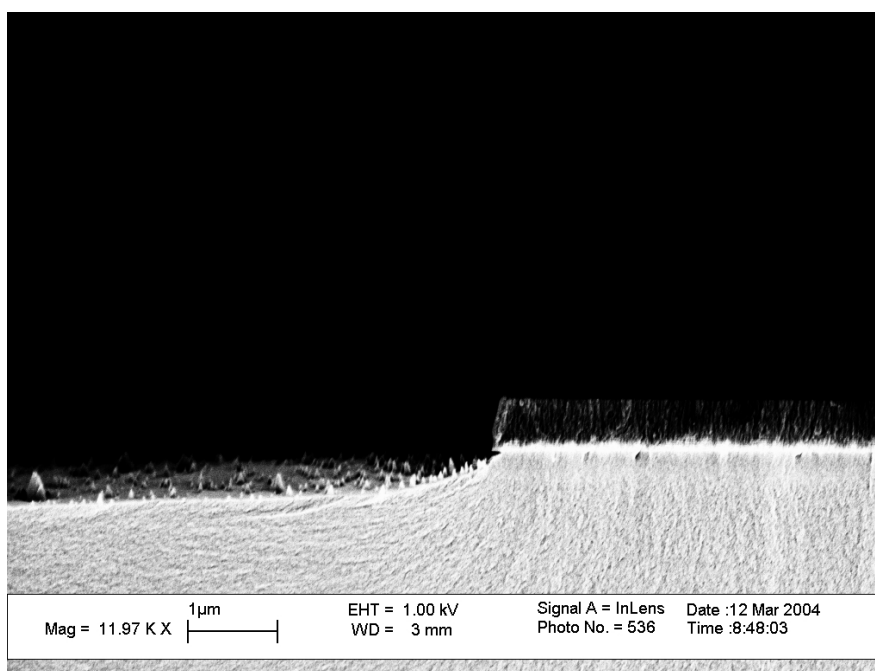


Figure 7.3. Cross-section image of etched silicon dioxide etch mask. Notice the slightly sloped sidewall and the “grassy” bottom on the PFCB surface from overetching.

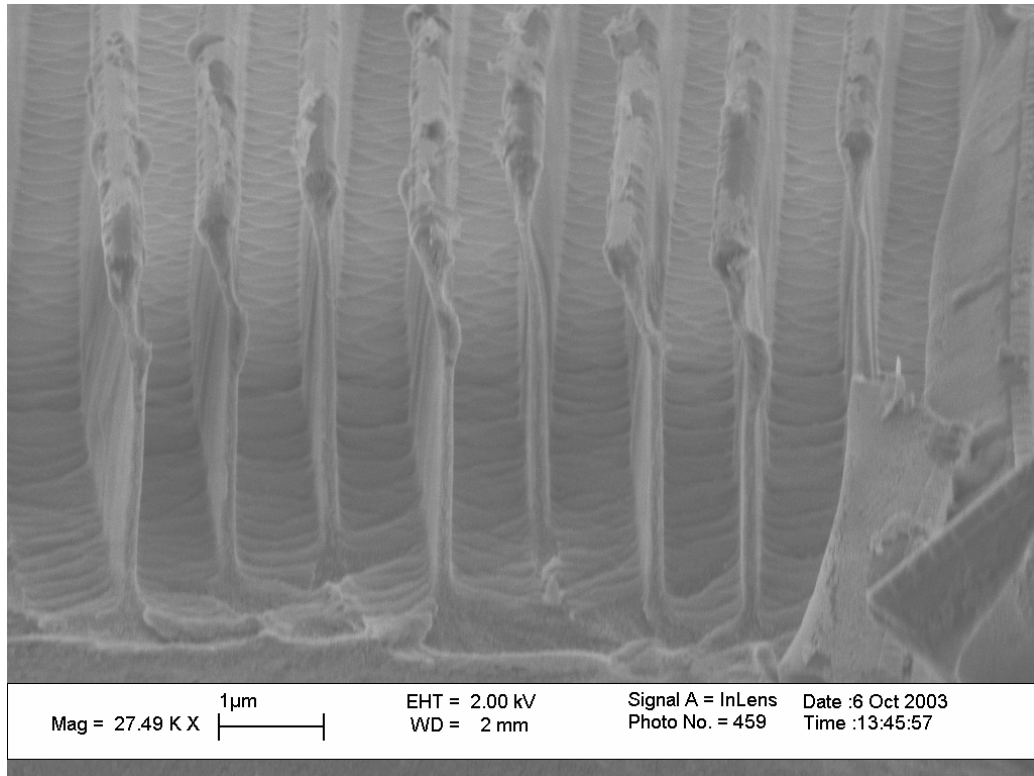


Figure 7.4. Half micron features etched into PFCB with an oxygen/helium chemistry.

The effect of platen temperature on the sidewall angle can be observed by comparing Figures 7.6 (a) and (b). When the platen temperature was set at 5°C, the sidewall was slanted into the trench. On the other hand, with the platen temperature at 35°C, the sidewall became re-entrant and it slanted away from the trench.

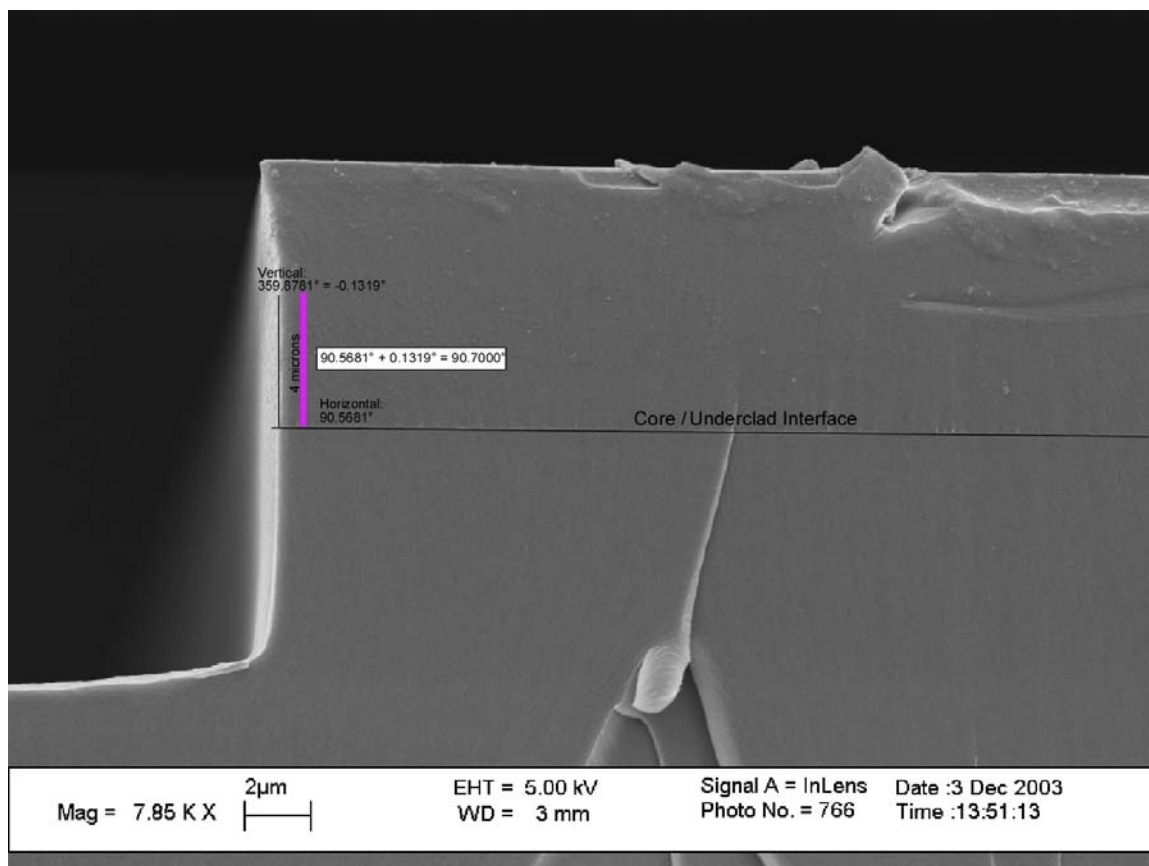


Figure 7.5. SEM image of cross-section for typical oxygen/helium etch of  $50\mu\text{m}$  features. At the depth of the waveguide core, the sidewall was measured to be  $90.7^\circ$ , which is only  $0.7^\circ$  from ideal verticality.

Up to this point, we have an etch process that meets two of the three criteria necessary for making high efficiency SAIBs. The last requirement is low sidewall roughness. It can be seen in Figure 7.7 that the sidewall has visible roughness for the etch process used for the result shown in Figure 7.5. There are two components to this roughness: fine roughness near the top of the trench, and larger vertical striations that go all the way from the top to the bottom of the trench. Since the small scale roughness is only present at the top of the etch and we don't see it during shallower etches, we believe it is due to the length of exposure of the polymer to the oxygen etch chemistry. On the

other hand, the vertical striations are most likely due to imperfections in the etch mask that are transferred to the trench through the etch process.

To attempt to reduce the roughness, we tried different strategies such as varying the parameters of the oxygen/helium recipe, different etch gases, and different etch mask materials. However, while reducing the sidewall roughness, we didn't want to sacrifice sidewall angle, nor anisotropy. We found that different coil and platen powers did little to help and degraded the sidewall verticality.

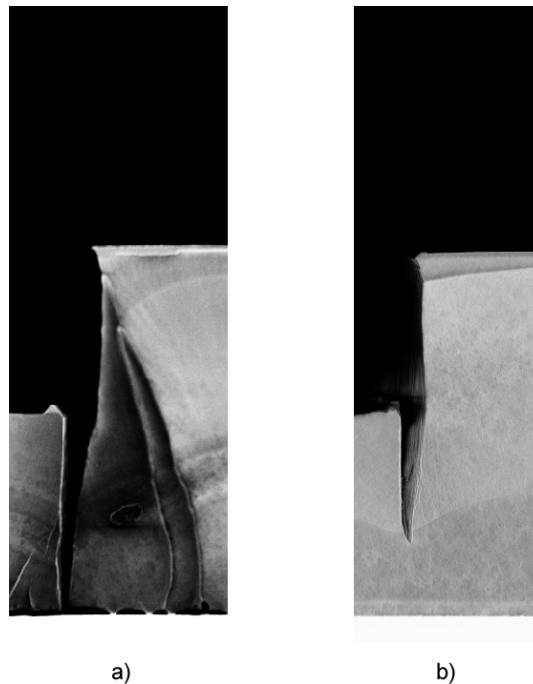


Figure 7.6. Sidewall angle dependence on platen temperature during the etch process. (a) Platen temperature at 5°C. (b) Platen temperature at 35°C.

Using carbon dioxide instead of oxygen with and without helium, yielded a slower etch rate and the sidewalls became slightly bowed. In Figure 7.8 (a) and (b) it can be seen that the small scale roughness appears to be reduced. However, notice that the etch depth is much shallower for equal etch times and the small scale roughness is

already starting to appear at the top of the etched sidewall. Thus, for an etch of comparable depth it seems unlikely that this etch will result in reduced small scale roughness. Part (b) of the figure shows that the sidewall has some bowing, although it isn't clear if this is due to plastic deformation from cleaving or from the etch process.

Finally, we tried to use SU8 as an etch mask. But, in order to spin cast the SU8 layer, first a 50nm protective silicon dioxide layer was deposited. This layer prevents the cyclopentanone solvent in SU8 from dissolving the fully cured PFCB polymer. As can be seen in Figure 7.9, the small scale sidewall roughness didn't change very much and the vertical striations weren't reduced. It is interesting that the SU8 closest to the trench etched much slower than the rest of the SU8. We believe this is due to the sidewall being passivated with byproducts from the etched PFCB.

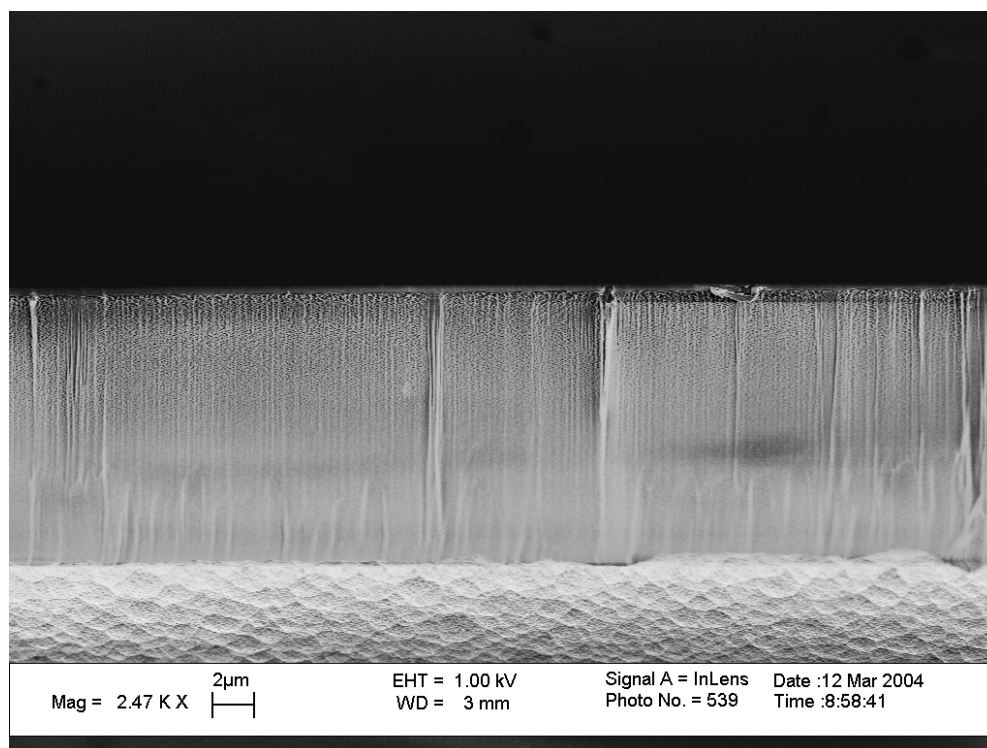


Figure 7.7. Typical sidewall roughness observed in oxygen/helium etch of PFCB.

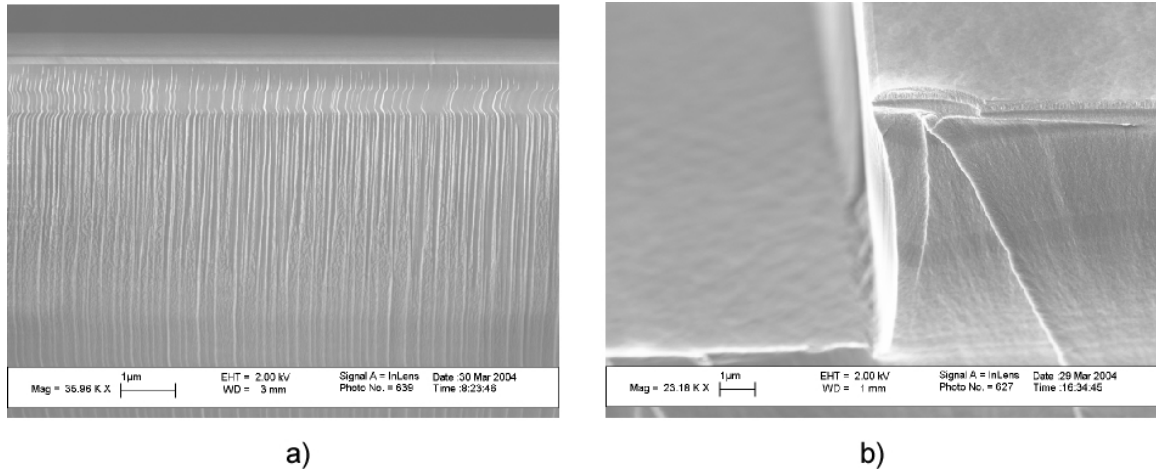


Figure 7.8. Carbon dioxide only etch of  $50\mu\text{m}$  features in PFCB. a) Sidewall roughness appears to be reduced, but the etch depth is shallower. b) The bowing may be due to plastic deformation from cleaving.

We fabricated SAIBs using the oxygen/helium etch recipe to make the trenches. In our initial design the SAIBs had the rectangular shape shown in Figure 7.1. However, the sharp corners resulted in stress cracks after the trenches were etched (see Figure 7.10). In order to avoid this problem, which may go through waveguides and ruin the device, we rounded the edges of the SAIB. The devices that we fabricated (see Figure 7.11) and tested yielded a bend efficiency of 93.4% [3]. Further research is focused on reducing the sidewall roughness through the addition of other gases to oxygen and the reduction of roughness on the silicon dioxide etch mask.

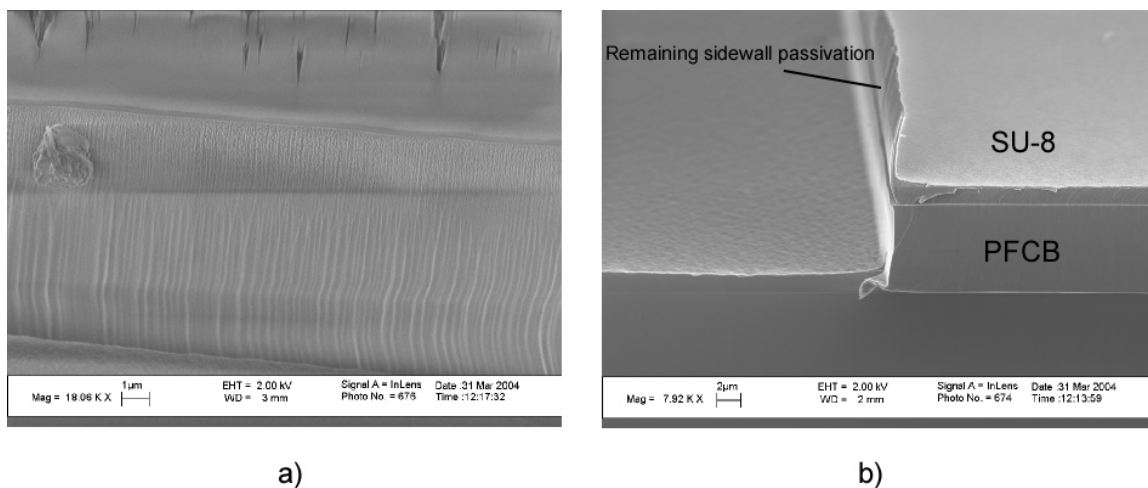


Figure 7.9. (a) PFCB trench sidewall when SU8 is used as an etch mask. The horizontal line in the middle of the image is due to charging during the SEM scanning. (b) Angled view of etched trench showing some SU8 remaining from the etch. The thin vertical feature that sticks out along the sidewall of the trench may be due to sidewall passivation from the byproducts of the PFCB when it is etching.

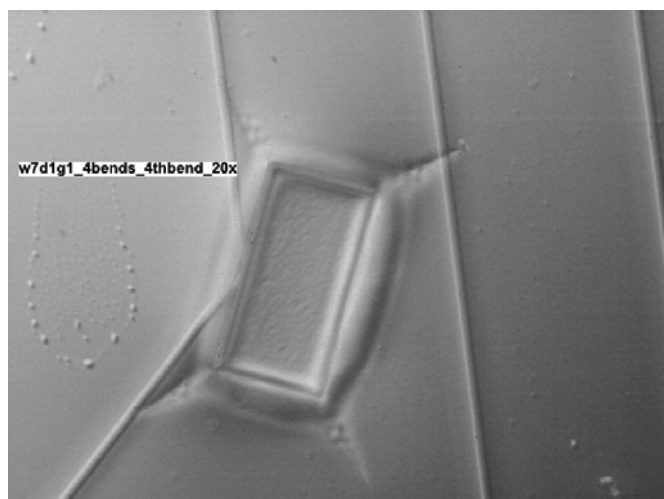


Figure 7.10. Optical microscope image through DIC filter of a rectangular SAIB. The sharp corners caused stress cracks. In this case, one of the cracks goes through an adjacent waveguide.

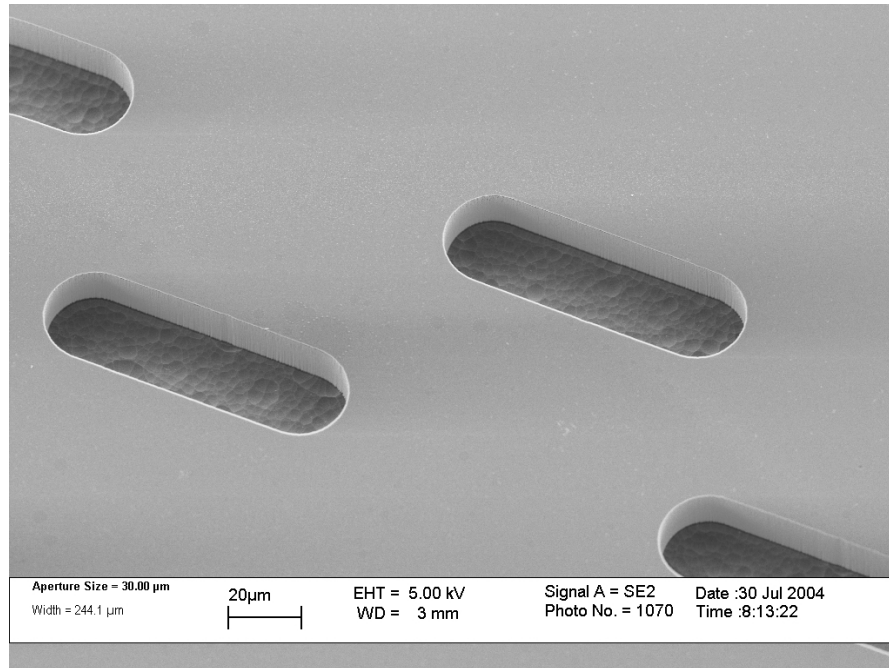


Figure 7.11. Fabricated SAIBs with rounded edges in PFCB polymers. These structures yielded a measured optical bend efficiency of 93.4%. However, some sidewall roughness is visible. Eliminating this roughness should improve the bend efficiency.

### 7.3 Etch Roughness Reduction

In the previous section we discussed that the etch process used to make the SAIBs with 93.4% bend efficiency produced sidewalls with considerable roughness (refer to Figures 7.7 and 7.11). Among the possible loss mechanisms at the bend we have misalignment, undercut, and scattering. The first two will be discussed in the latter parts of the next chapter, while this section delves into the work done to try to reduce the sidewall roughness in order to minimize scattering losses at the bend's interface. The roughness seen on the sidewalls of the oxygen/helium etch could be due to lithography transfer, etch mask etching, or polymer etching. Our initial hypothesis is that the vertical striations are most likely due to lithography transfer to the etch mask while

the small scale roughness is due to the chemical interaction between the oxygen and the polymer during the etch. In the next sections we will discuss the development of an improved silicon dioxide etch for the etch mask and finally a new etch process using different gases in an effort to reduce the sidewall roughness.

While the vertical striations are most likely due to lithography transfer, mask erosion during the polymer etch could also cause them if the mask erodes unevenly. The original silicon dioxide etch produced sidewalls that deviated significantly from the ideal 90°. Additionally, the etch was so slow that it took several hours to etch through the silicon dioxide layer. Thus, we worked on improving the silicon dioxide etch before looking into the other possible mechanisms for the polymer sidewall roughness.

### 7.3.1 Improved Silicon Dioxide Etch

Song, et al. reported using octafluorocyclobutane ( $C_4F_8$ ), carbon monoxide, oxygen, and argon to etch silicon dioxide with vertical sidewalls [55]. We decided to explore the use of octafluorocyclobutane and oxygen using design of experiments (DOE). DOE is a statistical tool that helps the experimenter extract information out of the data generated from experiments [56]. It also helps reduce the number of runs needed to cover a parameter space and gain enough information to decide what region of the parameter space warrants further study. This can be done by using a fractional factorial design. With this type of design, a preliminary study of a parameter space with four variables with two possible values can be done with less than 16 runs, which would account for every single combination of values. In most cases, only a few of the variables affect the outcome significantly. A full factorial design can be run to study these few after the preliminary

experiment. (For a detailed study of design of experiments the reader may see [56], [57], or [58].) Using a one quarter fractional factorial design, we explored the parameter space. The variables that we chose to vary were chamber pressure, coil power, platen power, oxygen flow, and octafluorocyclobutane flow. The order of the experiment runs was randomized to avoid mistaking an effect due to an uncontrolled variable for one of the variables being studied. We measured the sidewall angle and the etch rate using images taken with a scanning electron microscope (SEM). The details of the experiment are shown in Table 7.1. The column labeled Std refers to the experiment order before randomization, while the column labeled Run refers to the order in which the experiments were run. The sidewall angle column contains the measured angle with  $0^\circ$  being a perfectly vertical sidewall and the angle increasing clockwise.

Table 7.1. Details of exploratory experiment for silicon dioxide etch process.

Std	Run	Factor 1	Factor 2	Factor 3	Factor 4	Factor 5	Response 1	Response 2
		A:Chamber Pressure	B:Coil Power	C:Platen Power	D:O2 flow	E:C4F8 flow	Etch Rate	Sidewall Angle
		mTorr	W	W	sccm	sccm	nm/min	degrees
3	1	4	300	50	5	15	95.3	12.03
8	2	16	300	200	10	15	99.2	10.3
1	3	4	100	50	10	15	37.5	13.95
2	4	16	100	50	5	10	17.6	37.9
7	5	4	300	200	5	10	197	7.85
5	6	4	100	200	10	10	70.3	11.05
6	7	16	100	200	5	15	47.5	37.85
4	8	16	300	50	10	10	55.6	9.08

The main goal of this initial run is to find how the etch rate and the sidewall angle are affected by the different parameters. However, it can also tell us if photoresist will work as an etch mask and if we can get reasonable etch rates with the octafluorocyclobutane and oxygen chemistry.

In this case, we found that the photoresist works as an adequate etch mask and that within the parameter space explored, this etch chemistry yields reasonable etch rates. However, even though we didn't run samples for every possible combination of the parameters, we can create a model that predicts the results of such runs. In Figure 7.12 we show a cube graph of sidewall angle vs. three of parameters that were varied. These parameters are the only ones that significantly affect the sidewall angle. They are chamber pressure, coil power, and oxygen flow. As can be seen in the figure, the model predicts that for a chamber pressure of four milliTorr, a coil power of 300 Watts, and an oxygen flow of 10 sccm, the sidewall angle would be  $-2.87^\circ$ . This result suggests that the next experiment must focus on an area around these operating values, while choosing operating points for octafluorocyclobutane flow and platen power.

On the other hand, the etch rate doesn't depend on oxygen and octafluorocyclobutane flow. However, at a higher platen power the etch rate is higher. Thus, we included platen power in the follow-up experiment to develop the etch recipe.

For the next experiment we took the starting points learned from the exploratory experiment and designed a new experiment with only four variables. These variables are chamber pressure, coil power, platen power, and oxygen flow. We kept the octafluorocyclobutane flow constant at 10sccm and etched the samples for two minutes. The experiment details are shown in Table 7.2.

In this case we can see in Figure 7.13 that there are several parameter combinations that yield highly vertical sidewalls. The model predicts that for a chamber pressure of two milliTorr, a coil power of 400 Watts, and a platen power of 200 Watts, the sidewall angle is  $0.90^\circ$ . However, the sample of the actual run with these parameters didn't have any photoresist left. On the other hand, another parameter combination of chamber pressure equal to four milliTorr, coil power equal to 300 Watts, and platen power equal to 300 Watts, has a predicted sidewall angle of  $0.85^\circ$ . For this parameter combination, there is some photoresist left (Figure 7.14 compares the profile for this  $\text{SiO}_2$  etch process and the one etched in the RIE). This means that the etch could have gone on for longer than two minutes and that thicker layers of silicon dioxide can be etched with the same photoresist thickness. It is important to note that both of these data points from the model correspond to parameter combinations that were actually run in the experiment. It can be seen, by comparing the values from Table 7.2 with those from Figure 7.13 (0.27 in the table vs.  $0.90^\circ$  in the figure for the first case and 0.3 in the table vs.  $0.85^\circ$  in the figure the second case) that this is the case. There are small differences because the model is built with the results from all the experiment runs and there is noise in the experimental conditions as well as in the measurement process. Because of this noise, the predicted results aren't identical to the measured data points.

DESIGN-EXPERT Plot

Sidewall Angle

X = A: Chamber Pressure

Y = B: Coil Power

Z = D: O2 flow

Actual Factors

C: Platen Power = 125.00

E: C4F8 flow = 12.50

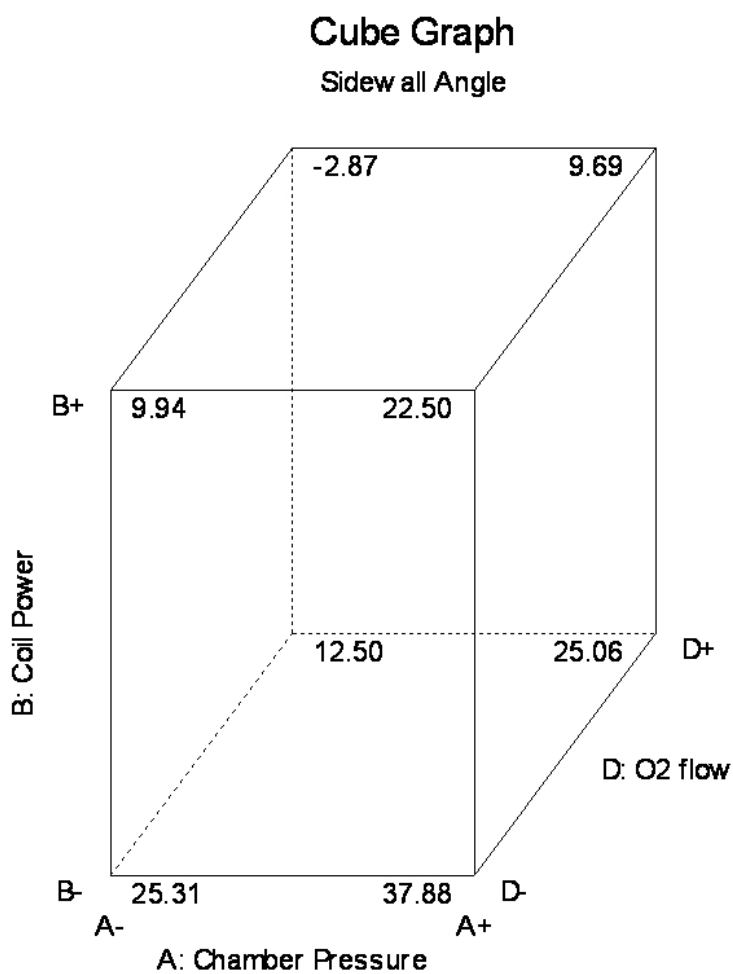


Figure 7.12. Plot showing the effect of the main parameters affecting the sidewall angle.

Table 7.2. Details of silicon dioxide etch process development experiment.

Std	Run	Factor 1	Factor 2	Factor 3	Factor 4	Response 1
		A:Coil Power	B:Platen Power	C:Chamber Pressure	D:O2 Flow	Sidewall Angle
		Watts	Watts	mTorr	sccm	degrees
6	1	400	200	4	10	5.47
5	2	300	200	4	15	27.67
2	3	400	200	2	15	0.27
1	4	300	200	2	10	31.53
3	5	300	300	2	15	6.37
7	6	300	300	4	10	0.3
8	7	400	300	4	15	1.67
4	8	400	300	2	10	-1.03

DESIGN-EXPERT Plot

Sidewall Angle

X = A: Coil Power

Y = B: Platen Power

Z = C: Chamber Pressure

Actual Factor

D: O2 Flow = 12.50

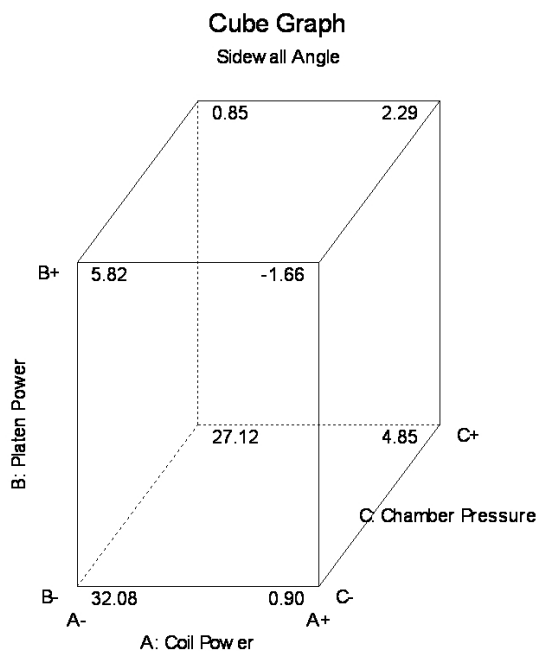
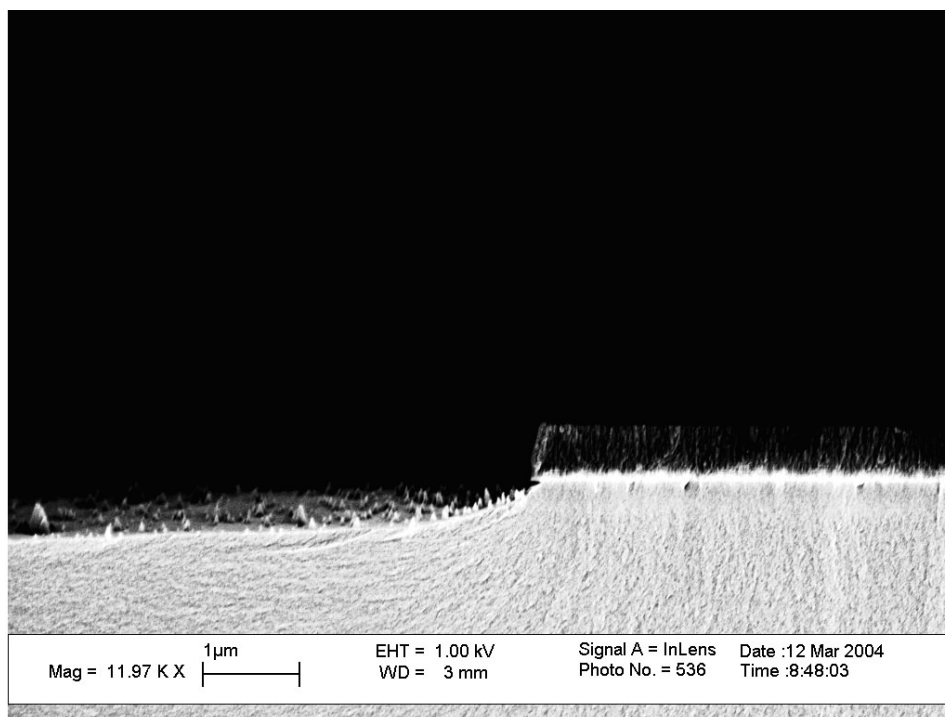
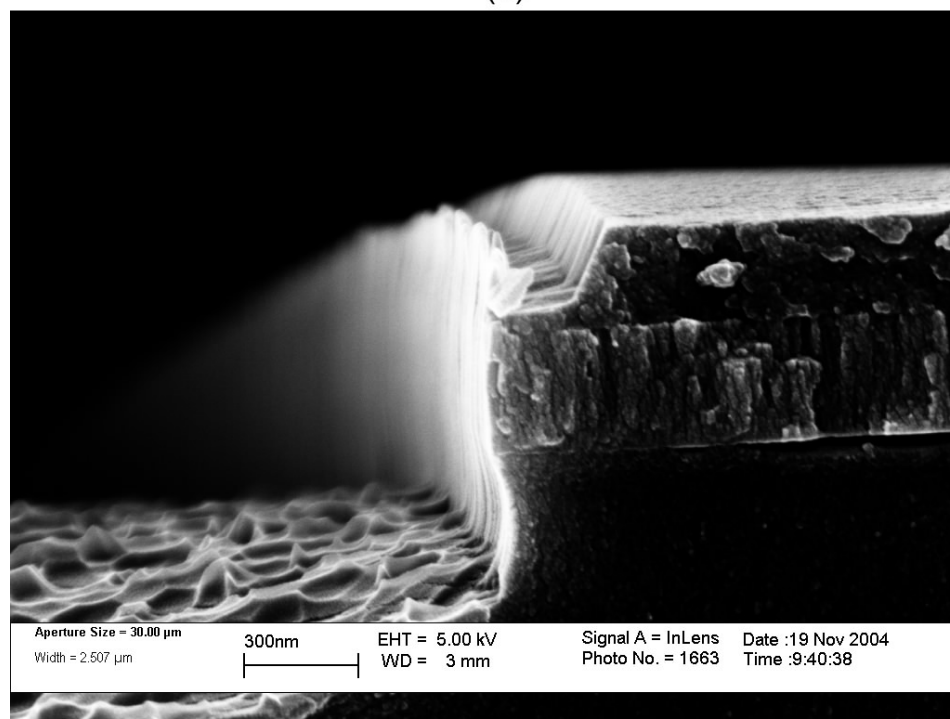


Figure 7.13. Effect of the significant parameters affecting the silicon dioxide sidewall angle. Note that the front bottom right corner and the back top left corner deviate from the ideal vertical sidewall by less than one degree.



(a)



(b)

Figure 7.14. Comparison of SiO<sub>2</sub> etch mask profile after (a) RIE etch process, and (b) optimized SiO<sub>2</sub> etch in ICP RIE.

For this experiment run, the oxygen flow didn't have a significant effect in the sidewall verticality. While it seems that this contradicts the results from the previous experiments, this time we have expanded the range in which we examined the parameter's effects. Thus, it is possible that in this region oxygen flow doesn't affect the sidewall verticality significantly. Further work would be needed to find out with certainty.

Thus, with this development work using DOE techniques, we have found a parameter combination that yields an etch with highly vertical sidewalls that uses photoresist as an etch mask. With this etch mask profile we can concentrate on reducing surface roughness that could be due to lithography transfer or the polymer etching. We will study these causes in the next section.

### 7.3.2 PFCB Etching with Reduced Sidewall Roughness

Our hypothesis is that the sidewall roughness is due to lithography transfer and the plasma etch process. The roughness due to lithography transfer originates in the photomask used to pattern the air trench features. Ladoceur, et al. have reported high correlation between the roughness present on the photomask and the roughness transferred to the pattern in the photoresist through contact lithography [52]. Photomasks typically consist of a chrome pattern on a quartz plate. In most photomasks the chrome is wet etched. The chrome is dry etched only in high end masks of considerable cost. However, the dry etch process yields smoother sides on the chrome features. To test the contribution of the photomask roughness to the sidewall roughness observed in the air trenches, we used a high end photomask from Compugraphics. This mask was made in one of their high end tools with dry etched chrome. We also used a mask fabricated with

the conventional wet etching process. Additionally, we baked the sample on a hot plate after developing to try to get some reflow of the photoresist to reduce roughness transferred from the lithography [59]. On the other hand, we tried a different etch chemistry using carbon monoxide and oxygen which relies on sidewall passivation to maintain a vertical sidewall.

To explore this parameter space, we designed another fractional factorial experiment with five variables. These variables are photomask type, hot plate temperature, hot plate time, oxygen flow, and carbon monoxide flow. The specific values used for each parameter are included in Table 7.3. This experiment was run on samples with about 20 $\mu$ m of PFCB polymer on a silicon substrate with 330nm of silicon dioxide as an etch mask. Half of the wafer was patterned with the wet etched photomask and the other with the dry etched one. The wafer was cleaved into small pieces and each piece was processed further according to the parameters in Table 7.3. The silicon dioxide in all of the samples was etched with the recipe developed in the previous section. The parameters of the polymer etch recipe that weren't varied are coil power at 500 Watts, platen power at 200 Watts, chamber pressure at 5 milliTorr, and platen temperature at 10°C. The samples were imaged in the SEM and they were measured qualitatively on a scale of one (smoothest) to five (roughest). To make the qualitative judgment more repeatable it was done by deciding how rough a one would be, and a two, and so on. Then we estimated what fraction of the sidewall had what roughness and multiplied the qualifying number by this fraction. This was finally added to compute the sample's roughness.

In Figure 7.15 we can see the effect of significant parameters on sidewall roughness. The best result seems to be the sample patterned with the dry etched mask, a hot plate temperature of 100°C, and an oxygen flow of 8 sccm. However, this point is predicted by the model and wasn't directly measured. Since the measurement is qualitative, it is difficult to say whether the prediction is accurate without running a sample with those parameters. Nonetheless, this experiment has pointed us in the right direction. Let's compare the SEM image from the "Run 7" sample (see Table 7.3 next to last row) to the one in Figure 7.7, which is included for convenience, in Figure 7.16. Notice that the image for the sample with the carbon monoxide and oxygen etch is so smooth in its top 40% that the roughness isn't perceptible. Additionally, while the roughness increased with etch time for the oxygen and helium etch, in this case the opposite seems to happen. This data indicates that another experiment should be run while varying more parameters of the etch process.

Table 7.3. Details of the polymer etching experiment.

Std	Run	Factor 1	Factor 2	Factor 3	Factor 4	Factor 5	Response 1
		A:Mask Type	B:HP Temperature	C:HP Time	D:O2 Flow	E:CO Flow	Roughness
			deg C	s	sccm	sccm	
3	1	Wet Etched	120	60	2	42.9	1.5
7	2	Wet Etched	120	120	2	21.4	2
2	3	Dry Etched	100	60	2	21.4	2.9
8	4	Dry Etched	120	120	8	42.9	2.85
6	5	Dry Etched	100	120	2	42.9	2.5
5	6	Wet Etched	100	120	8	21.4	2.35
1	7	Wet Etched	100	60	8	42.9	2.9
4	8	Dry Etched	120	60	8	21.4	2.35

DESIGN-EXPERT Plot

Roughness

X = A: Mask Type

Y = B: HP Temperature

Z = D: O2 Flow

Actual Factors

C: HP Time = 90.00

E: CO Flow = 42.90

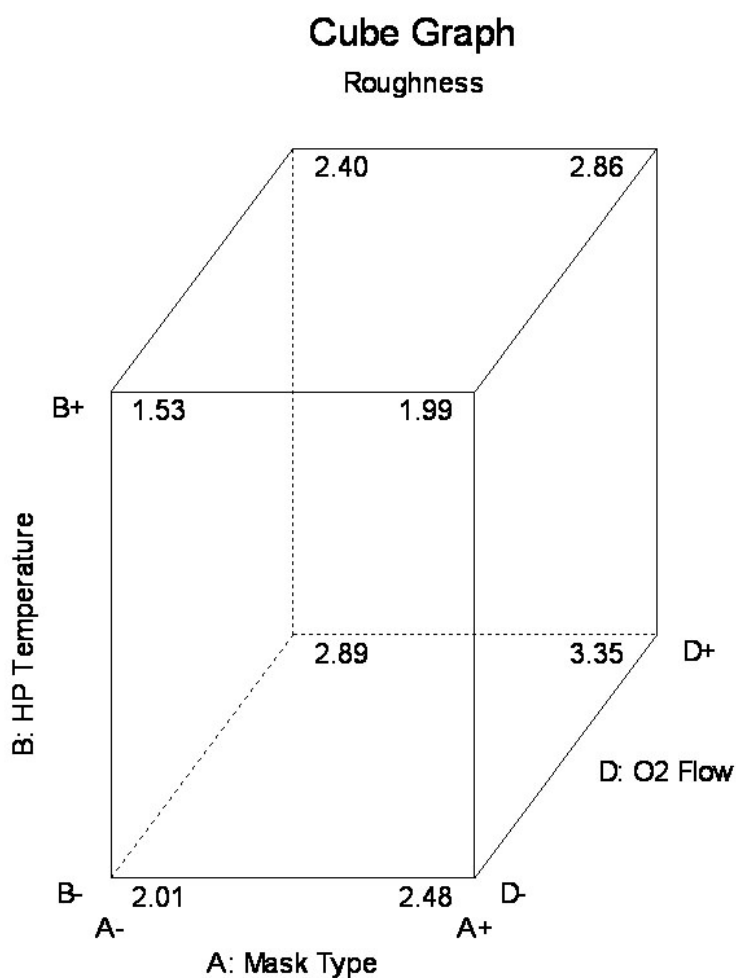
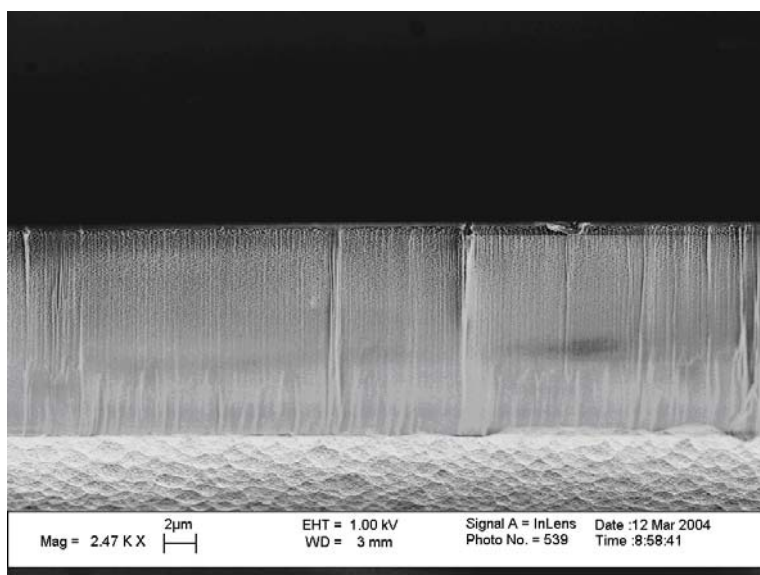
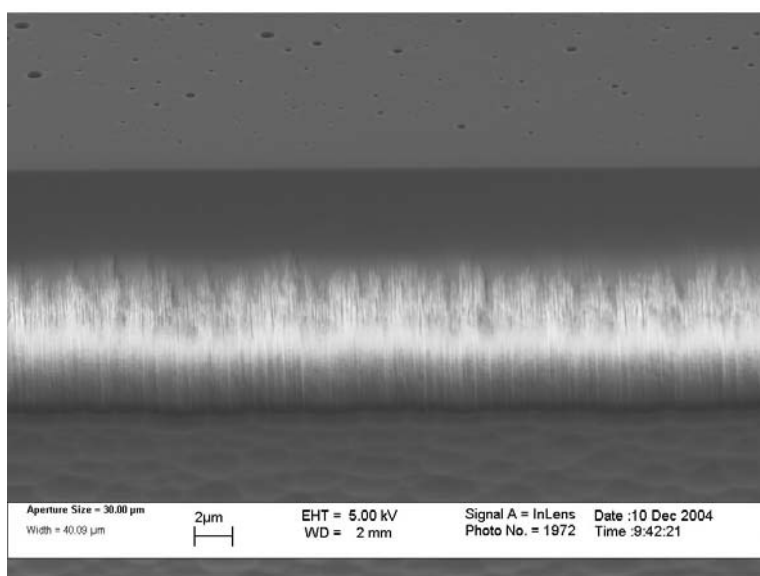


Figure 7.15. Effect of significant parameters affecting sidewall roughness. For the mask type axis, A- stands for “wet etched”, while A+ stands for “dry etched”.



(a)



(b)

Figure 7.16. Comparison of (a) typical oxygen/helium etch sidewall vs. (b) carbon monoxide/oxygen etch for “Run 7”. Note that (b) looks rougher than (a) in a good portion of the sidewall. However, this etch gets smoother as the sidewall is exposed longer to the process. This data suggests that further investigation is warranted for this etch chemistry.

## 7.4 Conclusion

We developed an etch process in an ICP-RIE using oxygen and helium that yields a highly anisotropic vertical sidewall. These are very important features needed to fabricate a low loss single air interface bend. Actually, as discussed in the next chapter, with this recipe we measured bends with a loss of 0.3 dB/bend. However, the roughness on the sidewall was significant. To reduce this we tried an etch process with carbon monoxide and oxygen. For this new process we applied design of experiments to extract data from our experiments more efficiently. The results obtained up to the time that this dissertation was written are promising. Important improvement can be seen with new etch chemistry. However, further experimentation is required around the process values where the improvement was observed.

## **CHAPTER 8**

### **FABRICATION AND MEASUREMENT OF 45° SINGLE AIR INTERFACE BENDS IN PFCB POLYMERS**

The contents of this chapter were published in Optics Express © OSA [6]. In this chapter, the motivation, design, fabrication, and measurement of 45° single air interface bends with a footprint of 80 $\mu$ m by 40 $\mu$ m are presented. These devices had a loss of 0.3dB/bend. The simulations were performed by Dr. Seunghyun Kim and he wrote the corresponding section.

#### **8.1 Introduction**

It is difficult to realize very small planar lightwave circuits (PLCs) in low loss waveguide material systems in which the refractive index contrast is typically in the range of 0.3% to 1.5%. This is primarily because the minimum bend radius typically must be at least several millimeters to achieve high optical throughput. In the literature, several different methods for reducing the area of a waveguide bend have been reported. For example, the minimum bend radius can be significantly reduced by creating a region

of large refractive index contrast at the bend by etching deep trench structures [60]. These structures define not only the bends, but also tapered transitions into and out of the bends [37]. The total area required for a bend therefore consists of both the bend itself and the taper regions. Another method consists in using corner mirrors based on hybrid integration of photonic crystals with conventional waveguides [61] or single air interface bends (SAIBs) [34], both of which can change the mode's direction in a very small area. SAIBs have been proposed for a variety of waveguide material systems and operating wavelengths [34], [38], [39], [40], [62], [63], [64]. However, high efficiency single air interface bends in low refractive index contrast waveguides have yet to be demonstrated.

As proposed in Ref. [34], SAIBs with bend angles smaller than  $90^\circ$  can be used to achieve high optical efficiency in low refractive index material systems. This strategy insures that total internal reflection occurs for all angular spectrum components of the waveguide mode, thus resulting in a high efficiency bend. In this chapter we report the design, fabrication, and measurement of high efficiency single air interface  $45^\circ$  bends in waveguides with a refractive index contrast of 1.3% using perfluorocyclobutyl (PFCB) copolymer materials [65], [66]. These polymers offer low propagation loss and a high glass transition temperature of over  $200^\circ\text{C}$  [67].

In the following sections, we first discuss the design of SAIBs and determine their placement tolerance. This is followed by a description of our fabrication process. In the last section, we report our measurement results.

## 8.2 Single Air Interface Bend Analysis

Based on core and clad PFCB copolymer formulations supplied by Tetramer Technologies, Inc., we designed single mode channel waveguides to operate at a wavelength of  $1.55\mu\text{m}$ . The core dimensions are  $3.6\mu\text{m} \times 3.6\mu\text{m}$ . The core refractive index is 1.4836 for TE polarization (electric field in the plane of the substrate) and 1.4816 for TM polarization (electric field out of the plane). The TE and TM cladding refractive indices are 1.4644 and 1.4625, respectively. To form a small area bend, a SAIB structure is placed at the intersection of two straight waveguides as shown in Figure 8.1. The red region represents an air trench etched vertically into the waveguide cladding/core/cladding stack. It provides a PFCB/air interface to reflect the waveguide mode through total internal reflection (TIR). In the following discussion, the origin (labeled O in Figure 8.1) is taken as the point at which the centers of the waveguides intersect, and the distance between the PFCB/air interface and the origin along the z axis is  $z_p$ .

To numerically calculate the optical performance of SAIB structures, we use a rigorous two-dimensional finite difference time domain (2-D-FDTD) method. The geometry and magnitude squared time averaged fields at  $\lambda=1.55\mu\text{m}$  for both TE and TM polarizations for our  $45^\circ$  bend are shown in Figures 8.2 (a) and 8.2 (b). The edge of the air interface is placed at  $z_p = -0.2\mu\text{m}$ . At this position, the Goos-Hanchen shift is such that the bend efficiency is nearly equal for both TE and TM polarized light. The bend efficiencies are calculated from the FDTD simulations with a mode overlap integral (MOI), which gives the ratio of the power in the guided mode in the output waveguide to

the power in the incident guided mode. At a wavelength of  $1.55\mu\text{m}$ , the calculated efficiencies using 2-D FDTD are 99.0% and 98.7% for TE and TM polarizations, respectively. To verify these results, we determined the efficiencies using a 3-D FDTD method implemented on a Linux cluster, which gave 98.5% for TE polarization and 98.0% for TM polarization. Since the 2-D and 3-D FDTD results are within one percent of each other and 3-D FDTD analysis is so computationally intensive, we use 2-D FDTD calculations throughout the remainder of this chapter.

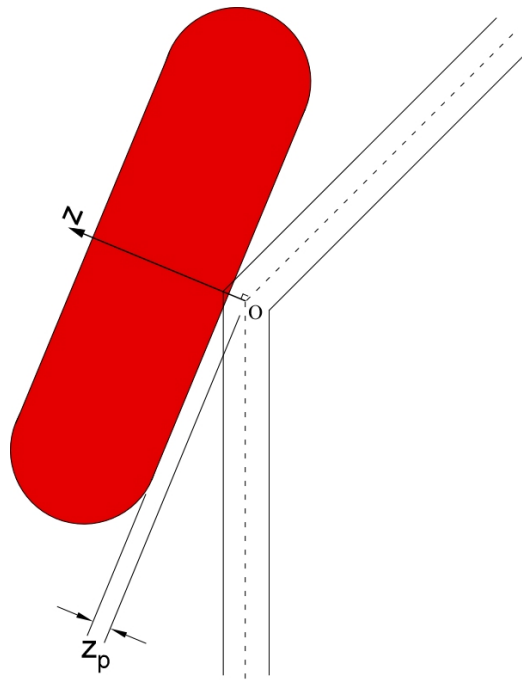


Figure 8.1. Top view of SAIB structure for a  $45^\circ$  waveguide bend showing the air interface placement and choice of reference point for design.

For device fabrication it is important to understand the effect of misalignment and etch undercut on the optical performance of SAIBs. In both cases, the result is misplacement of the SAIB interface with respect to the designed position. The bend efficiency as a function of this misplacement is shown in Figure 8.3. The alignment

accuracy must be better than  $\pm 0.3\mu\text{m}$  around the designed placement at  $z_p = -0.2\mu\text{m}$  to have a bend efficiency of 95% or greater for both TE and TM polarizations. The same applies to undercut. Thus, the misplacement of the air interface caused by the both misalignment and undercut must be less than  $\pm 0.3\mu\text{m}$  to achieve the aforementioned bend efficiency.

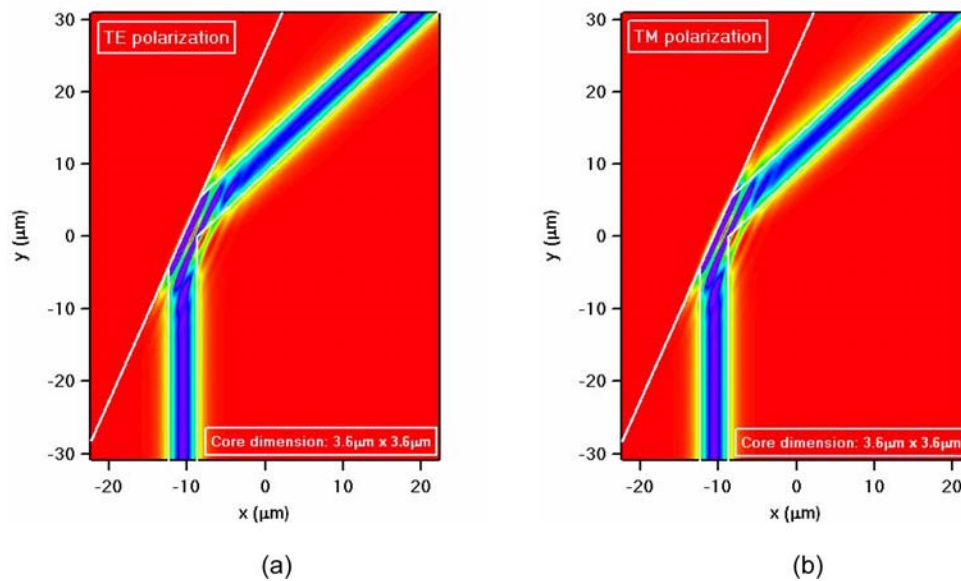


Figure 8.2. Magnitude squared time averaged (a) magnetic field plot (TE polarization) and (b) electric field plot (TM polarization) at  $\lambda = 1.55\mu\text{m}$ .

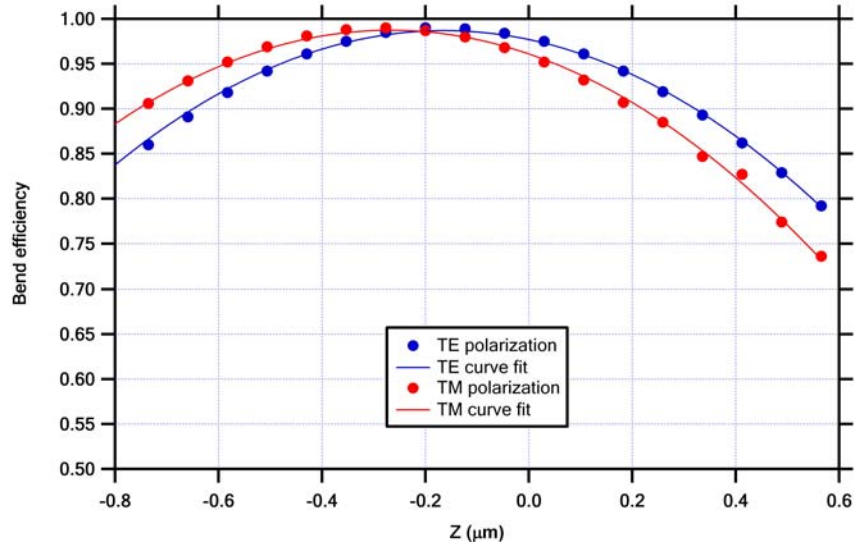


Figure 8.3. Bend efficiency as a function of the position of the air interface relative to the O position. The designed position of the SAIB is  $z_p = -0.2\mu\text{m}$ . Note that the vertical axis starts at a bend efficiency of 0.5.

### 8.3 Fabrication

We fabricated SAIBs in PFCB waveguides on a silicon substrate using typical microfabrication techniques. First, a  $12\mu\text{m}$  thick undercladding layer was spun and cured at  $190^\circ\text{C}$  followed by a  $3.7\mu\text{m}$  thick core layer. Next, we deposited silicon dioxide as a hard mask for the waveguide etch via RF sputtering and defined the waveguides using contact lithography with AZ 701 MiR i-line photoresist. Then, the silicon dioxide hard mask was etched in a  $\text{CHF}_3$  chemistry with a reactive ion etcher (RIE) followed by etching of the PFCB core layer in an inductively coupled plasma reactive ion etcher (ICP-RIE) using a helium and oxygen etch chemistry. After the waveguide core etch, the silicon dioxide layer was stripped in buffered hydrofluoric acid. The overcladding was then spun and cured at  $190^\circ\text{C}$ . Another silicon dioxide hard mask was deposited followed by photoresist pattern definition with contact lithography to define the air trench patterns.

The silicon dioxide was then etched in the RIE. Finally, the air trenches were etched in the ICP-RIE using a helium and oxygen chemistry.

As shown in the 2-D FDTD simulation results in Figure 8.3, the placement of the air trench interface with respect to the bend is critical. Moreover, contact photolithography doesn't allow us to align the SAIBs with the necessary tolerance. Thus, we introduced a range of predefined offsets into the photomask to compensate for actual misalignment during the fabrication process. These offsets compensate for a mask misalignment of up to  $\pm 1\mu\text{m}$  in  $0.1\mu\text{m}$  increments in both the x and y directions. Hence, if our alignment is less than or equal to one micron in x and y, at least one set of bends will be aligned to within  $0.1\mu\text{m}$  and the expected bend efficiency as per the 2-D FDTD simulations in Figure 8.3 will stay within 1% of the maximum.

Another fabrication issue that must be considered is that during the SAIB deep etch process the PFCB material beneath the edge of the etch mask is slowly undercut. After a  $14\mu\text{m}$  to  $16\mu\text{m}$  deep etch this undercut causes considerable misplacement of the SAIB interface. Thus, we introduced another set of offsets into the mask layout for undercut compensation. The range of this compensation goes from  $0.3\mu\text{m}$  to  $1.3\mu\text{m}$  of undercut in  $0.2\mu\text{m}$  increments. This means that if the air interface misplacement is due only to undercut then the interface for at least one set of SAIBs will be located to within  $0.1\mu\text{m}$  of its designed position for any undercut value in the  $0.2\mu\text{m}$  to  $1.4\mu\text{m}$  range. Figure 8.4 shows a cross-sectional SEM image of the sidewalls typically observed for our fabrication process. During the measurement of the samples, which is discussed in the next section, we found that the undercut must be close to  $1.1\mu\text{m}$ . However, during the etch process, there is mask erosion. Thus, even though the image shows an undercut of

1.1  $\mu\text{m}$ , we believe this is a coincidence and the distance measured is due to plastic deformation and real undercut. To observe mask erosion, several images at different intervals during the etch are needed.

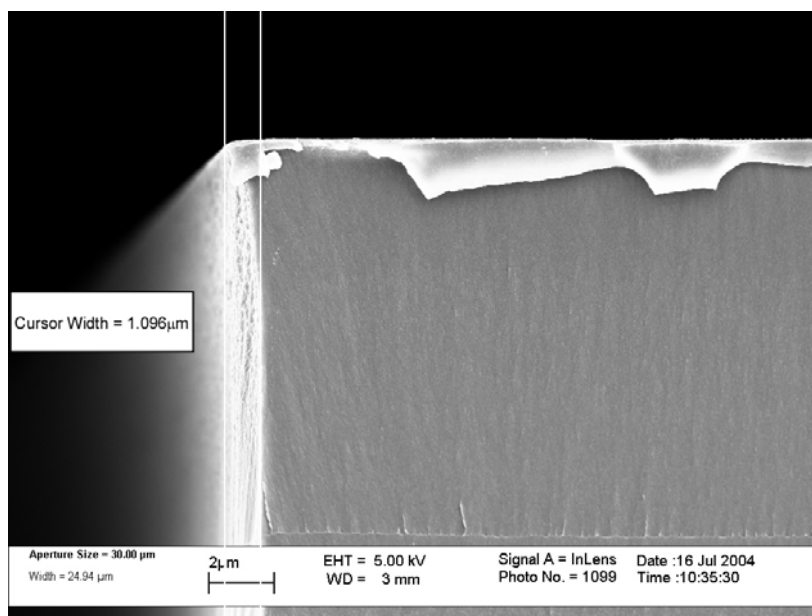


Figure 8.4. Cross-section SEM image showing the typical etch undercut (1.1  $\mu\text{m}$  as depicted by the cursor width) for an air trench.

For each combination of misalignment and undercut compensation, a set of waveguides was designed containing 2, 4, 8, and 16 bends. Each of these is termed a group. Nine of these groups are included in one 1.5cm x 1.5cm die, and two die are required to account for all of the misalignment offsets for each undercut compensation. Twelve die containing all possible misalignment and undercut combinations are fabricated on a single three inch wafer.

Even though we did not quantify the amount of mask misalignment on fabricated die we evaluated it qualitatively by looking at the symmetry of the air trench placement with respect to the waveguides from microscope images as illustrated in Figure 8.5. This

image of a pair of bends was taken with a DIC filter with the focus at the waveguide plane. It shows that the bends' symmetry with respect to the waveguides is quite good. This symmetry implies good alignment for this bend. We used this criterion to determine which waveguide groups to initially measure since better alignment results in higher bend efficiency.

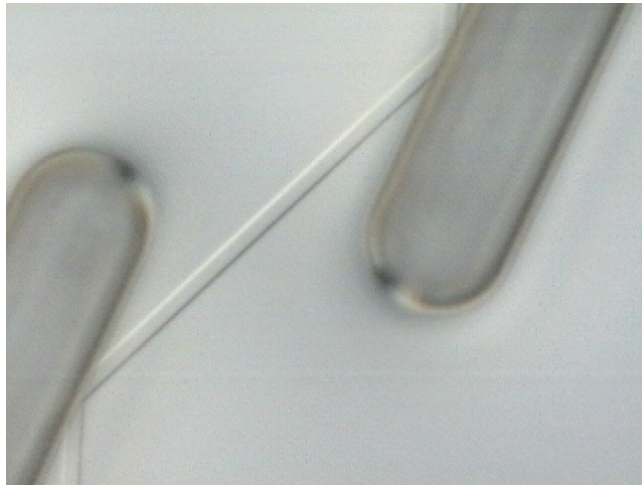


Figure 8.5. Microscope image taken with a DIC filter through a 50x objective focused at the waveguide plane of SAIBs in good alignment.

Figure 8.6 shows an SEM image of a finished air trench bend. It consists of a 25 $\mu\text{m}$  wide trench that is 87 $\mu\text{m}$  long. The waveguide isn't visible because it is buried between the under and overcladding layers. As illustrated in Figure 8.7, the verticality of the etched sidewall is excellent (typically better than  $\pm 0.5^\circ$ ). However, as seen in Figure 8.6, there is some evidence of sidewall roughness in the form of vertical striations. A clearer view of the sidewall roughness is shown in Figure 8.8. Note that there are two different types of roughness that can be observed. At the top of the etched face, we can see some fine scale roughness that is related to how long the sidewall is exposed to the

etch. Further down, vertical lines that start at the top of the sidewall are visible. These seem to be due to roughness of the edge of the etch mask that is transferred to the polymer sidewall. In Chapter Seven we discussed our current efforts to reduce this roughness.

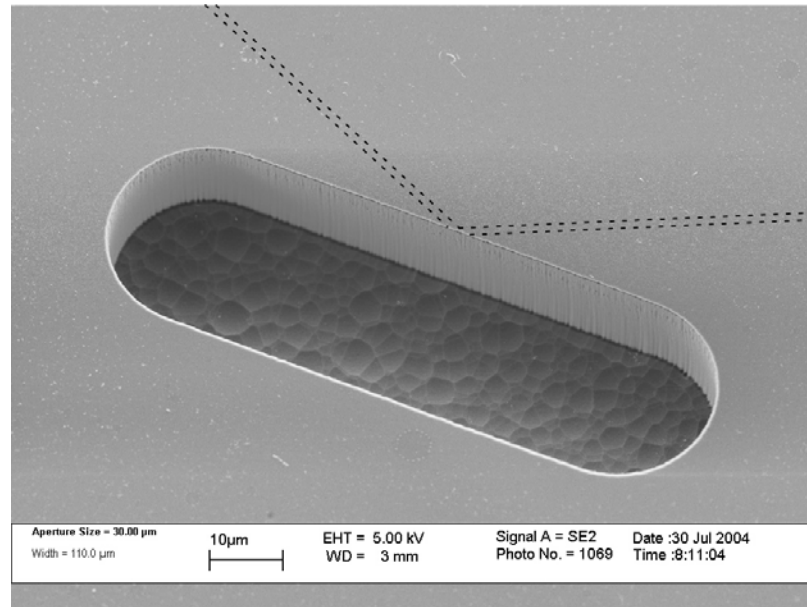


Figure 8.6. SEM image of finished air trench bend. The rounded edges are introduced to reduce stress. The dotted line depicts the waveguide core location.

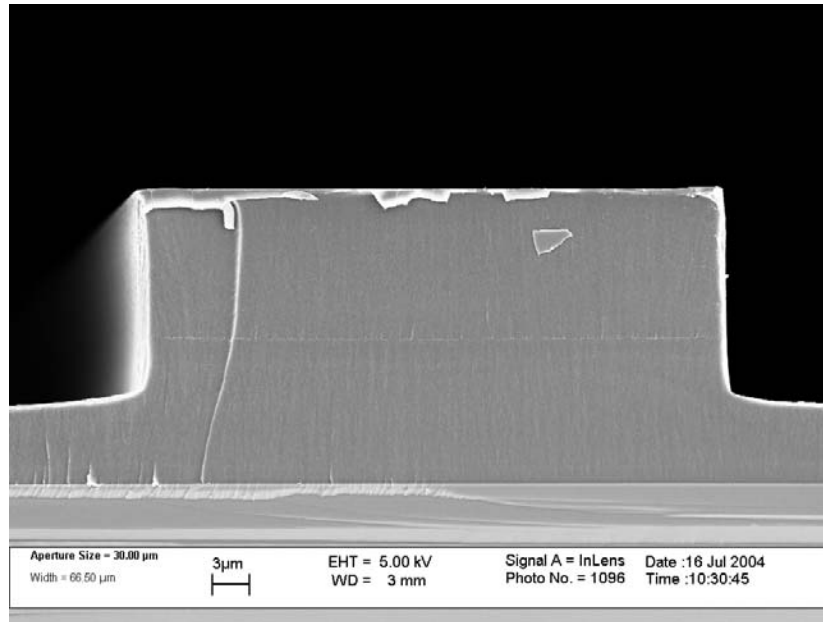


Figure 8.7. SEM image of a typical sidewall for the deep anisotropic air trench etch.

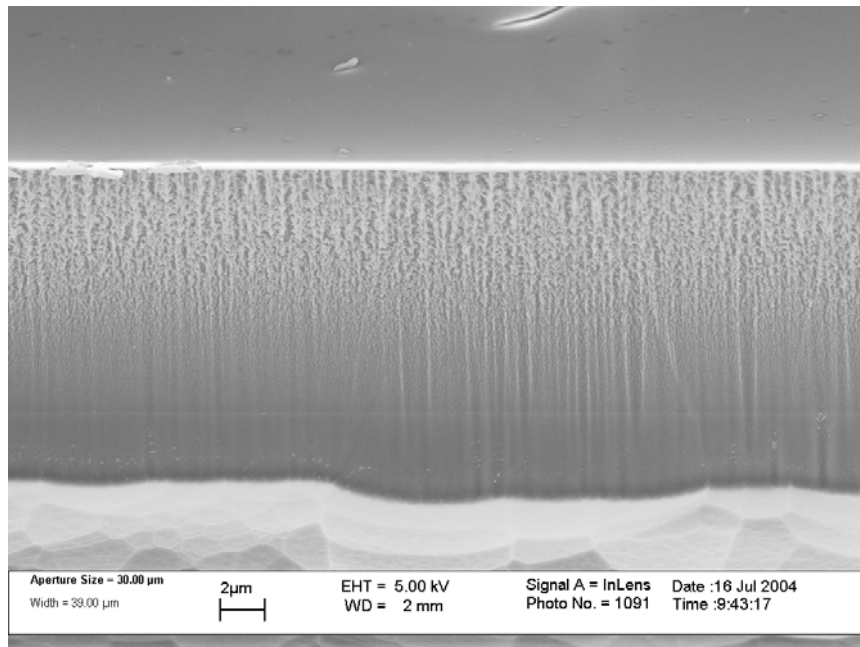


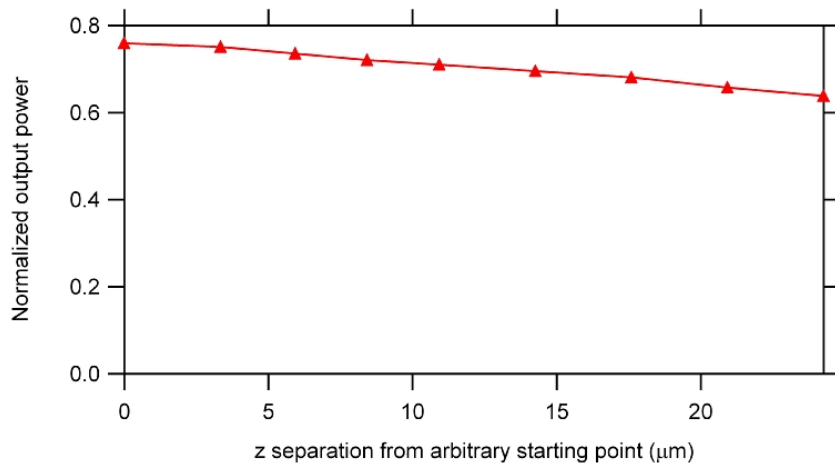
Figure 8.8. SEM image of a typical air trench sidewall.

## 8.4 Experimental Measurement and Discussion

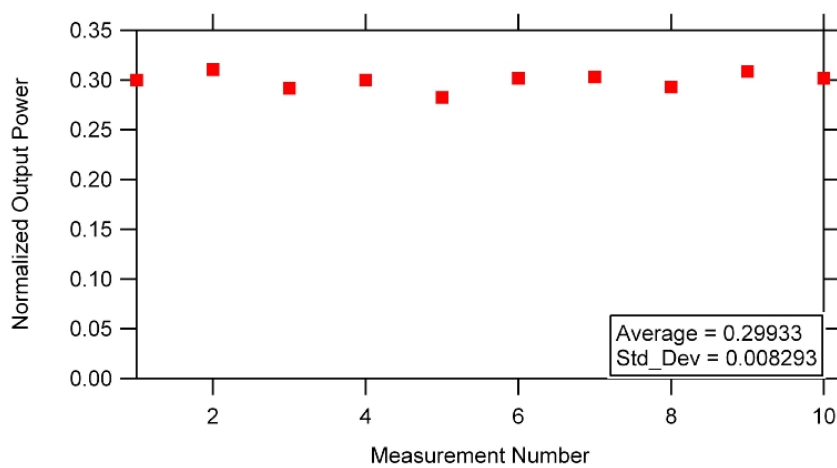
Our measurement setup consists of a laser operating at 1550nm coupled to a polarization maintaining (PM) fiber, which is butt coupled to an input waveguide on the device die. For detection, we use a single mode (SM) fiber butt coupled to the corresponding output waveguide. The fiber is connected to a photodetector. Both input and output fibers are on computer controlled three axis translation stages with piezo actuators. Index matching oil is used with the input and output fibers to improve the coupling efficiency and reduce scattering due to end face roughness on the waveguides. For TM measurements, the PM fiber is rotated to orient the electric field perpendicular to the substrate, while for TE it is oriented parallel to the substrate.

We automated our test bench to perform a simultaneous conical scan with the input and output fibers to find the maximum throughput for a waveguide. This yields measurement standard deviations typically less than one percent. However, the separation between each fiber and the waveguide is set manually using a reticle while looking through the eyepiece of a microscope set at a total magnification of 225x. At this magnification, the resolution of the reticle is 10  $\mu\text{m}$ /division. To determine the effect of the inherent variability of a manual process on our measurement accuracy, we first examined the relationship between the measured throughput power and the separation between an output waveguide and output fiber. For simplicity we varied only one fiber's position. Figure 8.9 (a) shows the results for such a scan. Note that there is only a 13% variation in the measured optical power for a 25 $\mu\text{m}$  displacement of the fiber. We then tested the repeatability of the measured power when a user sets the fiber separation for

both input and output fibers using the method described above. The results are shown in Figure 8.9 (b). The standard deviation of the measurements is only three percent of the average value, which results in an acceptably small measurement error for the bend efficiency.



(a)



(b)

Figure 8.9. (a) Output power as a function of moving the output fiber away from the waveguide. (b) Standard deviation for measured output power in ten different measurements.

To measure the optical loss of fabricated SAIBs, we measured the power transmitted through waveguides containing 2, 4, 8, and 16 bends. Each of these waveguides in a group has the same misalignment and undercut compensation. Moreover, each waveguide has the same length so that bend loss can be measured independent of the propagation loss. The measured power for a group is plotted in dB as a function of the number of waveguide bends and the data is fitted to a straight line. The line's slope is the loss per bend.

We measured several groups among the ones that had the greatest symmetry when observed with a microscope as in Figure 8.5. The measured data for TM polarization of one of these is shown in Figure 8.10. The optical loss per bend is  $0.30 \pm 0.03\text{dB/bend}$ , which is a bend efficiency of 93.4%. For the same waveguide group, the measured bend efficiency for TE polarization is  $0.33 \pm 0.03\text{dB/bend}$ .

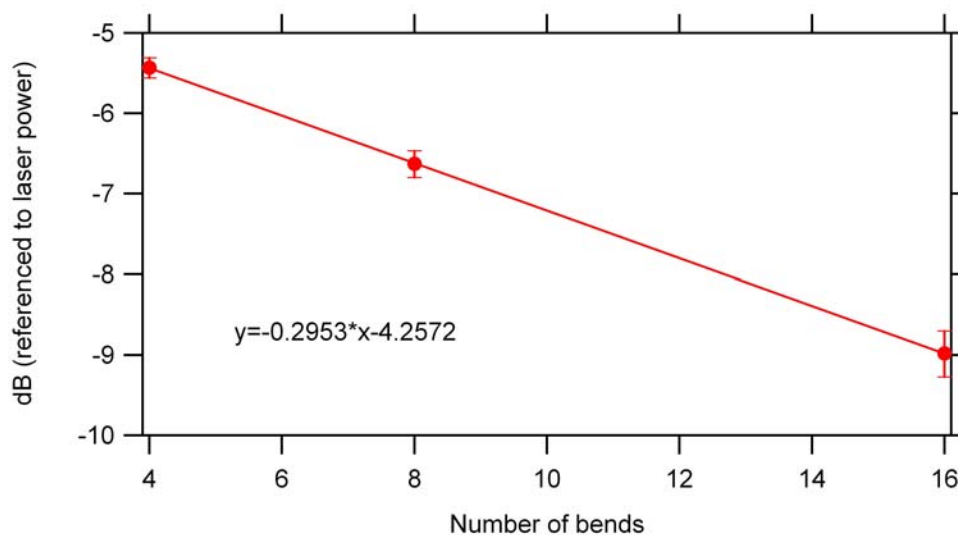


Figure 8.10. Measurement data for a waveguide group that shows a bend efficiency of 93.4% with error bars indicating the variability introduced by measurement uncertainty. This waveguide group has an undercut compensation of  $1.1\mu\text{m}$ .

By measuring the rest of the groups with  $1.1\mu\text{m}$  undercut compensation, but with different misalignment compensations, we are able to compare the predicted variation in bend efficiency as a function of misalignment with the measured data of the fabricated samples. Measurement results are shown in Figure 8.11. The experimental data is similar to the 2-D FDTD simulation data of Figure 8.3, except for the 0.25 to 0.3 dB excess loss of the measured data. We believe that this is primarily due to scattering at the bend interface, although a small amount is likely owing to residual undercut and mask alignment errors as well as a slight sidewall bowing or tilt. Also, note that the loss per bend is similar for both TE and TM polarizations for bends with the lowest loss. The polarization dependant loss for these bends is therefore quite low.

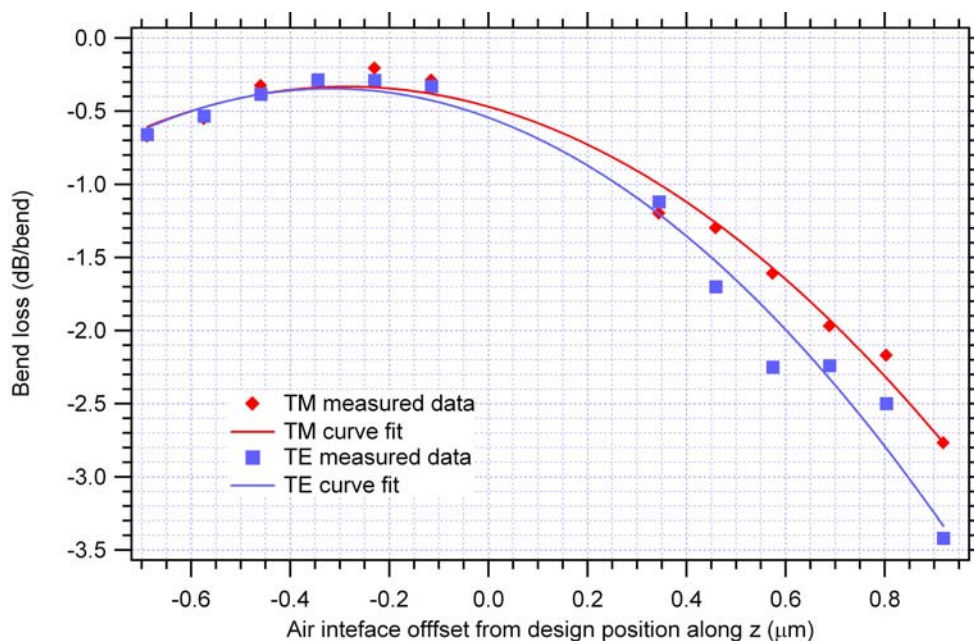


Figure 8.11. Simulation and measurement data as a function of SAIB interface misplacement. The horizontal axis is the actual offset introduced into the SAIB mask to compensate for misalignment.

## 8.5 Conclusion

We have presented results for compact high efficiency  $45^\circ$  bends in PFCB waveguides. Total internal reflection is used to reflect the waveguide mode from a single air interface. Bend design and tolerance analysis for fabrication was carried out using 2-D and 3-D FDTD simulations. The SAIB fabrication process and fabrication results have been presented. Finally, experimental measurements show an achieved bend loss of  $0.30 \pm 0.03 \text{ dB/bend}$  for TM polarization and  $0.33 \pm 0.03 \text{ dB/bend}$  for TE polarization.

Future research will focus on reducing the etched interface roughness to obtain higher bend efficiencies. Moreover, we plan to significantly reduce the air trench size to enable higher bend packing densities to be achieved. We estimate that  $40 \mu\text{m}$  by  $10 \mu\text{m}$  air trenches are feasible.

## CHAPTER 9

### CONCLUSION AND FUTURE WORK

In this dissertation I have presented research that has an underlying theme of enabling higher integration of microphotonic devices for planar lightwave circuits and sensors. This is motivated by the need to reduce costs and increase compactness for practical applications. In the area of sensors, I examined a novel detection method for microcantilever deflection detection and an integrated depolarizer. On the other hand, single air interface bends can be used to increase integration in planar lightwave circuits. In the next sections, the content covered in this work is reviewed and possible areas to continue developing.

#### 9.1 Summary

Cost reduction and compactness affect sensor systems that need to be deployed in the field because they are bound to have a shorter lifetime due to wear and tear and because they must be small enough and robust enough to make their use practical. It is a different situation for laboratory applications for which conditions are controlled and cost may not be as important as accuracy or sensitivity. Chapter Three presents a novel microcantilever detection system with applications in chemical and biological detection. This approach based on a waveguide microcantilever and a novel splitter structure allows

for higher integration of cantilevers in a single chip. This may allow for significant cost reductions and for smaller, more compact chemical and biological detectors. On the other hand, in Chapters Four and Five, we discussed an integrated optic depolarizer. This depolarizer is aimed at reducing the cost of integrated fiber optic gyroscopes by reducing the number of labor intensive steps in its fabrication. Namely, currently used depolarizers rely on two pieces of polarization maintaining fiber whose slow axes are aligned at precisely  $45^\circ$  with respect to each other. This step is costly because it must be done one at a time and requires costly labor. By cutting down the cost, interferometric fiber optic gyroscopes can become affordable for small to medium aircraft. However, as is discussed in Chapter Five, its fabrication in a polymer material system still needs the development of an etching process that can etch  $0.5\mu\text{m}$  features about eight microns deep with smooth, vertical sidewalls.

Similarly, planar lightwave circuits with higher integration, lower cost, and added functionality can reduce costs in optical network components. In Chapter Six we covered a novel micromolding approach for waveguide fabrication. The goal of this waveguide fabrication method is to reduce scattering losses due to sidewall roughness by using a mold to define the waveguide core. However, a suitable mold material wasn't found during this research.

Chapters Seven and Eight discuss the practical realization of single air interface bends in perfluorocyclobutyl polymer waveguides. Chapter Seven presents the work done towards developing an etching process to fabricate trenches a few tens of microns wide and  $16\mu\text{m}$  deep with vertical, smooth sidewalls. An etch recipe was presented which yielded vertical sidewalls of the required depth; however, the sidewall had visible

roughness. Further work developed a silicon dioxide etch and explored a different etch chemistry. The preliminary results are promising and it should be pursued further. In Chapter Eight the experimental realization of single air interface bends is presented. The designed structures are discussed, followed by the fabrication process, and measurement method. These bends were fabricated using the etching process that yielded vertical sidewalls with visible roughness. Even with this roughness, the measured bend efficiency was 0.3dB/bend.

The next section discusses future research opportunities for the work included in this dissertation.

## **9.2 Future Research**

The future research work is presented by topic. Each topic is covered in a different section below.

### **9.2.1 Photonic Microcantilevers**

Potential areas for future research in photonic microcantilevers can be divided into design and analysis, experimental proof of the splitter's functionality, and fabrication and testing of waveguide microcantilever sensors. The structure should be designed for other material systems with which microcantilevers can be fabricated. Additionally, while the splitter structure shows great potential, other structures may offer similar or better performance. Thus, further research in the splitter structure design may be warranted. The research presented here is purely based on numerical calculations. The next logical step is

to prove the concepts by fabricating and experimentally verifying that the splitter structure can achieve a sensitivity close to the predicted one. Finally, the waveguide microcantilever sensor must be fabricated and tested. Its deflection should be measured by several methods including the one presented here to demonstrate its successful operation.

### 9.2.2 Integrated Optic Depolarizer

There is a good opportunity for future research in the development of the etch process need to fabricate this device. Several paths can be explored. For instance, the process based on sulfur passivation described in Chapter Five can be explored at lower platen temperatures. On the other hand, other etch chemistries may be able to provide greater passivation for the polymer materials being used. Thus, the use of other combinations of gases such as carbon monoxide and oxygen could be explored.

### 9.2.3 PFCB Etch Development

The results of the etch development for deep trenches in PFCB polymers showed great promise. Further experimentation around the process values that yielded a sidewall that was partially smooth is definitely warranted. The use of design of experiments should continue to be used to achieve this goal as it speeds up the process and helps make objective decisions on the direction the research should go. With an improved etch process single air interface bends with higher efficiency can be fabricated.

#### 9.2.4 SAIB Fabrication

In this dissertation we reported the fabrication of SAIBs with a bend efficiency of 93.4%. However, we achieved this by making many of them with different offsets and undercut compensations. This isn't practical for real applications. Future research should be devoted to developing this fabrication process on PFCB using different patterning techniques that allow for better alignment. Two techniques that could satisfy alignment tolerances are projection lithography using a stepper or electron beam lithography. Development of a fabrication process using either of these tools will enable the application of SAIBs to fabricate more complex devices in a small area.

## **APPENDIX**

### **MASK DESIGN FOR SECOND GENERATION SINGLE AIR BENDS FABRICATION AND TESTING**

The primary goal for this mask set is to produce a SAIB group in which the bends have an efficiency above 90%. In order to account for misalignment and etch undercutting, we have introduced preset offsets in the SAIB placement. We expect to achieve our goal by following this strategy.

#### **A.1 Motivation**

The purpose of this appendix is to document mask designs that include the three lithography steps required to fabricate a Single Air Trench Bend structure.

Our goals are the following:

1. Fabricate 45° Air Trench bends.
2. Characterize fabrication steps.
3. Measure alignment errors.
  - a. X and Y positioning error
  - b. Tilt error

4. Measure sidewall angle.
5. Measure patterned feature sizes and dose effects.
6. Measure undercut.

## **A.2 Mask Description**

These masks are designed to work with 3” wafers because the amount of PFCB polymer is limited. The first mask, Protect Mask (PFCB005-01-01-JCG), contains the dicing grid, patches for patterning the alignment marks and Verniers, and the alignment marks for the next lithography step. The second mask, Waveguide Mask (PFCB005-02-01-JCG), contains the waveguides, the first part of the Verniers, and the alignment marks for the next lithography step. The third mask, Trenches Mask (PFCB005-03-01-JCG), contains the air trenches and the final part of the Verniers.

The mask has 12 usable die. Each one is 1.5cm by 1.5cm (Figure A.1). The dicing grid is included in the protect mask (Figure A.2). This grid is necessary to align the dicing saw blade to cut along the desired lines when cutting out the die. The dicing grid borders every die on all four sides and has a width of 50 $\mu$ m.

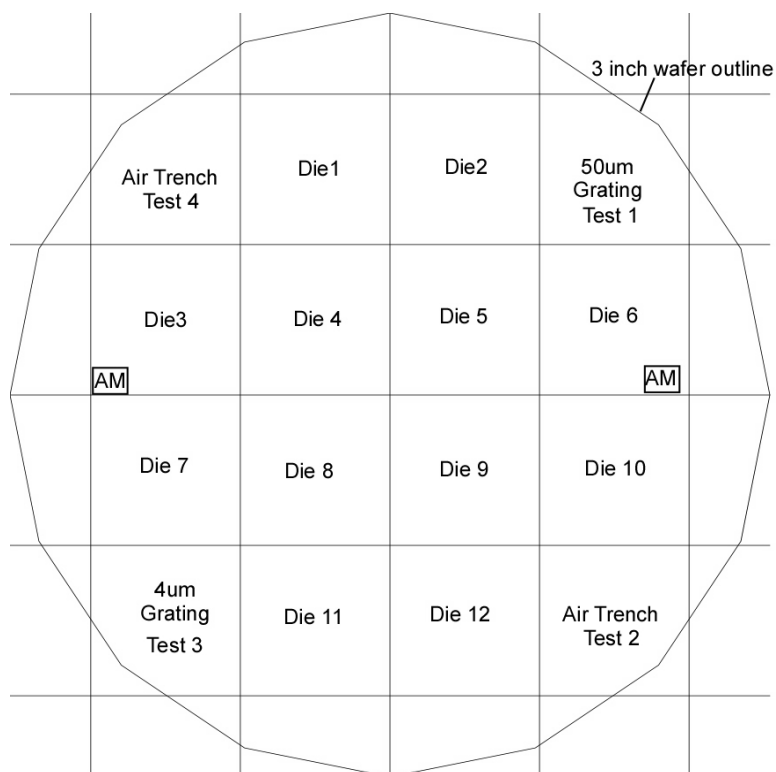


Figure A.1. The mask is divided into die which are 1.5cm by 1.5cm. The alignment marks are placed in die 3 and 6 5.6cm apart from each other.

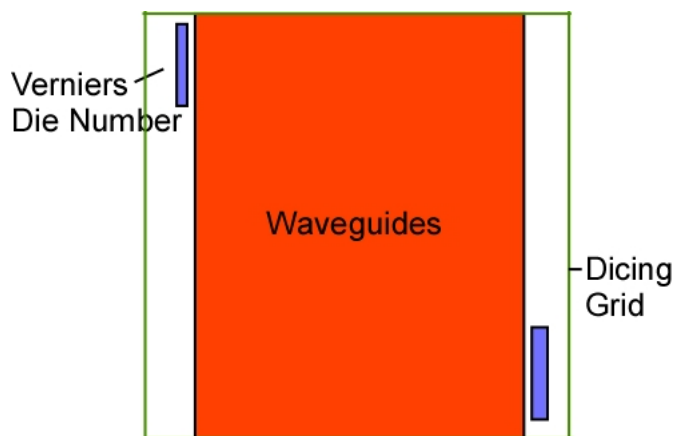


Figure A.2. A single die has the waveguide patterns inside with Verniers and the die number on the upper left and lower right corners, and a 50 $\mu$ m wide dicing grid, surrounding it.

Each die has different offsets and compensations to cover the full range. In die one through nine, the y offset was varied from 2.4 $\mu$ m to -2.4 $\mu$ m in 0.3 $\mu$ m decrements, while the undercut was varied from 0.3 $\mu$ m to 1.3 $\mu$ m in 0.2 $\mu$ m increments. To account for

all the y offset possibilities, this parameter varies in both die out of every pair. On the other hand, the undercut only changes from every pair of die to the next pair. For instance, all the groups in die one and two have different y offsets, while all of them share the same undercut compensations. The next pair (three and four) has the same y offsets, but a different undercut compensation. In the following tables the offsets of every group in every die are detailed.

### 1. Die One

- a. Contains 9 bend structures for the bend angle of 45°.
- b. These structures have preset offsets to allow for process latitude (alignment errors).
- c. Table A.1 specifies the parameters and their values for the structures in this die.
- d. Two sets of three Verniers with resolutions of 0.5, 0.2, and 0.1  $\mu\text{m}$  are included in the top left and bottom right corners of the die to evaluate the alignment accuracy after patterning of the air trenches.

Table A.1. Parameter variation for structures in die 1.

Structure number	Y offset	Undercut	CW Y Coordinate	CCW Y Coordinatate
1	2.4	0.3	3.2	1.6
2	2.1	0.3	2.9	1.3
3	1.8	0.3	2.6	1.0
4	1.5	0.3	2.3	0.7
5	1.2	0.3	2.0	0.4
6	0.9	0.3	1.7	0.1
7	0.6	0.3	1.4	-0.2
8	0.3	0.3	1.1	-0.5
9	0	0.3	0.8	-0.8

## 2. Die Two

- a. Contains 9 bend structures for the bend angle of 45°.
- b. These structures have preset offsets to allow for process latitude (alignment errors).
- c. Table A.2 specifies the parameters and their values for the structures in this die.
- d. Two sets of three Verniers with resolutions of 0.5, 0.2, and 0.1  $\mu\text{m}$  are included in the top left and bottom right corners of the die to evaluate the alignment accuracy after patterning of the air trenches.

Table A.2. Parameter variation for structures in die 2.

Structure number	Y offset	Undercut	CW Y Coordinate	CCW Y Coordinate
1	-0.3	0.3	0.5	-1.1
2	-0.6	0.3	0.2	-1.4
3	-0.9	0.3	-0.1	-1.7
4	-1.2	0.3	-0.4	-2
5	-1.5	0.3	-0.7	-2.3
6	-1.8	0.3	-1	-2.6
7	-2.1	0.3	-1.3	-2.9
8	-2.4	0.3	-1.6	-3.2
9	0	0.3	0.8	-0.8

## 3. Die Three

- a. Contains 9 bend structures for the bend angle of 45°.
- b. These structures have preset offsets to allow for process latitude (alignment errors).
- c. Table A.3 specifies the parameters and their values for the structures in this die.

- d. Two sets of three Verniers with resolutions of 0.5, 0.2, and 0.1  $\mu\text{m}$  are included in the top left and bottom right corners of the die to evaluate the alignment accuracy after patterning of the air trenches.

Table A.3. Parameter variation for structures in die 3.

Structure number	Y offset	Undercut	CW Y Coordinate	CCW Y Coordinate
1	2.4	0.5	3.7	1.1
2	2.1	0.5	3.4	0.8
3	1.8	0.5	3.1	0.5
4	1.5	0.5	2.8	0.2
5	1.2	0.5	2.5	-0.1
6	0.9	0.5	2.2	-0.4
7	0.6	0.5	1.9	-0.7
8	0.3	0.5	1.6	-1
9	0	0.5	1.3	-1.3

#### 4. Die Four

- a. Contains 9 bend structures for the bend angle of 45°.
- b. These structures have preset offsets to allow for process latitude (alignment errors).
- c. Table A.4 specifies the parameters and their values for the structures in this die.
- d. Two sets of three Verniers with resolutions of 0.5, 0.2, and 0.1  $\mu\text{m}$  are included in the top left and bottom right corners of the die to evaluate the alignment accuracy after patterning of the air trenches.

Table A.4. Parameter variation for structures in die 4.

Structure number	Y offset	Undercut	CW Y Coordinate	CCW Y Coordinate
1	-0.3	0.5	1	-1.6
2	-0.6	0.5	0.7	-1.9
3	-0.9	0.5	0.4	-2.2
4	-1.2	0.5	0.1	-2.5
5	-1.5	0.5	-0.2	-2.8
6	-1.8	0.5	-0.5	-3.1
7	-2.1	0.5	-0.8	-3.4
8	-2.4	0.5	-1.1	-3.7
9	0	0.5	1.3	-1.3

## 5. Die Five

- a. Contains nine bend structures for the bend angle of 45°.
- b. These structures have preset offsets to allow for process latitude (alignment errors).
- c. Table A.1 specifies the parameters and their values for the structures in this die.
- d. Two sets of three Verniers with resolutions of 0.5, 0.2, and 0.1  $\mu\text{m}$  are included in the top left and bottom right corners of the die to evaluate the alignment accuracy after patterning of the air trenches.

Table A.5. Parameter variation for structures in die 5.

Structure number	Y offset	Undercut	CW Y Coordinate	CCW Y Coordinate
1	2.4	0.7	4.2	0.6
2	2.1	0.7	3.9	0.3
3	1.8	0.7	3.6	0
4	1.5	0.7	3.3	-0.3
5	1.2	0.7	3	-0.6
6	0.9	0.7	2.7	-0.9
7	0.6	0.7	2.4	-1.2
8	0.3	0.7	2.1	-1.5
9	0	0.7	1.8	-1.8

## 6. Die Six

- a. Contains 9 bend structures for the bend angle of 45°.
- b. These structures have preset offsets to allow for process latitude (alignment errors).
- c. Table A.1 specifies the parameters and their values for the structures in this die.
- d. Two sets of three Verniers with resolutions of 0.5, 0.2, and 0.1  $\mu\text{m}$  are included in the top left and bottom right corners of the die to evaluate the alignment accuracy after patterning of the air trenches.

Table A.6. Parameter variation for structures in die 6.

Structure number	Y offset	Undercut	CW Y Coordinate	CCW Y Coordinate
1	-0.3	0.7	1.5	-2.1
2	-0.6	0.7	1.2	-2.4
3	-0.9	0.7	0.9	-2.7
4	-1.2	0.7	0.6	-3
5	-1.5	0.7	0.3	-3.3
6	-1.8	0.7	0	-3.6
7	-2.1	0.7	-0.3	-3.9
8	-2.4	0.7	-0.6	-4.2
9	0	0.7	1.8	-1.8

## 7. Die Seven

- a. Contains 9 bend structures for the bend angle of 45°.
- b. These structures have preset offsets to allow for process latitude (alignment errors).
- c. Table A.1 specifies the parameters and their values for the structures in this die.

- d. Two sets of three Verniers with resolutions of 0.5, 0.2, and 0.1  $\mu\text{m}$  are included in the top left and bottom right corners of the die to evaluate the alignment accuracy after patterning of the air trenches.

Table A.7. Parameter variation for structures in die 7.

Structure number	Y offset	Undercut	CW Y Coordinate	CCW Y Coordinate
1	2.4	0.9	4.8	0
2	2.1	0.9	4.5	-0.3
3	1.8	0.9	4.2	-0.6
4	1.5	0.9	3.9	-0.9
5	1.2	0.9	3.6	-1.2
6	0.9	0.9	3.3	-1.5
7	0.6	0.9	3	-1.8
8	0.3	0.9	2.7	-2.1
9	0	0.9	2.4	-2.4

## 8. Die Eight

- a. Contains 9 bend structures for the bend angle of 45°.
- b. These structures have preset offsets to allow for process latitude (alignment errors).
- c. Table A.1 specifies the parameters and their values for the structures in this die.
- d. Two sets of three Verniers with resolutions of 0.5, 0.2, and 0.1  $\mu\text{m}$  are included in the top left and bottom right corners of the die to evaluate the alignment accuracy after patterning of the air trenches.

Table A.8. Parameter variation for structures in die 8.

Structure number	Y offset	Undercut	CW Y Coordinate	CCW Y Coordinate
1	-0.3	0.9	2.1	-2.7
2	-0.6	0.9	1.8	-3
3	-0.9	0.9	1.5	-3.3
4	-1.2	0.9	1.2	-3.6
5	-1.5	0.9	0.9	-3.9
6	-1.8	0.9	0.6	-4.2
7	-2.1	0.9	0.3	-4.5
8	-2.4	0.9	0	-4.8
9	0	0.9	2.4	-2.4

## 9. Die Nine

- a. Contains 9 bend structures for the bend angle of 45°.
- b. These structures have preset offsets to allow for process latitude (alignment errors).
- c. Table A.1 specifies the parameters and their values for the structures in this die.
- d. Two sets of three Verniers with resolutions of 0.5, 0.2, and 0.1  $\mu\text{m}$  are included in the top left and bottom right corners of the die to evaluate the alignment accuracy after patterning of the air trenches.

Table A.9. Parameter variation for structures in die 9.

Structure number	Y offset	Undercut	CW Y Coordinate	CCW Y Coordinate
1	2.4	1.1	5.3	-0.5
2	2.1	1.1	5	-0.8
3	1.8	1.1	4.7	-1.1
4	1.5	1.1	4.4	-1.4
5	1.2	1.1	4.1	-1.7
6	0.9	1.1	3.8	-2
7	0.6	1.1	3.5	-2.3
8	0.3	1.1	3.2	-2.6
9	0	1.1	2.9	-2.9

## 10. Die Ten

- a. Contains 9 bend structures for the bend angle of 45°.
- b. These structures have preset offsets to allow for process latitude (alignment errors).
- c. Table A.1 specifies the parameters and their values for the structures in this die.
- d. Two sets of three Verniers with resolutions of 0.5, 0.2, and 0.1  $\mu\text{m}$  are included in the top left and bottom right corners of the die to evaluate the alignment accuracy after patterning of the air trenches.

Table A.10. Parameter variation for structures in die 10.

Structure number	Y offset	Undercut	CW Y Coordinate	CCW Y Coordinate
1	-0.3	1.1	2.6	-3.2
2	-0.6	1.1	2.3	-3.5
3	-0.9	1.1	2	-3.8
4	-1.2	1.1	1.7	-4.1
5	-1.5	1.1	1.4	-4.4
6	-1.8	1.1	1.1	-4.7
7	-2.1	1.1	0.8	-5
8	-2.4	1.1	0.5	-5.3
9	0	1.1	2.9	-2.9

## 11. Die Eleven

- a. Contains 9 bend structures for the bend angle of 45°.
- b. These structures have preset offsets to allow for process latitude (alignment errors).
- c. Table A.1 specifies the parameters and their values for the structures in this die.

- d. Two sets of three Verniers with resolutions of 0.5, 0.2, and 0.1  $\mu\text{m}$  are included in the top left and bottom right corners of the die to evaluate the alignment accuracy after patterning of the air trenches.

Table A.11. Parameter variation for structures in die 11.

Structure number	Y offset	Undercut	CW Y Coordinate	CCW Y Coordinate
1	2.4	1.3	5.8	-1
2	2.1	1.3	5.5	-1.3
3	1.8	1.3	5.2	-1.6
4	1.5	1.3	4.9	-1.9
5	1.2	1.3	4.6	-2.2
6	0.9	1.3	4.3	-2.5
7	0.6	1.3	4	-2.8
8	0.3	1.3	3.7	-3.1
9	0	1.3	3.4	-3.4

## 12. Die Twelve

- a. Contains 9 bend structures for the bend angle of 45°.
- b. These structures have preset offsets to allow for process latitude (alignment errors).
- c. Table A.1 specifies the parameters and their values for the structures in this die.
- d. Two sets of three Verniers with resolutions of 0.5, 0.2, and 0.1  $\mu\text{m}$  are included in the top left and bottom right corners of the die to evaluate the alignment accuracy after patterning of the air trenches.

Table A.12. Parameter variation for structures in die 12.

Structure number	Y offset	Undercut	CW Y Coordinate	CCW Y Coordinate
1	-0.3	1.3	3.1	-3.7
2	-0.6	1.3	2.8	-4
3	-0.9	1.3	2.5	-4.3
4	-1.2	1.3	2.2	-4.6
5	-1.5	1.3	1.9	-4.9
6	-1.8	1.3	1.6	-5.2
7	-2.1	1.3	1.3	-5.5
8	-2.4	1.3	1	-5.8
9	0	1.3	3.4	-3.4

### 13. Structures

#### a. Single Air Interface Bend.

- i. This structure was designed to test the efficiency of 2, 4, 8, and 16 air trench SAIB.
- ii. The propagation length is equal in all of the paths so that the propagation loss can be subtracted from all the measurements.
- iii. This structure is shown in Figure A.3.

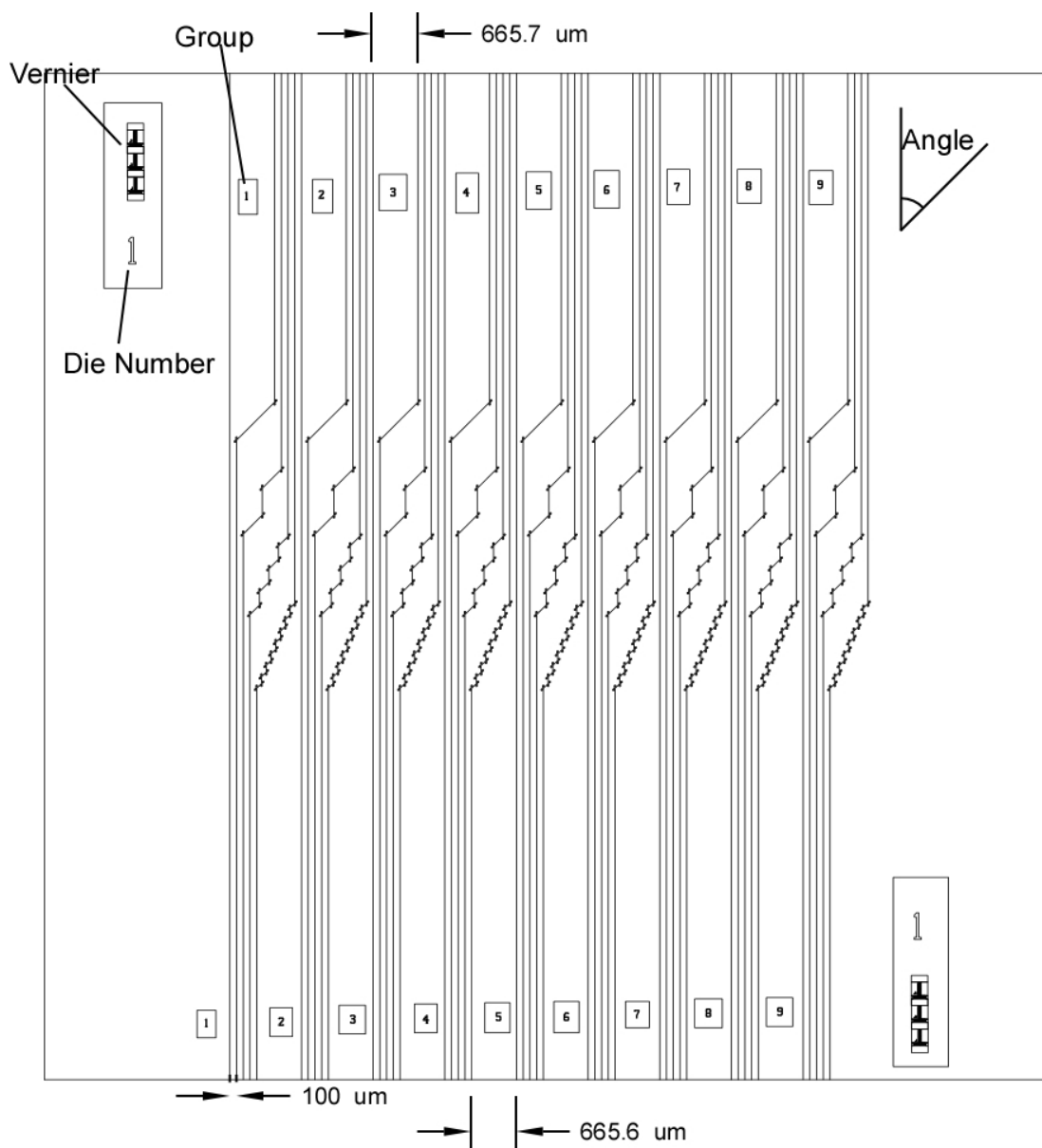


Figure A.3 Structure's layout for die 1 through 12. The figure is to scale.

#### 14. Additional Structures (see Figure A.1)

##### a. Air trench gratings (Test 1).

- i. Gratings with a period representative of all the air trenches being patterned for SAIB are included on a portion of the die to the right of die 2.

- ii. These gratings allow for evaluation in the SEM of the etch without having to destroy a device die.
- b. Trenches (Tests 2 and 4)
  - i. Trenches with the same dimensions and angle as the air trenches in the actual devices are included to allow SEM imaging of air trench characteristics such as undercut and roughness.
- c. Waveguide gratings for etch depth measurements (Test 4)
  - i. A grating with a period of 8  $\mu\text{m}$ , which corresponds to twice the waveguide width for equal line and space width, is included to the left of die 11. However, this grating is buried under the overcladding.

#### Fabrication Procedure (see Figure A.4)

- a. Coat Underclad layer
- b. Coat Core layer
- c. Deposit  $\text{SiO}_2$  hard mask (50nm)
- d. Deposit Cr mask (~90nm)
- e. Coat photoresist (positive)
- f. Pattern protect mask
- g. 30s  $\text{O}_2$  descum in ICP
- h. Wet etch Cr.
- i. 5min  $\text{O}_2$  descum in ICP

- j. Deposit SiO<sub>2</sub> hard mask (120nm)
- k. Coat photoresist (positive)
- l. Pattern with waveguide mask (must align to protect layer)
- m. RIE etch SiO<sub>2</sub>
- n. Wet etch Cr
- o. Etch waveguide
- p. BHF dip for SiO<sub>2</sub> removal (60s)
- q. Coat Overclad layer
- r. Deposit SiO<sub>2</sub> hard mask (500nm)
- s. Coat photoresist (positive)
- t. Pattern air trench mask (must align to waveguide layer)
- u. RIE etch SiO<sub>2</sub> mask
- v. ICP RIE etch air trench
- w. Dice in the dicing saw

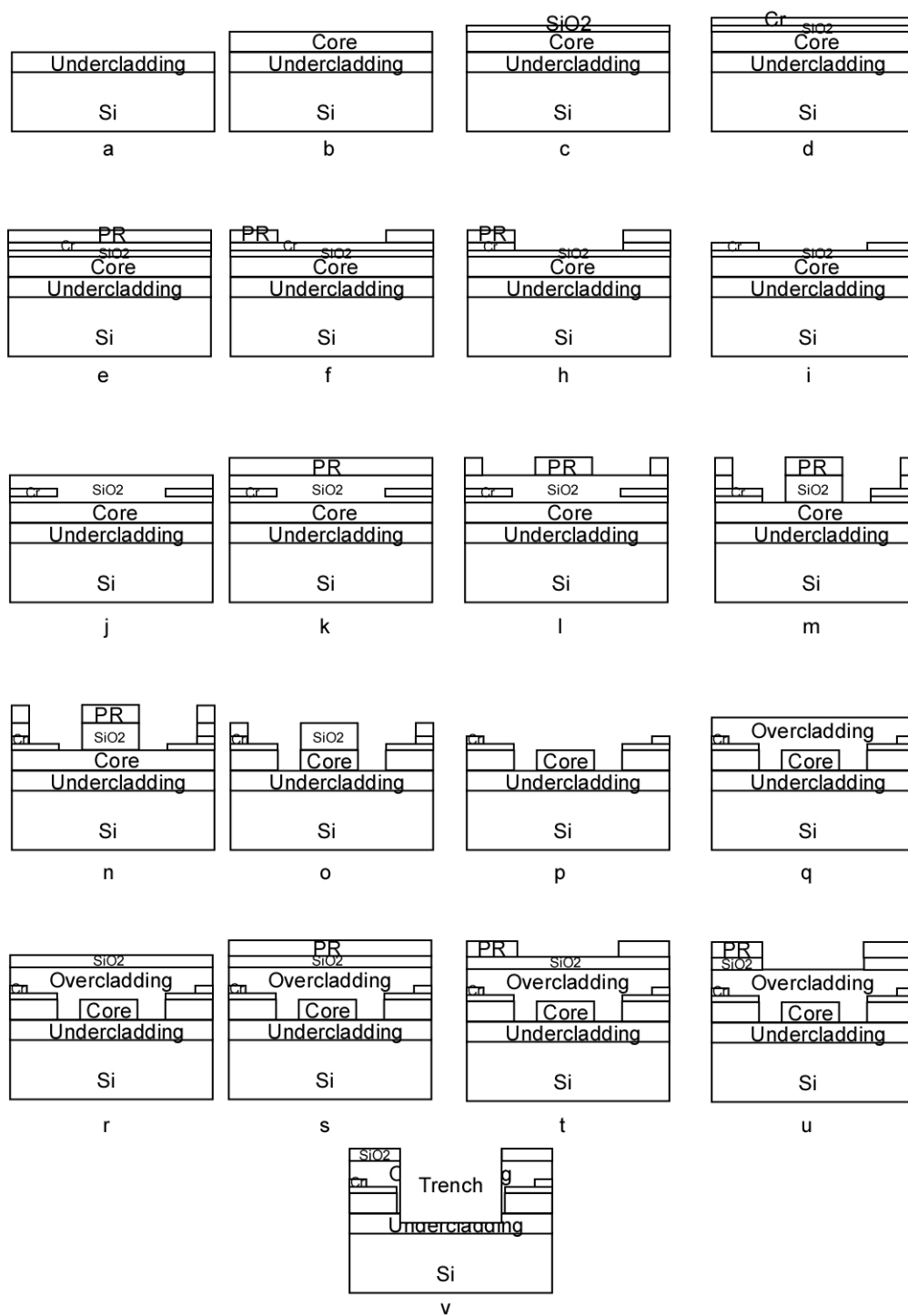


Figure A.4. Fabrication process for SAIB. Note that step g was omitted in the figure.

## REFERENCES

- [1] Y.P. Li, C. H. Henry, "Silica-based Optical Integrated Circuits," IEE Proc. Optoelectron., Vol. 143, pp. 263-280, 1996.
- [2] L. Li, *Compact Waveguide Bends and Application in a Waveguide Depolarizer*, Ph.D. Dissertation, University of Alabama in Huntsville, 2004.
- [3] J. Cardenas, L. Li, S. Kim, G. Nordin, "Compact Low Loss Single Air Interface Bends in Polymer Waveguides," Opt. Express, Vol. 12, pp. 5314-5324, 2004.
- [4] T. Thundat, P. I. Oden, R. J. Warmack, "Microcantilever Sensors," Microscale Thermophysical Engineering, Vol. 1, pp. 185-199, 1997.
- [5] S. Cherian, T. Thundat, "Determination of Adsorption-induced Variation in the Spring Constant of a Microcantilever," Appl. Phys. Lett., Vol. 80, pp. 2219-2221, 25 March 2002.
- [6] M. Godin, V. Tabard-Cossa, P. Grutter, "Quantitative Surface Stress Measurements Using a Microcantilever," Appl. Phys. Lett., Vol. 79, pp. 551-553, 23 July 2001.
- [7] J. Yang, T. Ono, M. Esashi, "Mechanical Behavior of Ultrathin Microcantilever," Sensors and Actuators, Vol. 82, pp. 102-107, 2000.
- [8] G. G. Stoney, Proc. R. Soc. London, Ser. A, 82, 172, 1909.
- [9] H.P. Lang, R. Berger, C. Andreoli, J. Brugger, M. Despont, P. Vettiger, Ch. Gerber, J.K. Gimzewski, J.P. Ramseyer, E. Meyer, H.J. Guntherodt, "Sequential Position Readout from Arrays of Micromechanical Cantilever Sensors," Appl. Phys. Lett., Vol. 72, pp. 383-385, 19 January 1998.
- [10] H.P. Lang, M.K. Baller, R. Berger, Ch. Gerber, J.K. Gimzewski, F.M. Battiston, P. Fornaro, J.P. Ramseyer, E. Meyer, H.J. Guntherodt, "An Artificial Nose Based on a Micromechanical Cantilever Array," Analytica Chimica Acta, 393, pp. 59-65, 1999.
- [11] M. Yang, X. Zhang, K. Vafai, C. S. Ozkan, "High Sensitivity Piezoresistive Cantilever Design and Optimization for Analyte-receptor Binding," J. Micromech. Microeng., Vol. 13, pp. 864-872, 2003.

- [12] J. Thaysen, A. D. Yalcinkaya, P. Vettiger, A. Menon, "Polymer-based Stress Sensor with Integrated Readout," *J. Phys. D: Appl. Phys.*, Vol. 35, pp. 2698-2703, 2002.
- [13] E.M. Chow, G.G. Yaralioglu, C.F. Quate, T.W. Kenny, "Characterization of a Two-dimensional Cantilver Array with Through-wafer Electrical Interconnects," *Appl. Phys. Lett.*, Vol. 80, pp. 664-666, 28 January 2002.
- [14] M. Calleja, P. Rasmussen, A. Johansson, A. Boisen, "Polymeric Mechanical Sensors with Integrated Readout in a Microfluidic System," *Proc. SPIE*, Vol. 5116, Smart Sensors, Actuators, and MEMS, pp.314-321, 2003.
- [15] H.C. Lefevre, *The Fiber-optic Gyroscope*, (An Artech House Publication, Boston, 1993), pp. 5-25.
- [16] *Ibid*, Chaps. 4, 5, and 7.
- [17] D. Stowe, D. Moore, R. Priest, "Polarization Fading in Fiber Interferometric Sensors," *IEEE J. of Quantum Elec.* Vol. 18, pp. 1644-1647, 1982
- [18] B. Szafraniec, G.A. Sanders, "Theory of Polarization Evolution in Interferometric Fiber-optic Depolarized Gyros," *J. Lightwave Technol.*, Vol. 17, pp. 579-590, 1999.
- [19] M. Madou, *Fundamentals of Microfabrication*, (A CRC Press Publication, Boca Raton, 1997), pp. 53-88.
- [20] M. Zhou, "Low-loss Polymeric Materials for Passive Waveguide Components in Fiber Optical Telecommunication," *Opt. Eng.*, Vol. 41, pp. 1631-1643, 2002.
- [21] B. Schuppert, E. Brose, K. Petermann, R. Moosburger, "Anisotropic Plasma Etching of Polymers Using a Cryo-cooled Resist Mask," *J. Vac. Sci. Technol. A*, Vol. 18, pp. 385-387, 2000.
- [22] M. Pons, J. Pelletier, O. Joubert, "Anisotropic Etching of Polymers in SO<sub>2</sub>/O<sub>2</sub> Plasmas: Hypotheses on Surface Mechanisms," *J. Appl. Phys.*, Vol. 75, pp. 4709-4715, 1994.
- [23] M. R. Baklanov, S. Vanhaelemeersch, H. Bender, K. Maex, "Effects of Oxygen and Fluorine on the Dry Etch Characteristics of Organic Low-k Dielectrics," *J. Vac. Sci. Technol. B*, Vol. 17, pp. 372-379, 1999.
- [24] K. Han, J. Kim, W. Jang, "Evaluation of Halogenated Polyimide Etching for Optical Waveguide Fabrication by Using Inductively Coupled Plasma," *J. Appl. Polym. Sci.*, Vol. 79, pp. 176-182, 2001.
- [25] S. Inoue, K. Kajikawa, "Inductively Coupled Plasma Etching to Fabricate the Nonlinear Optical Polymer Photonic Crystal Waveguides," *Mat. Sci. Eng. B*, Vol. 103, pp. 170-176, 2003.

- [26] J. C. Arnold, H. H. Sawin, "Charging of Pattern Features During Plasma Etching," *J. Appl. Phys.*, Vol. 70, pp. 5314-5317, 1991.
- [27] D. Fuard, O. Joubert, L. Vallier, M. Assous, P. Berruyer, R. Blanc, "Etch Mechanisms of Low Dielectric Constant Polymers in High Density Plasmas: Impact of Charging Effects on Profile Distortion During the Etching Process," *J. Vac. Sci. Technol. B*, Vol. 19, pp. 2223-2230, 2001.
- [28] M. Pons, O. Joubert, P. Paniez, J. Pelletier, "Plasma Etching of Polymers: A Reinvestigation of Temperature Effects," *J. Appl. Phys.*, Vol. 70, pp. 2376-2379, 1991.
- [29] S. Panda, D. J. Economou, "Anisotropic Etching of Polymer Films by High Energy (~100s of eV) Oxygen Atom Neutral Beams," *J. Vac. Sci. Technol. A*, Vol. 19, pp. 398-404, 2001.
- [30] M. K. Smit, E. C. M. Pennings, H. Blok, "A Normalized Approach to the Design of Low-loss Optical Waveguide Bends," *J. Lightwave Technol.*, Vol. 11, pp. 1737-1742, 1993.
- [31] H. Lin, Y. Lin, W. Wang, "Analysis of Abrupt Waveguide Bend with Low-index Microprism," *IEEE J. Quantum Elec.*, Vol. 34, pp. 2291-2297, 1998.
- [32] C. Manolatu, S. G. Johnson, S. Fan, P. R. Villeneuve, H. A. Haus, J. D. Joannopoulos, "High-density Integrated Optics," *J. Lightwave Technol.*, Vol. 17, pp. 1682-1692, 1999.
- [33] R. L. Espinola, R. U. Ahmad, R. Pizzuto, M. J. Steel, R. M. Osgood, Jr., "A Study of High-index-contrast 90° Waveguide Bend Structures," *Opt. Express*, Vol. 8, pp. 517-528, 2001.
- [34] L. Li, G. P. Nordin, J. M. English, J. Jiang, "Small-area Bends and Beamsplitters for Low-index-contrast Waveguides," *Opt. Express*, Vol. 11, pp. 282-290, 2003.
- [35] G. P. Nordin, S. Kim, J. Cai, J. Jiang, "Hybrid Integration of Conventional Waveguide and Photonic Crystal Structures," *Opt. Express*, Vol. 10, pp. 1334-1341, 2002.
- [36] Y. A. Vlasov, S. J. McNab, "Losses in Single-mode Silicon-on-insulator Strip Waveguides and Bends," *Opt. Express*, Vol. 12, pp. 1622-1631, 2004.
- [37] M. Popovic, K. Wada, S. Akiyama, H. A. Haus, J. Michel, "Air Trenches for Sharp Silica Waveguide Bends," *J. Lightwave Technol.*, Vol. 20, pp. 1762-1771, 2002.
- [38] J. E. Johnson, C. L. Tang, "Precise Determination of Turning Mirror Loss Using GaAs/AlGaAs Lasers with Up to Ten 90° Intracavity Turning Mirrors," *Phot. Technol. Lett.*, Vol. 4, pp. 24-26, 1992.

- [39] P. D. Swanson, B. D. Shire, C. L. Tang, M. A. Parker, J. S. Kimmet, R. J. Michalak, "Electron-cyclotron Resonance Etching of Mirrors for Ridge-guided Lasers," *Phot. Technol. Lett.*, Vol. 7, pp. 605-607, 1995.
- [40] Y. Z. Tang, W. H. Wang, T. Li, Y. L. Wang, "Integrated Waveguide Turning Mirror in Silicon-on-insulator," *Phot. Technol. Lett.*, Vol. 14, pp. 68-70, 2002.
- [41] NSF proposal # 0330032 in response to solicitation NSF 03-512, "SIRG: Photonic Microcantilever Arrays for Chemical and Biological Sensing," Principle investigator: G. P. Nordin, submitted March 2003.
- [42] NSF proposal #0428289 in response to solicitation NSF 2004-235, "SIRG: Photonic Microcantilever Arrays for Chemical and Biological Sensing," Principle investigator: G. P. Nordin, submitted February 2004.
- [43] B. E. A. Saleh, M. C. Teich, *Fundamentals of Photonics*, (A Wiley-Interscience Publication, New York, 1991), pp. 673-690.
- [44] K. Bohm, D. Petermann, "Performance of Lyot Depolarizers with Birefringent Single-mode Fibers," *J. Lightwave Technol.*, Vol. 1, pp. 71-74, 1983.
- [45] H. Lefevre, *The Fiber-Optic Gyroscope*, (Artech House, Boston, 1993), pp. 84-86.
- [46] M. Born, E. Wolf, *Principles of Optics*, 7<sup>th</sup> edition, (Cambridge University Press, 1999).
- [47] J. Auñón, V. Chandrasekar, *Introduction to Probability and Random Processes*, (McGraw Hill, 1997).
- [48] Y. Shani, R. Alferness, T. Koch, U. Koren, M. Oron, B. Miller, M. Young, "Polarization Rotation in Asymmetric Periodic Loaded Rib Waveguides," *Appl. Phys. Lett.*, Vol. 59, pp. 1278-1280, September 1991.
- [49] S. Obayya, B. Rahman, H. El-Mikati, "Vector Beam Propagation Analysis of Polarization Conversion in Periodically Loaded Waveguides," *Phot. Technol. Lett.*, Vol. 12, October 2000, pp. 1346-1348.
- [50] W. Huang Z. Mao, "Polarization Rotation in Periodic Loaded Rib Waveguides," *J. of Lightwave Technol.*, Vol. 10, pp. 1825-1831, 1992.
- [51] J. Cai, J. Jiang, G. P. Nordin, "Ultrashort Waveguide Polarization Converter Using a Subwavelength Grating," presented at Integrated Photonics Research, San Francisco, 2004.
- [52] F. Ladoceur, J. D. Love, T. J. Senden, "Effect of Sidewall Roughness in Buried Channel Waveguides," *IEE Proc. Optoelectron.*, Vol. 141, pp. 242-248, 1994.

- [53] J. P. R. Lacey, F. P. Payne, "Radiation Loss from Planar Waveguides with Random Wall Imperfections," IEE Proceedings, Vol. 137, pp. 282-288, 1990.
- [54] Chinoy, P.B., "Reactive Ion Etching of Benzocyclobutene Polymer Films," IEEE Transactions on Components, Packaging, and Manufacturing Technology-Part C, Vol. 20, pp. 199-206, 1997.
- [55] Y. Song, K. Powell, D. Thomas, S. Sardo, M. Gentili, "Fabrication of Deep Oxide Gratings by Electron-beam Lithography and MORI Reactive Ion Etching," Presented at ECS 206<sup>th</sup> Meeting Abs. 1441, 2004.
- [56] D. C. Montgomery, *Design and Analysis of Experiments, 5<sup>th</sup> edition*, (John Wiley and Sons, New York, 2001).
- [57] W. J. Diamond, *Practical Experiment Designs, 3<sup>rd</sup> edition*, (John Wiley and Sons, New York, 2001).
- [58] G. E. P. Cox, W. G. Hunter, J. S. Hunter, *Statistics for Experimenters*, (John Wiley and Sons, New York, 1978).
- [59] S. J. Choi, K. Djordjev, S. J. Choi, P. D. Dapkus, "CH<sub>4</sub>-based Dry Etching of High Q InP Microdisks," J. Vac. Sci. Technol. B, Vol 20, pp. 301-305, 2002.
- [60] L. H. Spiekman, Y. S. Oei, E. G. Metaal, F. H. Groen, P. Demeester, M. K. Smit, "Ultrasmall Waveguide Bends: The Corner Mirrors of the Future?" IEE Proc. Optoelectron., Vol. 142, pp. 61-65, 1995.
- [61] S. Kim, G. P. Nordin, J. Jiang, J. Cai, "High Efficiency 90° Silica Waveguide Bend Using an Air Hole Photonic Crystal Region," Phot. Technol. Lett., Vol. 16, pp. 1846-1848, 2004.
- [62] K. Ogusu, "Transmission Characteristics of Optical Waveguide Corners," Opt. Comm., Vol. 55, pp. 149-153, 1985.
- [63] R. Orobtcouk, S. Laval, D. Pascal, A. Koster, "Analysis of Integrated Optical Waveguide Mirrors," J. Lightwave Technol., Vol. 15, pp. 815-820, 1997.
- [64] L. Faustini, C. Coriasso, A. Stano, C. Cacciatore, D. Campi, "Loss Analysis and Interference Effect in Semiconductor Integrated Waveguide Turning Mirrors," Phot. Technol. Lett., Vol. 8, pp. 1355-1357, 1996.
- [65] D. W. Smith, Jr., S. Chen, S. Kumar, J. Ballato, H. Shah, C. Topping, S. H. Foulger, "Perfluorocyclobutyl Copolymers for Microphotonics," S. Adv. Mater., Vol. 14, p. 1585, 2002.

[66] D. W. Smith, Jr., A. B. Hoeglund, H. V. Shah, M. J. Radler, C. A. Langhoff, "Perfluorocyclobutane Polymers for Optical Fibers and Dielectric Waveguides," *Optical Polymers*, J. Harmon, Ed., ACS Symp. Ser. 795, Ch. 4, pp. 49-62, 2001.

[67] J. Ballato, D. W. Smith, Jr., S. H. Foulger, "Optical Properties of Perfluorocyclobutyl (PFCB) Polymers," *J. Opt. Soc. Am. B*, Vol. 80, pp. 1838-1843, 2003.